Chapter 5

Topology Optimization of Lift–drag Problems [†]

CONTENTS

5.1 Introduction

Fluid-related shape and topology optimization has undergone a tremendous development in various directions since the seminal work by Borrvall and Petersson (2003), such as turbulent flows (Yoon, 2016; Dilgen, Dilgen, Fuhrman, Sigmund, and Lazarov, 2018a; Picelli, Moscatelli, Yamabe, Alonso, Ranjbarzadeh, Santos Gioria, Meneghini, and Silva, 2022), non-Newtonian flows (Pingen and Maute, 2010; Alonso, Saenz, and Silva, 2020), unsteady state flows (Kreissl, Pingen, and Maute, 2011; Nobis, Schlatter, Wadbro, Berggren, and Henningson, 2022), and many multiphysics such as fluid–structure interaction (FSI) (Yoon, 2010b; Ranjbarzadeh, Picelli, Gioria, and Silva, 2022), thermal-fluids (Dede, 2009; Troya, Tortorelli, Andrej, and Beck, 2021), etc. Detailed and meticulous records and classification of fluid-related TO can be found in the review paper by Alexandersen and Andreasen (2020) , see also a very recent review paper by Fawaz, Hua, Le Corre, Fan, and Luo (2022) for heat exchanger designs based on TO techniques. The majority of the previous works mainly focused on the internal flows, whereas the external flows have received much less scientific attention in the state-of-the-art TO developments. More specifically, in

[†]The work in this chapter has been accepted for publication in *Structural and Multidisciplinary Optimization* (Springer), 2022.

the aerodynamics design, very few TO works have been carried out to find an optimal shape for a flying object with the exception of Kondoh, Matsumori, and Kawamoto (2012), Garcke, Hinze, Kahle, and Lam (2018), Feppon, Allaire, Dapogny, and Jolivet (2020b), and Ghasemi and Elham (2022). The early works (Kondoh, Matsumori, and Kawamoto, 2012; Garcke, Hinze, Kahle, and Lam, 2018) are limited to two-dimensional designs and/or very low Reynolds cases. Feppon, Allaire, Dapogny, and Jolivet (2020b) are known as the first who performed the shape and topology optimization in a three-dimensional setting. Their method relies on the boundary variation of Hadamard for describing the sensitivity of functions with respect to the domain. Finally, and very recently, Ghasemi and Elham (2022) constructed an efficient multi-stage density-based TO framework for solving 2D and 3D aerodynamic problems in the laminar flow regime. They proposed an operator-based analytical differentiation (OAD) to compute the exact partial derivatives of the flow solver. They developed their solver via OpenFOAM software and delivered promising designs in both two- and three-dimensional settings.

As briefly discussed above, various TO techniques have been applied in the context of fluid-related problems. Besides the density-based and level-set based approaches, we also notice that very recently some researches adopted an inverse homogenization (or dehomogenization) method to recover the optimized porous media performance by way of intricate microchannel structures in a post-processing step (Zhou, Lohan, Zhou, Nomura, and Dede, 2022). But here we mainly discuss the two most popular approaches (density-based and level set-based approaches) used in fluid TO. In the density-based approach, the key idea is to use a monolithic formulation by introducing the Brinkman penalization on fixed meshes. The density-based approach is a promising method that allows one to design from scratch. The main bottleneck is that the non-conforming mesh lacks a high resolution fluid–solid interface description. To overcome this problem, fine meshes need to be used everywhere in the design domain. However, when performing the primal and adjoint analyses, the solution of the linear system $Ax = b$ can be quite costly even by leveraging parallel implementations. The level set-based method, on the other hand, uses an implicit zero-level-set isosurface for the description of the fluid–solid boundary, which can be used as a metric when being coupled with surface capturing techniques such as cutFEM (Villanueva and Maute, 2017) and body-fitted adaptive meshes, or local mesh refinement such as iso-/anisotropic adaptive meshes. However, the above-mentioned specific numerical techniques increase the overall computational cost (i.e., remeshing cost) as the total state variable increases. With this in mind, an efficient computational tool can be of great significance in fluid TO. It is now clear that the core interests behind this are the flow modelings and meshing techniques, which have been seldom discussed in depth in the literature.

The aim of this chapter is to report on the technical increments toChapters 2 to 4, where we proposed a reaction–diffusion equation-based (RDE) topology optimization (TO) framework for solving the fluid optimization problems. More specifically, the distributed unstructured mesh adaptation has seldom been used for topology optimization in the previous works, and this work is a first step in that direction to the best of our knowledge. It is indeed a technical issue, but

still, it requires a fully-distributed framework (including scalable domain decomposition, matrix assembly, parallel interpolation, linear solver) that very few general purpose libraries offer. In addition, as we shall show below, this work is the first attempt to conduct a comparative study by showcasing different flow modeling strategies with their advantages and disadvantages.

In our previous works, body-fitted meshes were used. As one of the surface capturing techniques, this enables the disjoint reunion of a global mesh that involves several (fluid/solid) subdomains, whose interfaces are described by an implicit zero-level-set isosurface. Therefore, the fluid–structure system can be modeled using separate equations where a no-slip boundary condition is imposed on the moving fluid–solid boundaries. Hereinafter, for brevity, we name it as the "separate" modeling. However, such an implicit surface remeshing could be a significant performance bottleneck since it is currently performed on a single MPI process. In effect, it sometimes becomes even a heavier workload than solving state equations. In addition, it also raises a challenge that even though a parallel solver could use a sequential remesher by gathering a partitioned mesh on a single MPI process, it is not always possible to handle a large mesh on it due to memory limitations (Park, Loseille, Krakos, Michal, and Alonso, 2016). Thanks to the versatility of the RDE method, we can also model the fluid–solid system using a monolithic formulation. For brevity, hereinafter, we name it as the "hybrid" flow modeling strategy, see the schematic illustration in Fig. 5.1c.

In this chapter, we shed a light on an external flow optimization problem and run our newly updated TO algorithm, in which ParMmg is used for the parallel iso-/anisotropic mesh adaptation. To this end, we first formulate a lift–drag optimum design problem in Section 5.2. In Section 5.3, we provide the implementation details and illustrate how different meshing techniques (fixed mesh, isotropic mesh, anisotropic mesh, and body-fitted mesh) are integrated in different flow modeling strategies ("separate" and "hybrid"). Then, we present in Section 5.4 various 2D and large-scale 3D design examples and conduct an in-depth comparative study. Lastly, the main findings and the limitations of the approach are summarized in Section 5.5.

5.2 Formulation

5.2.1 Governing equations

The fluid flow is governed by the incompressible steady-state laminar flow (the gravity effect is neglected in this chapter). The basic motion of a fluid particle within the fluid domain Ω_f is characterized by the dimensionless velocity $\boldsymbol{v} : \Omega_f \to \mathbb{R}^d$ and the dimensionless pressure $p : \Omega_f \to$

$\mathbb{R}$, which are the unique solutions of the following continuity and Navier–Stokes (NS) equations:

$$\begin{cases} -\operatorname{div}\left(\sigma_{\mathrm{f}}\left(\boldsymbol{v}, p\right)\right) + \left(\boldsymbol{v}\cdot\nabla\right)\boldsymbol{v} - \boldsymbol{f}_{\mathrm{Da}}\left(\boldsymbol{v}\right) = 0 & \text{in } \Omega_{\mathrm{f}} \\ -\operatorname{div}\left(\boldsymbol{v}\right) = 0 & \text{in } \Omega_{\mathrm{f}} \\ \boldsymbol{v} = \boldsymbol{v}_0 & \text{on } \partial\Omega_{\mathrm{f}}^{D} \\ \sigma_{\mathrm{f}}\left(\boldsymbol{v}, p\right)\cdot\boldsymbol{n}_{\mathrm{f}} = 0 & \text{on } \partial\Omega_{\mathrm{f}}^{N} \\ \boldsymbol{v} = 0 & \text{on } \Gamma_{\mathrm{s,f}} \\ \boldsymbol{v}\cdot\boldsymbol{n} = 0 & \text{on } \Gamma, \end{cases} \tag{5.1}$$

where $\Gamma := \partial\Omega \backslash \left(\partial\Omega_{\mathrm{f}}^{D} \cup \partial\Omega_{\mathrm{f}}^{N} \cup \Gamma_{\mathrm{s,f}}\right)$ denotes the free-slip boundaries. $\boldsymbol{n}_{\mathrm{f}}$ is the unit normal vector. The fluid stress tensor $\sigma_{\mathrm{f}}\left(\boldsymbol{v}, p\right)$ is defined as follows:

$$\sigma_{\mathrm{f}}\left(\boldsymbol{v}, p\right) := 2\frac{1}{Re}e\left(\boldsymbol{v}\right) - p\mathbf{I}, \tag{5.2}$$

where Re is the Reynolds number, and $\mathbf{I}$ is the identity matrix. The strain tensor is given as: $e\left(\boldsymbol{v}\right) := \frac{1}{2}\left(\nabla\boldsymbol{v} + \nabla\boldsymbol{v}^{\mathrm{T}}\right)$.

The dimensionless fictitious body force term $\boldsymbol{f}_{\mathrm{Da}}\left(\boldsymbol{v}\right) = -\alpha\boldsymbol{v}$ is introduced in the momentum equation, where $\alpha\left(H_\phi\right)$ is the inverse permeability of the fictitious porous medium, which can be interpolated as follows:

$$\alpha\left(H_\phi\right) = \alpha_{\max}\left(1 - H_\phi\right), \tag{5.3}$$

where $\alpha_{\max}$ is the upper bound of the effective inverse impermeability in the solid domains. For the case of "separate" modeling using body-fitted mesh, α is only to aid the sensitivity analysis. Therefore, $\alpha_{\max}$ can be any positive value. For the case of "hybrid" modeling, we set $\alpha_{\max} = 10^7$ in this chapter. In the authors experience, generally a lower order of magnitude of $\alpha_{\max}$ may cause an unstable fluid–solid surface evolution, especially for the case of higher Reynolds number. Thus, its value should be large enough to stop the flow, please see also our very recent contribution on natural convection optimization problem for further discussions Chapter 4.

The nonlinear problem defined in Eq. (5.1) is solved using a classical Newton method where the linearized fluid equations are solved in sequence.

5.2.2 Optimum design problem

The optimum design problem in this chapter is to maximize the lift force under the constraints of: (1) drag force, (2) volume, and (3) center of mass. The optimization model can be formulated as follows:

$$\inf_{H_\phi \in \mathcal{X}} J(\Omega) = -\operatorname{Lift}(\Gamma, \boldsymbol{v}(\Gamma), p(\Gamma)) \tag{5.4a}$$

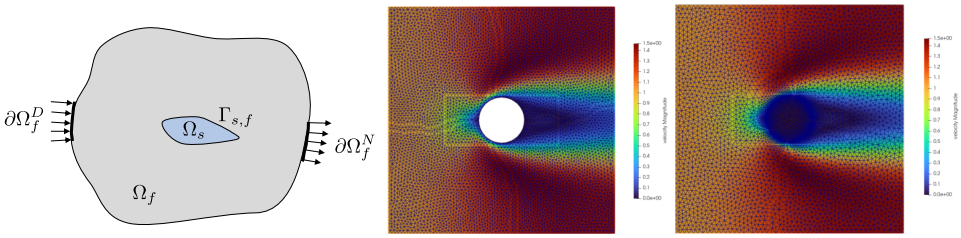

(A) Schematic. (B) "Separate" modeling. (C) "Hybrid" modeling.

FIGURE 5.1: (a) Schematic of the lift–drag problem and two flow modeling strategies using: (b) body-fitted mesh and (c) isotropic mesh.

$$\text{s.t.} \begin{cases} G_1 = \text{Drag}(\Gamma, \boldsymbol{v}(\Gamma), p(\Gamma)) - C_0 \text{Drag}_0 \leq 0 \\ G_2 = \dfrac{\int_D (1 - H_\phi) d\Omega}{\int_D d\Omega} - V_{\max} = 0 \\ G_3 = \dfrac{\int_D \boldsymbol{x} (1 - H_\phi) d\Omega}{\int_D (1 - H_\phi) d\Omega} - \boldsymbol{x}_0 = 0 \\ \textit{Eq.}\ (5.1)\ \text{(Navier–Stokes equations)}, \end{cases} \tag{5.4b}$$

where the maximum allowed drag force is imposed to be $C_0 \, \text{Drag}_0$, where Drag_0 is the value computed based on the minimal drag problem subject to the same volume fraction $V_{\max}$ and the center of mass (COM) constraints. $\boldsymbol{x}_0 = (x_0, y_0, z_0)$ denotes the target x-, y-, and z-coordinates of the COM. As for the cost functions, we follow the lead of Kondoh, Matsumori, and Kawamoto (2012) by describing the drag and lift forces as the boundary integrals[1], defined as below:

$$\text{Drag} = -\int_{\partial\Omega \setminus \Gamma_{s,f}} (\boldsymbol{v} \cdot \boldsymbol{e}_x)(\boldsymbol{v} \cdot \boldsymbol{n}) + p\boldsymbol{n} \cdot \boldsymbol{e}_x \, d\Gamma \tag{5.5a}$$

$$\text{Lift} = -\int_{\partial\Omega \setminus \Gamma_{s,f}} (\boldsymbol{v} \cdot \boldsymbol{e}_y)(\boldsymbol{v} \cdot \boldsymbol{n}) + p\boldsymbol{n} \cdot \boldsymbol{e}_y \, d\Gamma, \tag{5.5b}$$

where $(\boldsymbol{e}_x, \boldsymbol{e}_y, \boldsymbol{e}_z)$ is the canonical basis of $\mathbb{R}^3$. Using Lagrange's method, we replace the optimization problem given in Eq. (5.4) with an unconstrained optimization problem. The Lagrangian is formulated as follows:

$$\begin{aligned} &\mathscr{L}(\boldsymbol{v}, \boldsymbol{v}_A, p, p_A, \lambda_1, \lambda_2, \lambda_3, \lambda_4, \lambda_5, \Omega) \\ &= J(\Omega) + \langle \boldsymbol{v}_A, R_1 \rangle + \langle p_A, R_2 \rangle + \sum_{i=1}^{5} \lambda_i G_i, \end{aligned} \tag{5.6}$$

[1]Other cost functions for the lift–drag problem can be found in Kondoh, Matsumori, and Kawamoto (2012) for the density-based approach, and Feppon, Allaire, Dapogny, and Jolivet (2020a) for an extension to a domain integral which is to aid the shape derivative. See also Garcke, Hinze, Kahle, and Lam (2018) for a phase-field method.

where $\boldsymbol{v}_A$ and p_A are the adjoint velocity and adjoint pressure, respectively, and λ_i is the Lagrange multipliers associated to the corresponding constraint functional. The design sensitivity[2] can be derived as follows:

$$\bar{F}' = \int_\Omega -\alpha_{\max} \boldsymbol{v} \cdot \boldsymbol{v}_A - \lambda_2 - \lambda_3 (x - x_0) - \lambda_4 (y - y_0) - \lambda_5 (z - z_0) \, \mathrm{d}\Omega, \tag{5.7}$$

where $\boldsymbol{v}_A$ and p_A can be obtained by solving the following adjoint equations:

$$\begin{cases} -\boldsymbol{v} \cdot \nabla \boldsymbol{v}_A + \boldsymbol{v}_A \cdot \nabla \boldsymbol{v}^{\mathrm{T}} - \dfrac{1}{Re} \nabla \cdot \left(\nabla \boldsymbol{v}_A + \nabla \boldsymbol{v}_A^{\mathrm{T}} \right) + \alpha \boldsymbol{v}_A + \nabla p_A = 0 \\ -\nabla \cdot \boldsymbol{v}_A = 0, \end{cases} \tag{5.8}$$

with the following adjoint boundary conditions:

$$\begin{cases} \boldsymbol{v}_A = \lambda_1 \boldsymbol{e}_x - \boldsymbol{e}_y & \text{on } \partial\Omega_{\mathrm{f}}^D \\ \left(\boldsymbol{v} \cdot \boldsymbol{e}_y \right) \boldsymbol{n} - \lambda_1 \left(\left(\boldsymbol{v} \cdot \boldsymbol{e}_x \right) \boldsymbol{n} + \boldsymbol{e}_x \left(\boldsymbol{v} \cdot \boldsymbol{n} \right) \right) + \boldsymbol{v}_A (\boldsymbol{v} \cdot \boldsymbol{n}_{\mathrm{f}}) & \\ + \dfrac{1}{Re} \left(\nabla \boldsymbol{v}_A + \nabla \boldsymbol{v}_A^{\mathrm{T}} \right) \cdot \boldsymbol{n}_{\mathrm{f}} - p_A \boldsymbol{n}_{\mathrm{f}} = 0 & \text{on } \partial\Omega_{\mathrm{f}}^N \\ \boldsymbol{v}_A = 0 & \text{on } \Gamma_{\mathrm{s,f}} \\ \boldsymbol{v}_A \cdot \boldsymbol{n} = 0 & \text{on } \Gamma. \end{cases} \tag{5.9}$$

The adjoint equations defined in Eqs. (5.8) and (5.9) can be expressed in the weak form as follows:

$$\begin{aligned} &\int_\Omega -\tilde{\boldsymbol{v}}_A \cdot (\boldsymbol{v} \cdot \nabla \boldsymbol{v}_A) + \tilde{\boldsymbol{v}}_A \cdot \left(\boldsymbol{v}_A \cdot \nabla \boldsymbol{v}^{\mathrm{T}} \right) + \frac{1}{Re} \nabla \tilde{\boldsymbol{v}}_A : \left(\nabla \boldsymbol{v}_A + \boldsymbol{v}_A^{\mathrm{T}} \right) \\ &+ \tilde{\boldsymbol{v}}_A \cdot \alpha \boldsymbol{v}_A - p_A \nabla \cdot \tilde{\boldsymbol{v}}_A - \tilde{p}_A \nabla \cdot \boldsymbol{v}_A d\Omega \\ &+ \int_{\partial\Omega_{\mathrm{f}}^N} \left(\boldsymbol{v} \cdot \boldsymbol{e}_y \right) \left(\tilde{\boldsymbol{v}}_A \cdot \boldsymbol{n} \right) + \left(\boldsymbol{e}_y \cdot \tilde{\boldsymbol{v}}_A \right) \left(\boldsymbol{v} \cdot \boldsymbol{n} \right) + \left(\boldsymbol{v}_A \cdot \tilde{\boldsymbol{v}}_A \right) \left(\boldsymbol{v} \cdot \boldsymbol{n} \right) \\ &- \lambda_5 \left(\left(\boldsymbol{v} \cdot \boldsymbol{e}_x \right) \left(\tilde{\boldsymbol{v}}_A \cdot \boldsymbol{n} \right) + \left(\boldsymbol{e}_x \cdot \tilde{\boldsymbol{v}}_A \right) \left(\boldsymbol{v} \cdot \boldsymbol{n} \right) \right) d\Gamma \\ &\forall (\tilde{\boldsymbol{v}}_A, \tilde{p}_A) \in \mathscr{U}_{v,p}, (\boldsymbol{v}, p) \in \mathscr{U}_{v,p}, \end{aligned} \tag{5.10}$$

where $\tilde{\boldsymbol{v}}_A$ and $\tilde{p}_A$ are the test functions for the adjoint velocity and adjoint pressure, respectively. We set the classical Hilbert spaces for the velocity v, pressure p, as follows:

$$\mathscr{U}_{v,p} := \left\{ (\tilde{\boldsymbol{v}}, \tilde{p}) \in H^1 \left(\Omega_{\mathrm{f}}, \mathbb{R}^d \right) \times L^2 \left(\Omega_{\mathrm{f}} \right) \mid \tilde{\boldsymbol{v}} = 0 \text{ on } \partial\Omega_{\mathrm{f}}^D \right\} \tag{5.11}$$

[2]The differential to H_ϕ instead of to ϕ makes it possible to evolve the topological configuration rather than only shape variation. To fully reflect the topological evolution capability of the proposed method, we present in Section 5.4.1 a test case for the classical minimal power dissipation problem.

5.3 Implementation details

Here, we overview the numerical implementation techniques. In this chapter, we use FreeFEM (Hecht, 2012; Jolivet, Dolean, Hecht, Nataf, Prud'homme, and Spillane, 2012) for the discretization of PDEs, and PETSc (Balay, Abhyankar, Adams, Benson, Brown, Brune, Buschelman, Constantinescu, Dalcin, Dener, Eijkhout, Gropp, Hapla, Isaac, Jolivet, Karpeev, Kaushik, Knepley, Kong, Kruger, May, McInnes, Mills, Mitchell, Munson, Roman, Rupp, Sanan, Sarich, Smith, Zampini, Zhang, Zhang, and Zhang, 2021) for distributed linear algebra. For the first time, we use parallel iso-/anisotropic adaptive meshes thanks to ParMmg, see the details in (Cirrottola and Froehly, 2021). The isotropic or shape regular adaptive methods use only elements with bounded aspect ratio (stretched elements are avoided), see Fig. 5.2c . The anisotropic adaptive methods (see Fig. 5.2e), on the other hand, fit high aspect ratio elements (highly stretched elements) along the regions of rapid variation of the solution for situations like interior or boundary layers (Aguilar and Goodman, 2006). The basic idea is to use the Delaunay algorithm (George and Borouchaki, 1998) to generate a new triangular (2D) or tetrahedral (3D) mesh whose edges are close to the unit length in the metric $\mathcal{M} = \frac{|\mathcal{H}|}{\varepsilon}$, where $|\mathcal{H}|$ is the Hessian of the variable (i.e., Heaviside function H_ϕ and/or velocity gradient in this work), x a point in space, and ε the interpolation error for the variables. Note that anisotropic meshes may be generated by ParMmg if needed. For comparison, we also run the "separate" modeling algorithm and use body-fitted meshes (see Fig. 5.2g) which are generated by Mmg in sequential (Dapogny, Dobrzynski, and Frey, 2014).

We summarize in Algorithm 4 the workflow for a lift–drag optimization problem using iso-/anisotropic adaptive meshes. First, the input mesh $\mathcal{T}_0$ in the Inria Medit format is read by FreeFEM. Next, the computational domain is decomposed by a standard mesh partitioner such as METIS (Karypis and Kumar, 1998). After that, the initial level-set field is given[3]. Then, the optimization loop begins. The forward problem is solved using the Newton method and the objective value is computed. If it is converged, the optimization ends. Otherwise, the adjoint problem is solved and the sensitivity is computed. Next, the level-set function ϕ_{it} is updated using the RDE and the Heaviside function $H_{\phi_{it}}$ is obtained. After that, we centralize the solution on a global mesh and call ParMmg for updating the global mesh. Finally, the current step solutions v, p, ϕ_{it} and $H_{\phi_{it}}$ are interpolated to the newly updated mesh $\mathcal{T}_{it+1}$. The workload is then distributed again until the maximum iteration number is reached (150 in this chapter).

As for the values of the regularization parameter τ and the ficititious time step Δt, experience shows that it is more efficient to start with a larger value of τ and to gradually decrease its values in a step-wise manner in a continuation scheme. This is because a larger value of τ can accelerate the topological evolution at the beginning stage while a smaller value of τ is prone to generate sharper ends after the outline is taking shape. Similarly, the fictitious time step Δt is progressively increased to make the topological evolution not to be too slow. After pre-determining a maximum

[3]In this chapter, for all test cases, we initialize the design domain with a sphere in the center: $\phi = -1$, if $(x - x_0)^2 + (y - y_0)^2 + (z - z_0)^2 \leq R$.

allowed iteration number (e.g., 150 in this paper), the value of these two parameters is updated at the given steps (e.g., every 30 iterations), following the continuation scheme as below:

$$\begin{aligned} \tau &= \{10^{-5}, 10^{-6}, 10^{-7}, 10^{-8}\} \\ \Delta t &= \{1.5, 2.5, 3.5, 4.5\}. \end{aligned} \tag{5.12}$$

In this chapter, all the adaptive mesh cases were performed on a Linux workstation with dual Intel(R) Xeon(R) Gold 6246R with a clock frequency of 3.4 GHz, having 32 cores in total and 256 GB of memory. We use GNU compilers and OpenMPI. Besides, a large-scale fixed mesh case (cf. Fig. 5.4) was performed on Rescale cluster (`www.rescale.com`) using 8 nodes where each node is equipped with 352 GB of memory and a Xeon Platinum 8168 (Skylake) with a clock frequency of 2.7 GHz with 44 cores.

Algorithm 4 Lift–drag topology optimization using iso-/anisotropic adaptive mesh.

Input: global mesh $\mathcal{T}_0$
decompose the computational domain for parallel computing
initialize the level-set field ϕ
for $it = 0; it < 150; it = it + 1$ **do**
  solve Navier–Stokes equations on $\mathcal{T}_{it}$ using the Newton method, cf. Eq. (5.1)
  calculate the objective functional, cf. Eq. (5.5)
  if $\|J_{it} - J_{it-1}\| < \varepsilon$ **then**
    break
  else
    solve the adjoint problem on $\mathcal{T}_{it}$, cf. Eqs. (5.8) and (5.9)
    compute the sensitivity, cf. Eq. (5.7), and Lagrange multipliers
    update the level-set function ϕ_{it} by solving RDE on $\mathcal{T}_{it}$
    update the Heaviside function $H_{\phi_{it}}$
    call ParMmg to obtain $\mathcal{T}_{it+1}$ based on the input metric
    broadcast to all processes
    interpolate v, p, ϕ_{it}, and $H_{\phi_{it}}$ to $\mathcal{T}_{it+1}$
  end if
end for

5.4 Numerical investigation

In this section, first, we solve a classical 2D drag minimization problem to reveal the effects of different flow modeling strategies ("separate" and "hybrid") and different meshing techniques on the optimization results. Then, we examine the computational efficiency of our framework to a larger scale of 3D problem. Finally, we present several 3D test cases for the lift maximization under a drag constraint.

It should be noted that the fluid-based optimization problems are known to have high nonlinearity and nonconvexity, thus may converge to non-unique solutions. Furthermore, in the real-world wing design, the physics to be considered will be much more complicated, i.e., turbulent flow, or compressible flow. In such cases, even a very small change in the shape may cause a different level of impact on the aerodynamic performances. It could be said that the size optimization method is necessary when we seek for an accurate design by means of fine-tune a few CAD parameters. In this chapter, however, we limit ourselves to low/moderately high Reynolds ($Re \leq 1000$). Regardless of the above aspects, it still makes sense to compare different flow modeling strategies and different meshing techniques in the context of fluid-based topology optimization, since we are not aware, to the best of our knowledge, of the analogous discussions in the literature.

Now we start by a small-scale two-dimensional test case as shown in Fig. 5.2. The computational domain is the unit square $\Omega = [0;1]^2$. The flow enters the domain from the left-hand side with a uniform velocity profile $v = [1,0]^{\mathrm{T}}$. The flow exits the domain from the right-hand side with a zero normal stress. The top and bottom walls bear a free-slip boundary condition. A sphere with the radius of $R = 10^{-2}$ is suspended in the center of the cube. The Reynolds number is set to $Re = 100$ and the target volume is set to $2 \cdot 10^{-2}$.

The optimal configurations obtained by different meshes are shown in Fig. 5.2. The flow modeling strategy, element number, and the objective values are summarized in Table 5.1. From these comparison results, we can observe the following:

1. These optimal configurations are practically identical. If we take a close look at each, the iso-/anisotropic mesh cases feature sharper ends than those of the fixed mesh or the body-fitted mesh cases.
2. As for the fixed mesh case, in order to obtain a high-resolution optimal solution, we have to use at least twice the element number of adaptive mesh cases, see Table 5.1.
3. We use the body-fitted mesh case as a baseline for measuring flow analysis accuracy. The objective values are nearly the same. The relative difference is less than 1.4% among those cases.

TABLE 5.1: Flow modeling, element number and objective value for different mesh cases, cf. Fig. 5.2.

Mesh	Flow modeling	Element number	Obj. value
Fixed mesh, cf. Figs. 5.2a and b	Hybrid	98,352	0.201
Isotropic mesh, cf. Figs. 5.2c and d	Hybrid	36,561	0.198
Anisotropic mesh, cf. Figs. 5.2e and f	Hybrid	50,353	0.198
Body-fitted mesh, cf. Figs. 5.2g and h	Separate	13,620	0.198

Next, we extend to the 3D test cases. The computational domain is the unit cube $\Omega = [0;1]^3$. The flow enters the domain from the left-hand side with a uniform velocity profile $v = [1,0,0]^{\mathrm{T}}$.

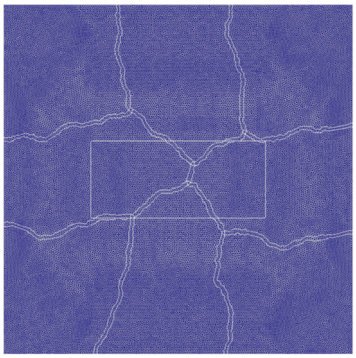

(A) Fixed mesh.

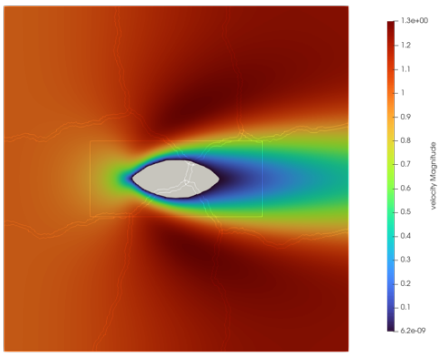

(B) Velocity field.

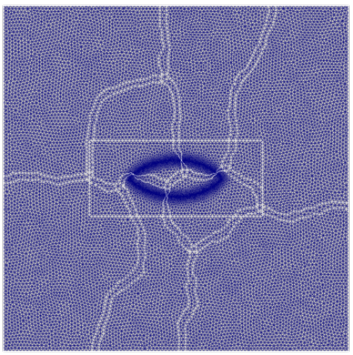

(C) Isotropic mesh.

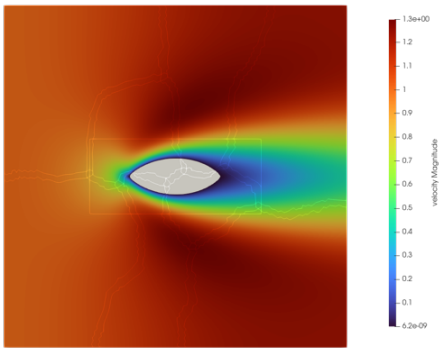

(D) Velocity field.

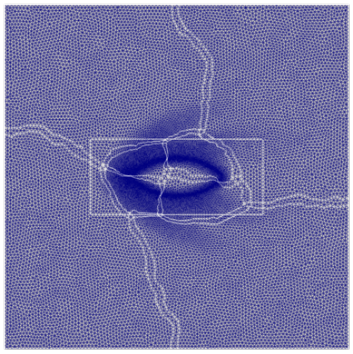

(E) Anisotropic mesh.

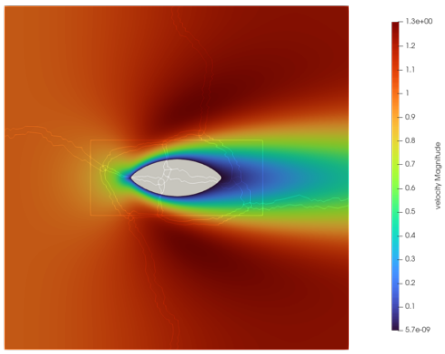

(F) Velocity field.

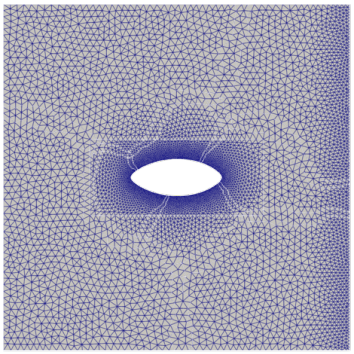

(G) Body-fitted mesh.

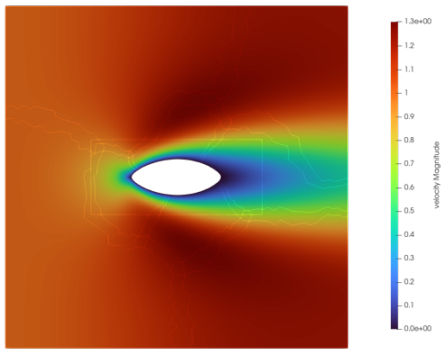

(H) Velocity field.

FIGURE 5.2: The mesh representation (left column) and velocity field (right column) using different meshes: (a)-(b): fixed mesh, (c)-(d): isotropic mesh, (e)-(f): anisotropic mesh, and (g)-(h): body-fitted mesh.

The flow exits the domain from the right-hand side with a zero normal stress. The top and side walls bear a free-slip boundary condition. A sphere with the radius of $R = 10^{-2}$ is suspended in the center of the cube. The Reynolds number is set to $Re = 100$ and the target volume is set to $3 \cdot 10^{-3}$.

The cross section views of the mesh are plotted in Fig. 5.3. For this test case, the number of tetrahedra used at the last iteration is $7.71 \cdot 10^5$ for the body-fitted mesh, cf. Fig. 5.3c, and $7.34 \cdot 10^5$ for the isotropic mesh, cf. Fig. 5.3a. The time breakdown for each finite element action is documented in Table 5.2. From the time breakdown, two results can be observed. The first is that "hybrid" modeling incorporated with isotropic mesh adaptation takes 70.9% less time than the "separate" modeling with body-fitted mesh to solve the governing equations. As for the body-fitted mesh, it is not possible to use the previous step solution as the initial guess if we repeatedly disjoin-reunion the computational domains through a geometry trimming process to treat this Stefan problem. As a result, it requires us to initialize the flow field by the solution of Stokes flow, followed by the Newton iterations for a series of Reynolds numbers until the target Reynolds is reached. In contrast, when using the "hybrid" modeling which is less sensitive to boundary conditions at the fluid–solid interfaces, we can use the previous step solution (v, p) as an initial value for the current step Newton solver. In most cases, it requires less than two Newton iterations before convergence. For the case of higher Reynolds, the "hybrid" modeling becomes an even clearer winner over the "separate" modeling, see the test case under Reynolds number of $Re = 1000$ as shown in Fig. 5.5. Note that the anisotropy of the refined mesh in the downstream area is beneficial to the convergence of the Newton solver. The second result is ParMmg takes 92.8% less time than Mmg, which is sequential, to update the mesh. Furthermore, we confirm the validity of the mesh refinement by comparing those results with the fixed mesh case, cf. Fig. 5.4. We push the total tetrahedra number to $3.12 \cdot 10^6$, having $1.32 \cdot 10^7$ degrees of freedom for the linearized fluid system.

Finally, we use the "hybrid" modeling strategy to solve the lift maximization problem under a drag constraint. The Reynolds number is set to $Re = 100$. The value of Drag_0 is $3.4 \cdot 10^{-2}$, cf. Fig. 5.6b. The optimal solutions for different values of drag coefficient $C_0 = \{1.1, 1.3, 1.5\}$ are shown in Figs. 5.6c–e and Table 5.3. Note that the optimal configurations are represented by the zero-level-set isosurface. The iterative histories of the objective and constraint values for the case of $C_0 = 1.1$ are plotted in Fig. 5.7.

5.4.1 Extensions

A minimal power dissipation problem

We present a test case for the classical minimal power dissipation problem to fully reflect the topological evolution capability of the proposed method. The optimization mathematical model

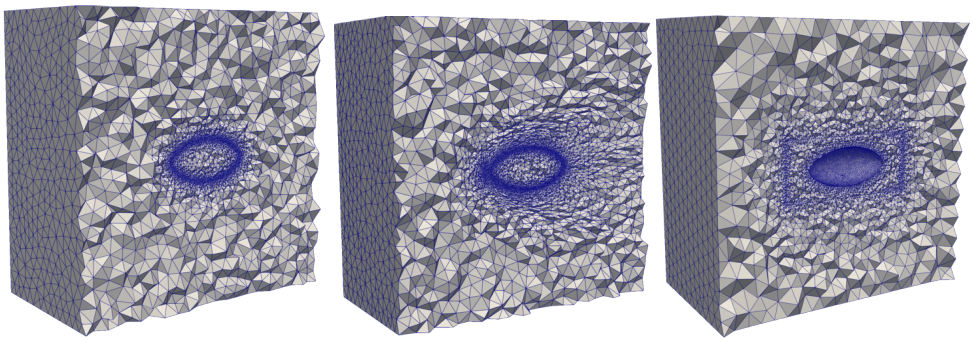

(A) Isotropic mesh. (B) Anisotropic mesh. (C) Body-fitted mesh.

FIGURE 5.3: Cross section view of the three different remeshing techniques used for drag minimization problem.

TABLE 5.2: Time breakdown of the finite element actions (in seconds) performed at the last iteration of the drag minimization problem, cf. Fig. 5.3.

Actions	Body-fitted, cf. Fig. 5.3c	Isotropic, cf. Fig. 5.3a
Solve governing equations	**127.6**	**37.1**
Solve adjoint equations	41.0	47.5
Compute sensitivity and Lagrange multiplier	0.16	0.12
Solve RDE	0.23	0.23
Visualize output	0.48	0.51
Centralize solution to process #0	0.93	0.87
Remesh	**33.7**	**2.51**
Partition updated mesh	5.19	3.18
Interpolate solution to updated mesh	1.72	1.39
Total	211.0	93.4

TABLE 5.3: Lift and drag values obtained by using different drag coefficients C_0, cf. Fig. 5.6.

C_0	Drag	Lift
1.0	$3.41 \cdot 10^{-2}$	0
1.1	$3.75 \cdot 10^{-2}$	$2.67 \cdot 10^{-3}$
1.3	$4.43 \cdot 10^{-2}$	$8.84 \cdot 10^{-3}$
1.5	$5.12 \cdot 10^{-2}$	$1.39 \cdot 10^{-2}$

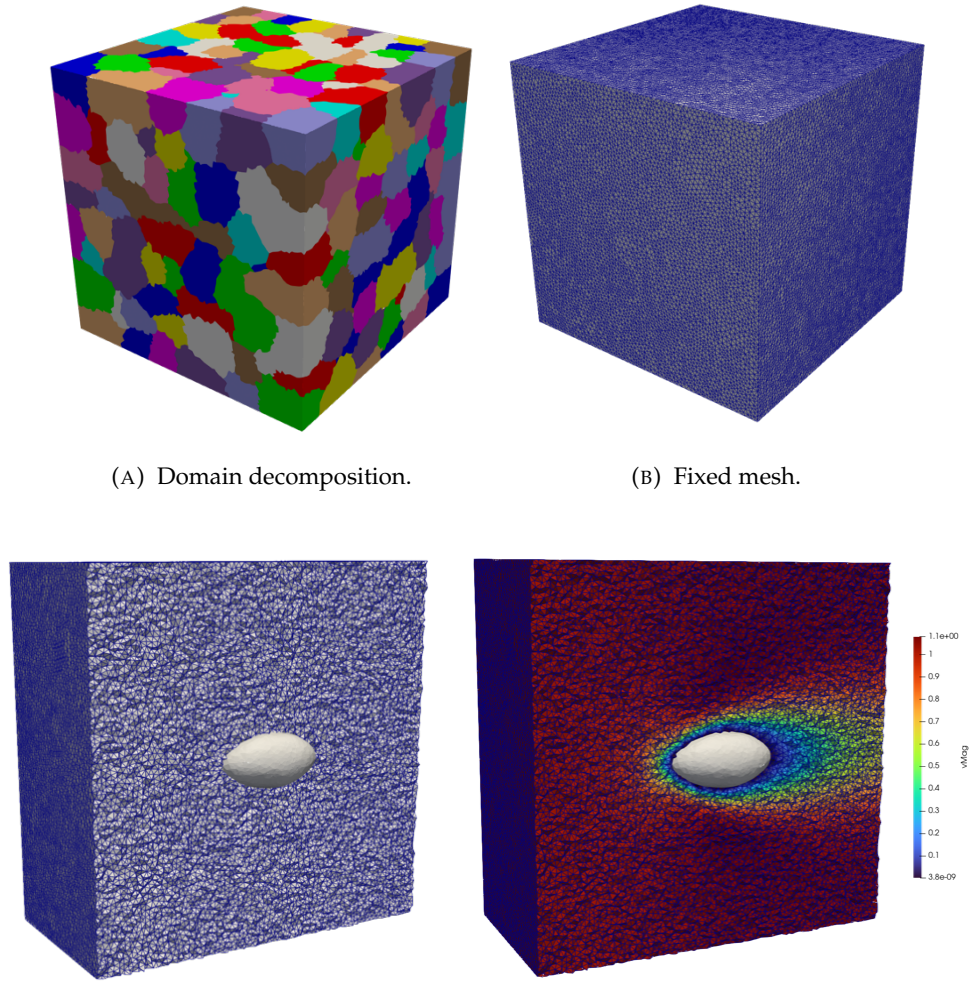

(A) Domain decomposition.

(B) Fixed mesh.

(C) Optimal solution.

(D) Velocity field.

FIGURE 5.4: Domain decomposition and parallel computing using 352 MPI processes for the fixed mesh case.

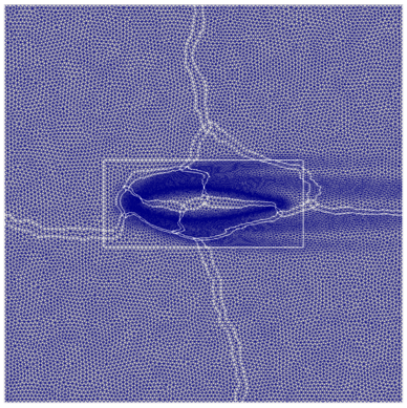

(A) Anisotropic mesh.

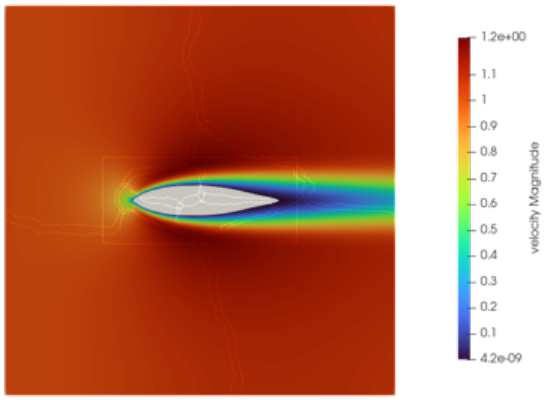

(B) Velocity field.

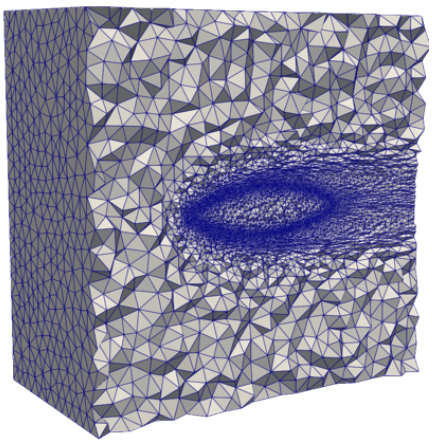

(C) Anisotropic mesh.

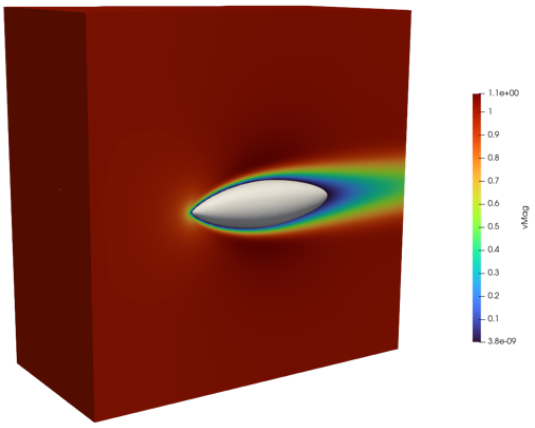

(D) Velocity field.

FIGURE 5.5: Optimal solutions for a moderately high Reynolds number ($Re = 1000$) using anisotropic mesh.

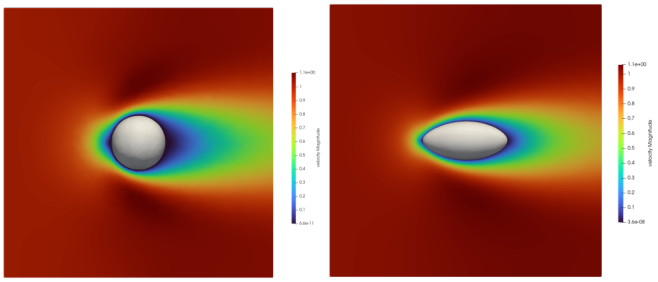

(A) Initial shape. (B) $C_0 = 1.0$.

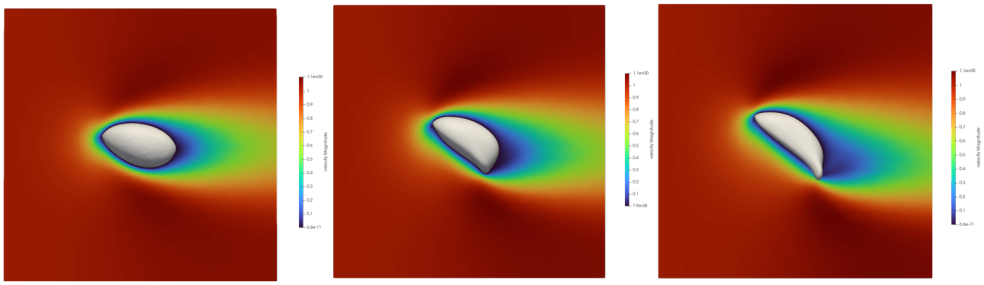

(C) $C_0 = 1.1$. (D) $C_0 = 1.3$. (E) $C_0 = 1.5$.

FIGURE 5.6: Velocity field of (a): initial shape, and optimal solutions for (b): drag minimization problem, (c)–(e): lift maximization problems.

is formulated as follows:

$$\inf_{H_\phi \in \mathcal{H}} J(\Omega) = \int_{\partial\Omega_f^D \cup \partial\Omega_f^N} \left(p + \frac{1}{2}|\boldsymbol{v}|^2 \right) (-\boldsymbol{v} \cdot \boldsymbol{n}_f)\, d\Gamma \tag{5.13a}$$

$$\text{s.t.} \begin{cases} G_1 = \dfrac{\int_D (H_\phi) d\Omega}{\int_D d\Omega} - V_{\max} = 0 \\ Eq.\ (5.1)\ \text{(Navier–Stokes equations)}. \end{cases} \tag{5.13b}$$

The adjoint equations and the sensitivity analysis can be referred to in Chapter 3. In this test case, τ is set to 10^{-3} and Δt is set to 0.1, and they are remained unchanged throughout the optimization. The "hybrid" flow modeling is used incorporated with the anisotropic adaptive mesh. The design model is shown in Fig. 5.8. The computational domain is the unit cubic $\Omega = [0;1]^3$. The radius of the in- and outlets are $\frac{1}{6}$ and $\frac{1}{12}$, respectively. The flow enters the domain from the inlet with a parabolic velocity profile $v_x = 2\left(1 - \left(36y^2 + 36z^2\right)\right)$. The flow exits the domain from the four outlets with a zero normal stress. The rest walls bear a no-slip boundary condition. The Reynolds number is set to $Re = 50$ and the maximum allowed volume fraction is set to 30%. Fig. 5.9 shows the snapshots of the channel layout during the intermediate steps. In this test case, the anisotropic mesh adaptation is used, as shown in Fig. 5.10.

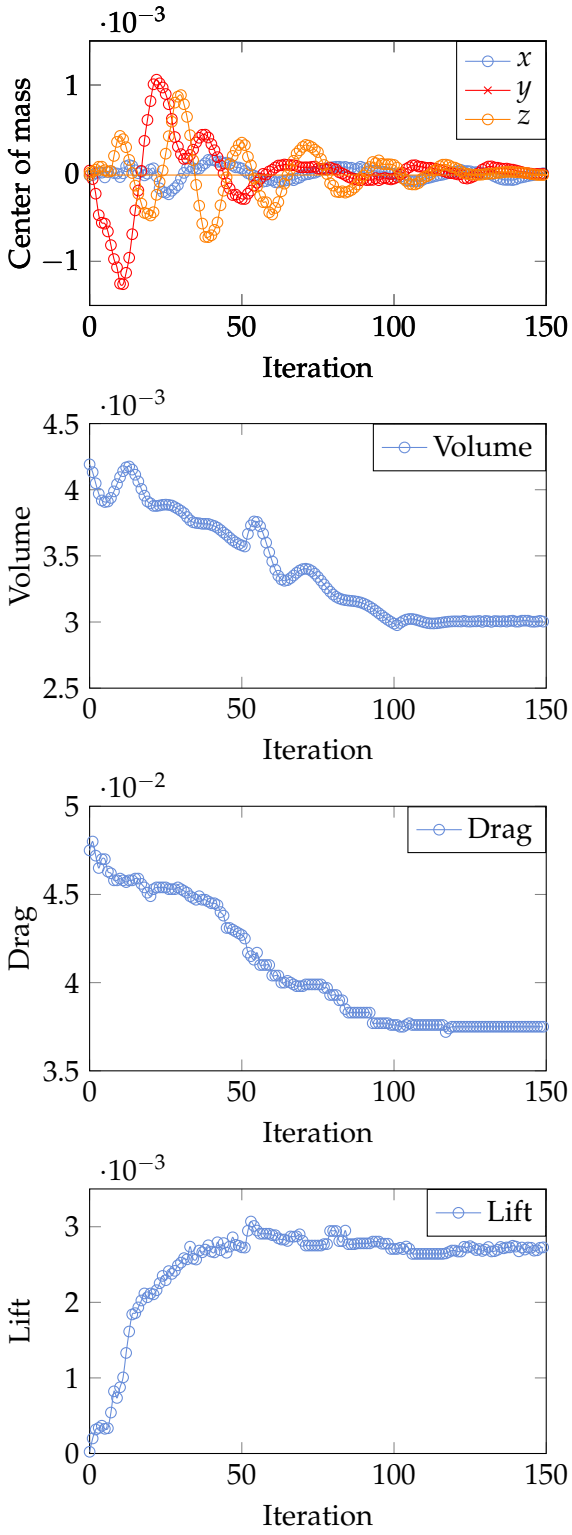

FIGURE 5.7: Iterative histories of the objective and constraint values, cf. Fig. 5.6c.

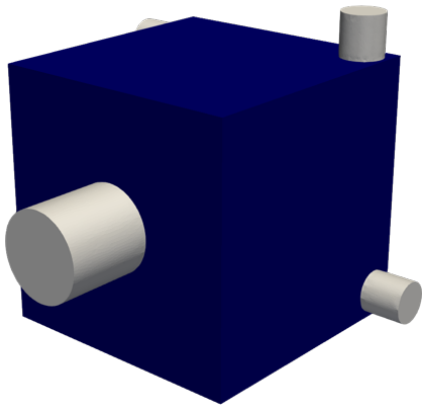

FIGURE 5.8: Design model for the 3D minimal power dissipation problem.

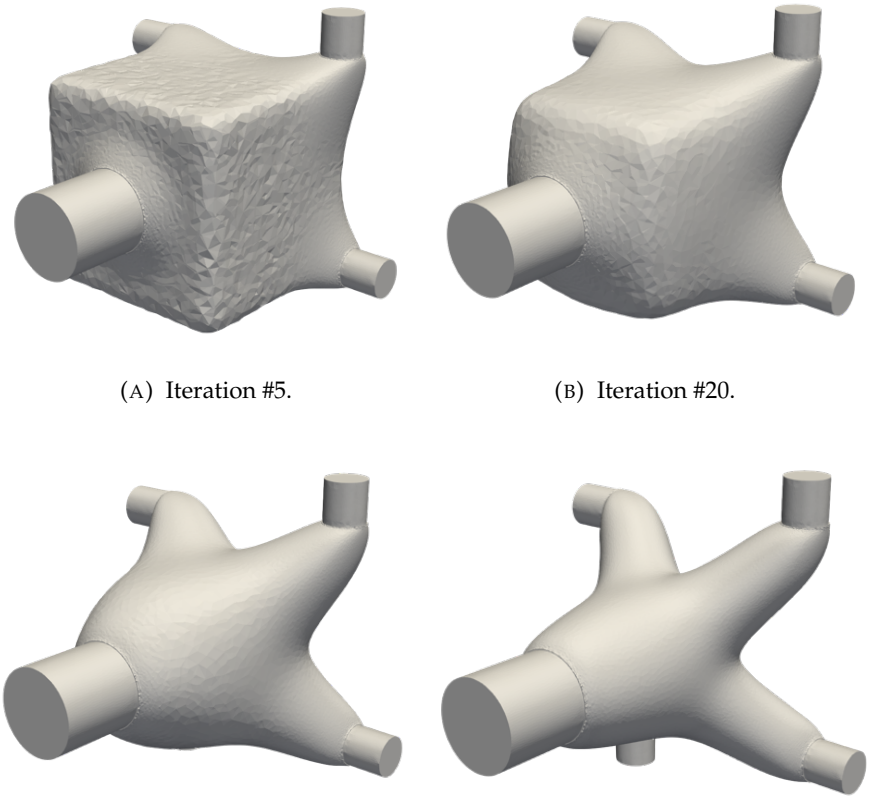

(A) Iteration #5. (B) Iteration #20.

(C) Iteration #40. (D) Optimal solution.

FIGURE 5.9: Topology evolution history of the 3D minimal power dissipation problem.

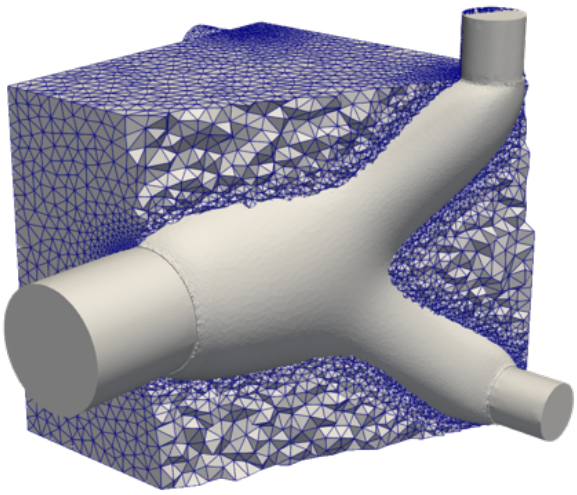

FIGURE 5.10: Cross-section view of the anisotropic mesh for the optimal configuration.

A forced convection problem

In addition to the pure fluid problem, we also test the updated algorithm to solve a thermal-fluid coupled problem. More specifically, we intend to solve a steady-state forced convection problem and find the optimal cooling channel layout which can minimize the thermal compliance under the constraints of: (1) volume, and (2) power dissipation. Therefore, the optimization mathematical model can be formulated as follows:

$$\inf_{H_\phi \in \mathcal{H}} J(\Omega) = \int_\Omega QT d\Omega \tag{5.14a}$$

$$\text{s.t.} \begin{cases} (\boldsymbol{v}\cdot\nabla)\,\boldsymbol{v} - \dfrac{1}{\mathrm{Re}}\nabla\cdot\left(\nabla\boldsymbol{v}+\nabla\boldsymbol{v}^{\mathrm{T}}\right) + \nabla p + \alpha\boldsymbol{v} = 0 & \text{in } \Omega_{\mathrm{f}} \\ -\nabla\cdot\boldsymbol{v} = 0 & \text{in } \Omega_{\mathrm{f}} \\ \mathrm{Re}\,\mathrm{Pr}\,(\boldsymbol{v}\cdot\nabla T) - \nabla\cdot(\kappa\nabla T) - Q(\boldsymbol{x}) = 0 & \text{in } \Omega \\ \boldsymbol{v} = \boldsymbol{v}_0 & \text{on } \partial\Omega_{\mathrm{f}}^D \\ \boldsymbol{v} = 0 & \text{on } \Gamma_{\mathrm{s,f}} \\ \left(-p\mathbf{I} + \dfrac{1}{\mathrm{Re}}\nabla\cdot\left(\nabla\boldsymbol{v}+\nabla\boldsymbol{v}^{\mathrm{T}}\right)\right)\cdot\boldsymbol{n}_{\mathrm{f}} = 0 & \text{on } \partial\Omega_{\mathrm{f}}^N \\ T = T_0 & \text{on } \partial\Omega_T^D \\ \kappa\nabla T\cdot\boldsymbol{n}_{\mathrm{f}} = 0 & \text{on } \partial\Omega_T^N \\ G_1 = \dfrac{\int_D H_\phi d\Omega}{\int_D d\Omega} - V_{\max} \le 0 & \\ G_2 = \Phi(\Gamma, \boldsymbol{v}(\Gamma), p(\Gamma)) - \Phi_0 \le 0, & \end{cases} \tag{5.14b}$$

where Φ denotes the power dissipation.

The design sensitivity can be derived as follows:

$$\begin{aligned}\bar{F}' = &-\frac{q_\alpha \alpha_{\max}\left(q_\alpha+1\right)}{\left(q_\alpha+H_\phi\right)^2}\boldsymbol{v}\cdot\boldsymbol{v}_A \\ &-\nabla T_A\cdot\nabla T\frac{q_\kappa\left(c_k-1\right)\left(q_\kappa+1\right)}{\left(q_\kappa+H_\phi\right)^2}+\lambda_1 \text{ in } \Omega,\end{aligned} \tag{5.15}$$

where the adjoint variables $\boldsymbol{v}_A$, p_A, and T_A are the solutions for the following adjoint equations with the adjoint boundary conditions:

$$\begin{cases} -\boldsymbol{v}\cdot\nabla\boldsymbol{v}_A+\boldsymbol{v}_A\cdot\nabla\boldsymbol{v}^{\mathrm{T}}-\dfrac{1}{\mathrm{Re}}\nabla\cdot\left(\nabla\boldsymbol{v}_A+\nabla\boldsymbol{v}_A^{\mathrm{T}}\right) & \\ \qquad +\alpha\boldsymbol{v}_A+\nabla p_A+\mathrm{Re}\,\mathrm{Pr}\,T_A\nabla T=0 & \text{in } \Omega_{\mathrm{f}} \\ \qquad -\nabla\cdot\boldsymbol{v}_A=0 & \text{in } \Omega_{\mathrm{f}} \\ Q\left(\boldsymbol{x}\right)-\mathrm{Re}\,\mathrm{Pr}\,\nabla T_A\cdot\boldsymbol{v}-\nabla\cdot\left(\kappa\nabla T_A\right)=0 & \text{in } \Omega \\ \qquad \boldsymbol{v}_A=\lambda_2\boldsymbol{v}_0 & \text{on } \partial\Omega_{\mathrm{f}}^D \\ \qquad \boldsymbol{v}_A=0 & \text{on } \Gamma_{\mathrm{s,f}} \\ -\lambda_2\left(\dfrac{1}{2}(\boldsymbol{v}\cdot\boldsymbol{v})+p\right)\boldsymbol{n}_{\mathrm{f}}-\lambda_2\boldsymbol{v}(\boldsymbol{v}\cdot\boldsymbol{n}_{\mathrm{f}})+\boldsymbol{v}_A(\boldsymbol{v}\cdot\boldsymbol{n}_{\mathrm{f}}) & \\ \qquad +\dfrac{1}{\mathrm{Re}}\left(\nabla\boldsymbol{v}_A+\nabla\boldsymbol{v}_A^{\mathrm{T}}\right)\cdot\boldsymbol{n}_{\mathrm{f}}-p_A\boldsymbol{n}_{\mathrm{f}}=0 & \text{on } \partial\Omega_{\mathrm{f}}^N \\ \qquad T_A=0 & \text{on } \partial\Omega_T^D \\ \qquad \left(\mathrm{Re}\,\mathrm{Pr}\,T_A\boldsymbol{v}+\kappa\nabla T_A\right)\cdot\boldsymbol{n}_{\mathrm{f}}=0 & \text{on } \partial\Omega_T^N, \end{cases} \tag{5.16}$$

The sensitivity analysis is quite similar to that of natural convection problem and can be referred to in Appendix A.2.

Considering a cavity whose dimension is $[0;1]^3$, a uniform body heat source Q_0 is applied in the computational domain. The blue region is the design domain while the white regions are the inlet and outlet. The objective functional is the thermal compliance $\int_D Q_0 T d\Omega$. Fig. 5.11b shows the optimal cooling channel layout under a volume constraint and a power dissipation constraint. To further demonstrate the mesh adaptivity ability, we show the cross-section views of the anisotropic mesh and velocity profiles at three different xy-planes, see Fig. 5.12.

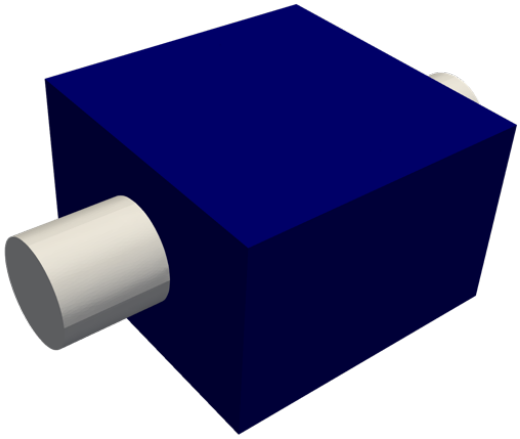

(A) Design model.

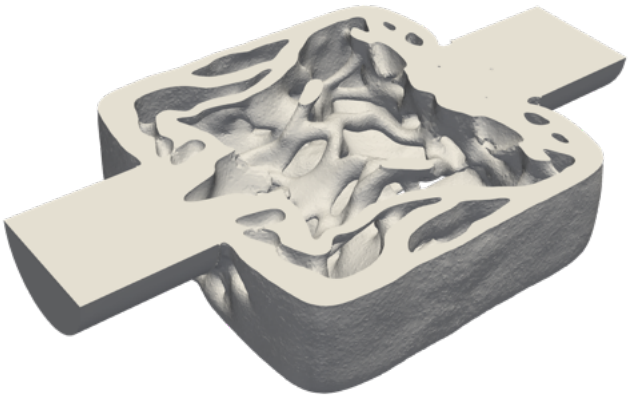

(B) Optimal cooling channel layout.

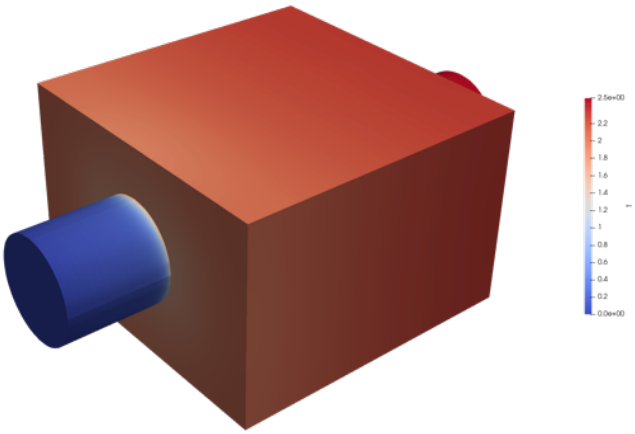

(C) Temperature field.

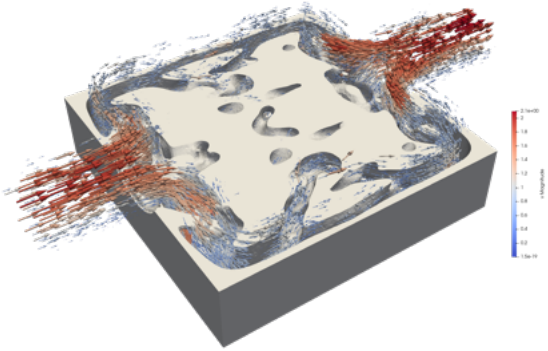

(D) Velocity glyph.

FIGURE 5.11: A three-dimensional test case for a forced convection problem (an ongoing work).

5.5 Summary

This chapter reports on the recent increments to the RDE-based TO framework. The main motivation is to break through the existing bottleneck of the sequentially performed body-fitted mesh evolution method, as well as to investigate the effects of different meshing and flow modeling strategies on the fluid-based topology optimization in terms of the computational cost and the analysis accuracy.

First, we recall the basic concept of the RDE-based TO method. Next, we present four different meshing techniques: fixed mesh, isotropic adaptive mesh, anisotropic adaptive mesh, and body-fitted adaptive mesh, together with two different flow modeling strategies: "separate" and "hybrid" modeling, followed by the implementation details. To demonstrate the workflow of the proposed methodology, we solve a lift-drag and a minimal power dissipation optimization problem by showcasing various 2D/3D, small-/large-scale numerical examples. The main findings are summarized as follows:

1. With the "separate" modeling strategy incorporated with body-fitted mesh, we can iteratively disjoin-reunion the computational domains through a geometry trimming process. This enables us to impose the no-slip boundary condition on the moving fluid–solid interface. However, for each iteration, it requires us to initialize the flow field by the solution of the Stokes flow, followed by repeatedly solving the Newton iteration for a series of Reynolds number until it reaches the target Reynolds. Furthermore, the body-fitted mesh adaptation is performed sequentially on a single MPI process, which is so far a bottleneck for solving large-scale problems.

2. The "hybrid" modeling strategy, relying on the fictitious body force term to mimic an immersed solid phase in an integrated domain, has its drawbacks for those problems where the pressure diffusion inside the solid phase can be problematic, e.g., fluid–structure interaction (FSI) problem. However, except in these specific cases, in general, this fictitious body-force term is not a too big issue for other fluid-based optimization problems. The comparison results show that we can obtain the practically identical solutions using either flow modeling strategy ("hybrid" or "hybrid") with different meshing techniques.

3. With the "hybrid" modeling, over 70% runtime-saving is reported compared with the "separate" modeling. This is partly due to the fact that the iso-/anisotropic mesh adaptation can be performed in a distributed fashion, partly due to a huge decrease in the Newton iteration number.

4. A large-scale 3D test case (using fixed mesh) with a total tetrahedra number of $3.12 \cdot 10^6$, having approximately $1.32 \cdot 10^7$ degrees of freedom for the linearized fluid system, is solved using a cluster mounted with 352 MPI processes, confirming the scalability of the proposed framework.

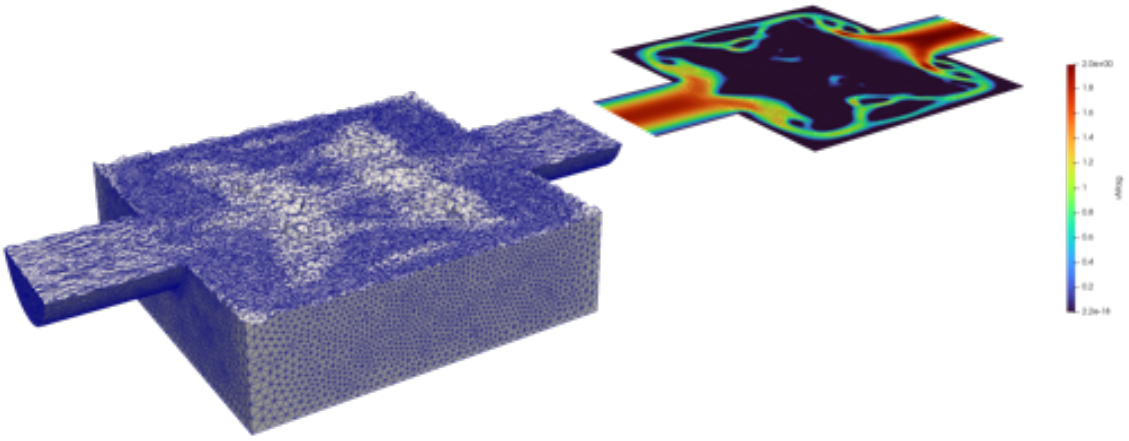

(A) $z = -0.05$.

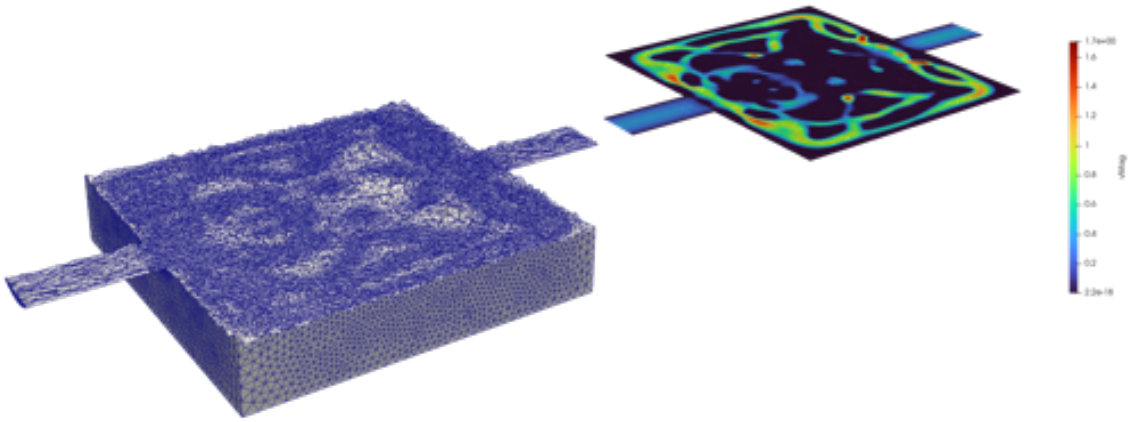

(B) $z = -0.15$.

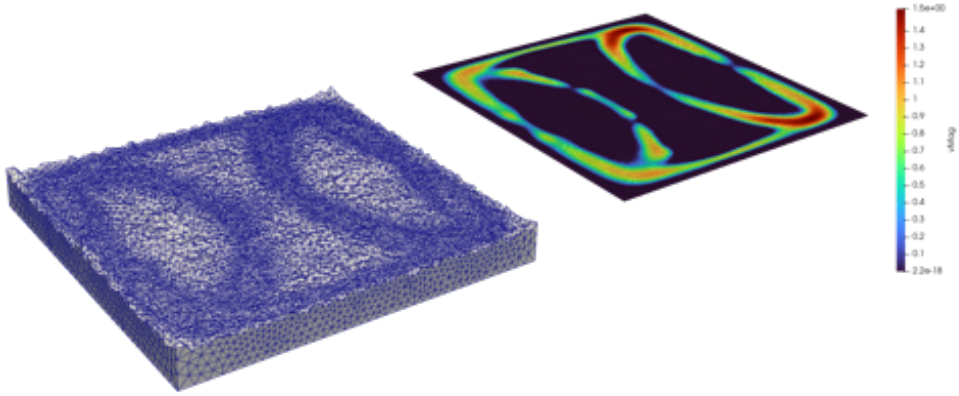

(C) $z = -0.25$.

FIGURE 5.12: Cross-section views of anisotropic mesh (left) and velocity profiles (right) at different xy-planes.

5. The RDE-based level-set method enables not only shape but also topology evolution. This feature is supported by a numerical verification example for the minimal power dissipation problem.

We intend to conduct future research by applying the proposed framework to the design of a heat exchanger. Since the iso-/anisotropic mesh adaptation can be performed in parallel, we can expect a more efficient solver which is capable of handling a complex channel layout.

As a final remark of this chapter, we conclude that several issues concerning fluid-related TO are far from being resolved, and there are two main limitations of the approach (in its current form). (1) Despite the fact that the stabilized FEM has grown to be a mature and accurate discretized method, the FVM has been the preferred one for computational fluid dynamics (Bazilevs, Takizawa, and Tezduyar, 2015). (2) The other issue not discussed here is the use of the continuous adjoint method for sensitivity analysis, which may introduce some discretization errors with respect to the exact sensitivities (Yu, Ruan, Gu, Ren, Li, Wang, and Shen, 2020). In case of two equation-based turbulence models, the exact sensitivities are vital (Dilgen, Dilgen, Fuhrman, Sigmund, and Lazarov, 2018a). This will be a topic for future investigations, aimed at the application in higher Reynolds cases. This chapter can be a helpful discussion for such further research, aimed at including fluid flows in large-scale TO.

Chapter 6

Topology Optimization of Lattice Structures[†]

CONTENTS

6.1 Introduction

In general, TO techniques are used to find an optimal solution which can maximize the performance. However, the generative designs with the highest performance may sometimes contradict the aesthetic and/or other specific functional requirements. For example, in the architectural design, the structures should meet the minimum performance criteria, but the performance maximization is not the only consideration. Architects usually need to choose the final design from multiple design candidates from an aesthetic perspective. Yang, Zhao, He, Zhou, Zhou, Huang, and Xie (2019) proposed five different strategies to achieve diverse and competitive designs based on the concept of penalizing elemental sensitivities. Later in the work by He, Cai, Zhao, and Xie (2020), they presented a stochastic approach for a similar purpose. Besides the aesthetic motivation, the visibility constraints can be another crucial consideration, such as skyscrapers (Besserud, Katz, and Beghini, 2013). Dapogny, Faure, Michailidis, Allaire, Couvelas, and Estevez (2017) formulated three different constraints on the geometry of shapes, one of which allows to control

[†]The work in this chapter has been submitted to *Advances in Engineering Software* (Elsevier).

the visibility of structures, and to penalize the length of bars or the areas of extended surfaces of shapes. The second typical instance is the design of implants. Lattice structures may not outperform the classical macroscopic TO designs (Wu, Aage, Westermann, and Sigmund, 2017), however, in the bio-system, the porosity of lattice structures will not impede the interaction between the solid implants and the surrounding biofluidic environment (Birmingham, Grogan, Niebur, McNamara, and McHugh, 2013). The biodegradation process will be able to happen naturally due to the chemical reactions (Barzegari, Mei, Lamaka, and Geris, 2021). Therefore, an orthopedic implant with well-designed lattice structure and/or functionally graded materials can facilitate the bone healing process (Mahmoud and Elbestawi, 2017). Zhang, Takezawa, Ding, Xu, Li, and Guo (2021) firstly presented the TO design of stiffness changeable structures considering material degradation. In their later work (Zhang, Takezawa, Ding, Xu, Duan, Li, and Guo, 2021), they extended this idea to the microscopic composite structure design and verified its ideal performance of the optimized composite structures. Another application scenario is that during the design process of the key components of an aircraft, some redundant loading paths should remain due to safety concerns. If a small portion of the loading path breaks due to fatigue failure, the remaining component can still fulfill the fail-safe requirements. In Kranz, Lüdeker, and Kriegesmann (2021), they considered maximum stress as the optimization objective and adopted a common and easy-to-implement maximum length scale constraint approach. They obtained redundant lattice structures and the fail-safe properties were evaluated by comparing against the explicit fail-safe approach. With this in mind, structures with some redundant features may not have the highest performance, but still, they have their own unique advantages in many applications.

Motivated by the need for porous structure in the design of biodegradable implants, as well as for the diverse and competitive structural designs in the architecture, this chapter sheds a light on the topology optimization of lattice structures. Among the literature, the existing TO methodologies can be broadly classified into three categories: (1) single-scale approach (Wu, Aage, Westermann, and Sigmund, 2017; Wu, Clausen, and Sigmund, 2017; Yi, Zhou, Yoon, and Saitou, 2019; Dou, 2020; Qiu, Jin, Jin, Wang, Xia, Zhu, and Shi, 2020; Kambampati and Kim, 2020; Träff, Sigmund, and Aage, 2021; Kranz, Lüdeker, and Kriegesmann, 2021; Zhou, Lu, Liu, and Lin, 2022; Gerzen, Mertins, and Pedersen, 2022), (2) concurrent approach (Radman, Huang, and Xie, 2013; Zhang, Ding, Li, and Xiong, 2019; Zhang, Takezawa, Ding, Guo, Ni, and Zhang, 2021; Ferro, Perotto, and Gavazzoni, 2022), and (3) inverse (or dehomogenization) (Pantz and Trabelsi, 2008; Allaire, Cavallina, Miyake, Oka, and Yachimura, 2019; Allaire, Geoffroy-Donders, and Pantz, 2019; Groen, Stutz, Aage, Bærentzen, and Sigmund, 2020; Geoffroy-Donders, Allaire, and Pantz, 2020; Dede, Zhou, and Nomura, 2020; Lee, Kwon, Yoo, Min, Nomura, and Dede, 2021; Zhou, Lohan, Zhou, Nomura, and Dede, 2022) methods. Please note that those categories, based on the different criteria, can be classified differently. For example, the readers are referred in the review paper to Wu, Sigmund, and Groen (2021) for more detailed and meticulous records and classification of multi-scale structures TO.

The first option is that of the single-scale approach. This approach is essentially a macroscopic

TABLE 6.1: Computational techniques in the state-of-the-art TO developments in the single-scale approaches.

Ref.	Design	TO	Local Averaged Density	2D/3D	Mesh Type
Wu, Aage, Westermann, and Sigmund (2017)	Lattice	Density	Explicit	2D/3D	Quadrilateral/hexahedral
Wu, Clausen, and Sigmund (2017)	Shell-infill	Density	PDE	2D	Quadrilateral
Yi, Zhou, Yoon, and Saitou (2019)	Lattice	Density	PDE	2D	Quadrilateral
Dou (2020)	Lattice	Density	Explicit	2D	Quadrilateral
Qiu, Jin, Jin, Wang, Xia, Zhu, and Shi (2020)	Shell-infill	BESO	Explicit	2D	Quadrilateral
Kambampati and Kim (2020)	Flow channel	LSM	Explicit	2D/3D	Quadrilateral/hexahedral
Träff, Sigmund, and Aage (2021)	Shell	Density	PDE	3D	Shell-element
Kranz, Lüdeker, and Kriegesmann (2021)	Lattice	Density	Explicit	2D	Quadrilateral
Zhou, Lu, Liu, and Lin (2022)	Shell-infill	Density	Explicit	2D	Quadrilateral
Gerzen, Mertins, and Pedersen (2022)	Lattice	Density	Explicit	2D/3D	Quadrilateral
This work	Lattice	LSM	PDE	2D/3D	Triangular/Tetrahedral

TO, and it is easy-to-implement, thus can be applied to any physics straightforwardly. In general, it does not require additional efforts for the reconstruction of the design results. However, it also has several drawbacks. As we shall show later in this chapter, this approach requires high computational cost, especially for the case of a large size macroscopic structure with small size lattice features. Wu, Aage, Westermann, and Sigmund (2017) pioneered the idea of applying a local volume constraint at a single macroscopic scale. In this seminal work, the local volume fraction is computed by measuring the average density over all voxels in a prescribed neighborhood. In their later work (Wu, Clausen, and Sigmund, 2017), they extended this approach for generating simultaneously optimized shells and infill in the context of minimum compliance TO. They adopted a PDE-filter for computing the averaged local density. Built upon these pioneering works, several researchers have reported successful applications. For example, Yi, Zhou, Yoon, and Saitou (2019) further considered buckling constraints, so that the design results can minimize compliance while enhancing the structural stability against buckling failure. Träff, Sigmund, and Aage (2021) constructed a high performance computing framework for ultra large scale, shell-element based topology optimization. They presented excellent design results for civil engineering and aerospace engineering examples by solving shell TO problems with up to 11 million shell elements on 800 cores. Kambampati and Kim (2020) presented one of the very few level-set methods considering the maximum length scale constraint. They adopted a Darcy flow model, also known as "Poor man's" approach (Zhao, Zhou, Sigmund, and Andreasen, 2018), to optimize 2D and 3D cooling channel layout. Zhou, Lu, Liu, and Lin (2022) shed a light on the design of shells with self-supporting infills for additive manufacturing (AM). They proposed an overhang constraint and a two-field based formulation to control the minimum length scale, followed by a model reconstruction to an output boundary represented geometry. Finally, and very recently, Gerzen, Mertins, and Pedersen (2022) derived a theoretical framework for considering geometrical constraints in the context of a density-based approach. They confirmed the validity of their framework by showcasing 2D and 3D lattice or membrane-like structures. We summarize in Table 6.1 the computational techniques in the state-of-the-art TO developments in the single-scale approaches.

The second and third categories can be regarded as multi-scale approaches. The second category is the concurrent topology optimization approach. This approach has attracted an increased interest in the design of functionally graded cellular structures. The homogenized material property tensor is a function of the fraction of solid material within each unit cell, and the topological change in unit cells can be reflected in the macroscopic structural response. The designer can choose to use single (or periodic) unit cells and allocate them appropriately in the macroscopic design domain (Zhang, Ding, Li, and Xiong, 2019). A higher design flexibility can be achieved by making the microscopic infill spatially vary in topology and characteristics. However, this can also lead to a high computational cost (Radman, Huang, and Xie, 2013; Zhang, Takezawa, Ding, Guo, Ni, and Zhang, 2021). A typical issue is to get well-connected neighborhood unit cells and this drawback has been addressed in many ways in the literature. For example, very recently, a preprint was uploaded to *arxiv.org* by Ferro, Perotto, and Gavazzoni (2022). They solved a Stokes-type TO problem on a narrow morphing region to achieve smooth connection between neighborhood unit cells.

The third option is the homogenization design method which is undergoing a resurrection in recent years since the pioneering work by Pantz and Trabelsi (2008). The key idea is to restore the optimized micro-structure at a selected length scale to get a global and detailed picture of the micro-structure, once an optimized composite structure is obtained (Allaire, Cavallina, Miyake, Oka, and Yachimura, 2019). In this approach, the micro-structure is restricted to be orthotropic with a few geometric variables. But the sacrifice in design flexibility can reduce the huge amount of computational cost. For example, in the work by Groen, Stutz, Aage, Bærentzen, and Sigmund (2020), comparisons with density-based single-scale approach show a reduction in computational cost of 3 orders of magnitude, making it possible for giga-scale designs on a standard PC. Another core interest behind this is how to recover micro-structures with good connectivity. To this end, Lee, Kwon, Yoo, Min, Nomura, and Dede (2021) partitioned the design domain into several subdomains, and they used different mapping functions at each subdomain. The mapping functions at the transition zone are adjusted to ensure the connectivity of restored micro-structures. Besides the structural optimization problems, the authors also notice that very recently some researchers have adopted the dehomogenization method in the context of fluid-related TO (Dede, Zhou, and Nomura, 2020). For example, in Zhou, Lohan, Zhou, Nomura, and Dede (2022), they projected the optimized porous media performance by means of intricate micro-channel structures in a post-processing step based on the reaction–diffusion equation.

As briefly discussed above, the three different categories have their own merits and demerits. This chapter builds upon the recent advancements in the first category (macroscopic TO with maximum length scale constraint) and develops a footprint in that direction. As summarized in Table 6.1, first, the density-based approach outnumbers other TO methods with 8 works or 80%. This is partly because the density-based approach is more capable of generating feature-rich shapes, starting from scratch. For this reason, very few works have contributed to the LSM in the context of lattice design. Second, most of the existing works presented only small-scale

2D academic examples with 7 works or 70%. Unlike 2D cases, the large-scale 3D cases require substantial algorithm effort, i.e., a fully distributed framework (including scalable domain decomposition, matrix assembly, parallel interpolation, linear solver) that very few general purpose libraries offer. Third, it is known that the arbitrary geometries and complex boundary conditions can be conveniently handled with unstructured meshes (Lin, Liu, and Wei, 2022). However, to this date, most of the works have adopted structured meshes. Forth, the key ingredient of the single-scale approach is to compute the local averaged density. Seven works or 70% utilized the explicit knowledge of the neighborhood elements to compute the exact averaged density value. However, such an explicit method limits its application to the unstructured mesh and/or adaptive mesh-based TO framework. To overcome this problem, some researchers used the variational method (also known as the fictitious physics model) for the simplification of the numerical evaluation of geometric constraints (Feppon, Allaire, Dapogny, and Jolivet, 2021; Yamada and Noguchi, 2022), though it may sometimes be less accurate than the explicit method.

Aiming at the above-mentioned gaps, this chapter proposes a level set-based method for topology optimization of high resolution lattice structures which is the first attempt in that direction. The main idea is to introduce the maximum length scale constraint, realized by a PDE-filter, into the reaction–diffusion equation (RDE)-based LSM which allows us to design from scratch. Then, this technique is coupled with the distributed computing algorithms based on PETSc, implemented in an open-source software FreeFEM using unstructured and/or adaptive meshes, to deliver two- and three-dimensional designs with complex-shape geometry. The parallel efficiency is validated by solving large-scale 3D benchmarks with 20 million elements on a cloud-based cluster.

The remainder of this chapter is organized as follows. Section 6.2 describes the mathematical and physics frames including the level set-based TO method, maximum length scale constraint by a PDE-filter and mathematical formulation of the optimum design problem. In Section 6.3, we illustrate the numerical implementation details including the finite element modeling, parallel computing, and the optimization algorithm. Section 6.4 presents several two- and three-dimensional large-scale test cases. Lastly, we document in Section 6.5 the conclusion and prospective works.

6.2 Formulation

In Section 6.2.1, we introduce the maximum length scale constraint based on a PDE-filter. Next, we formulate the optimum design problem for the lattice infill in Section 6.2.2.

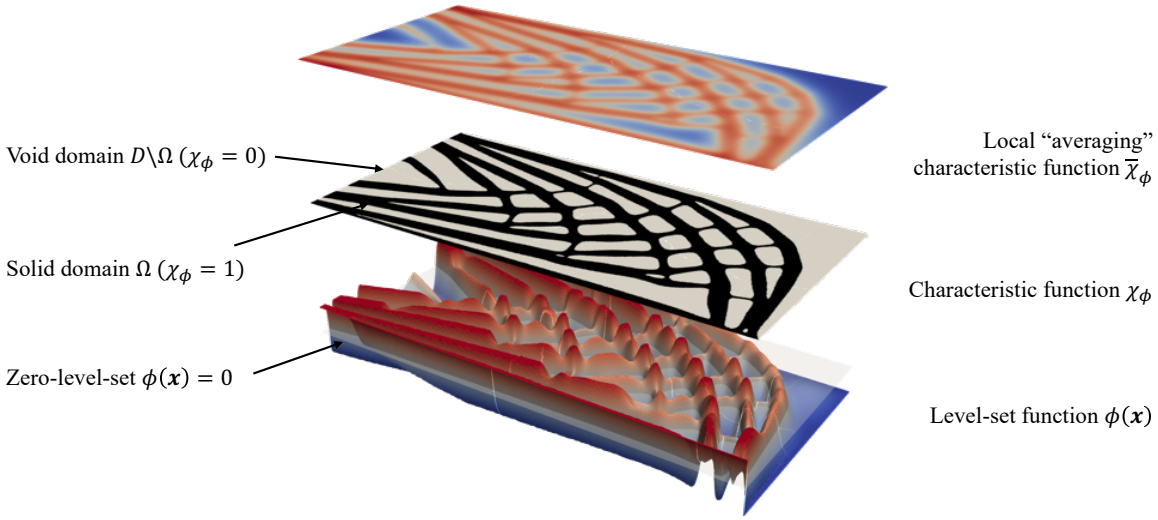

FIGURE 6.1: Schematic of the level-set function $\phi(x)$, characteristic function χ_ϕ, and local "averaging" characteristic function $\bar{\chi}_\phi$. (For interpretation of the references to colour in this figure legend, the reader is referred to the web version of this article.)

6.2.1 Maximum length scale constraint

To mimic the porous structures in natural systems, the geometrical constraint is introduced. In this chapter, we adopt the idea of Wu, Aage, Westermann, and Sigmund (2017) by imposing a maximum allowable volume fraction to the local averaged value of the characteristic function $\bar{\chi}$, see the top layer as shown in Fig. 6.1. Using the $p-$norm function to approximate the maximum value of $\bar{\chi}$, the local volume can be then calculated per the design variable and aggregated by p-mean as

$$\max_{\forall i}\left(\bar{\chi}_i\right) \approx \|\bar{\chi}_i\|_p = \left(\frac{1}{n}\sum_{i=1}^{n}\bar{\chi}_i^p\right)^{1/p} \leq \bar{V}_{\max}, \tag{6.1}$$

where n is the total number of nodes[1] in the design domain and $\bar{V}_{\max}$ is the maximum allowable local volume fraction. When p goes to infinity, $\max\left(\bar{\chi}\right) = \|\bar{\chi}\|_p$, but a large value of p will lead to numerical instability. Therefore, we set $p = 10$ in this chapter. Note that since $p-$norm approximation cannot represent the max function in a fully accurate way, at some places where the stress is very high, we may observe the exceeding values.

The primary idea to compute this local volume fraction is to measure the percentage of solid voxels over all voxels in a prescribed neighborhood $\mathbb{N}_e$ (Wu, Aage, Westermann, and Sigmund,

[1]Using the FEM, the design domain is discretized into N elements with n vertices (or nodes). In many researches, the uniform characteristic function of each element is defined as a design variable. In this chapter, the design variables are defined at nodes and a linear interpolation scheme is used to obtain the value within an element. See `P1` element in `https://doc.freefem.org/documentation/finite-element.html#p1-element`. This ensures the continuity of the design variables (Zhu, Zhang, Li, Liang, Wang, Li, and Nishiwaki, 2021).

2017; Kambampati and Kim, 2020).

$$\bar{\chi} = \frac{\sum_{i \in \mathbb{N}_e} \chi_i}{\sum_{i \in \mathbb{N}_e} 1} \tag{6.2a}$$

$$\mathbb{N}_e = \{i | \ \|\boldsymbol{x}_i - \boldsymbol{x}_e\| \leq r\}, \tag{6.2b}$$

where r is the prescribed radius. This approach requires the explicit knowledge of the spatial information of the neighborhood elements located in the design domain, which limits its application to the unstructured mesh and/or adaptive mesh-based TO framework. In order to overcome this problem, we use a PDE-filter (Lazarov and Sigmund, 2011; Kawamoto, Matsumori, Yamasaki, Nomura, Kondoh, and Nishiwaki, 2011) to compute the local average value $\bar{\chi}$, as given in Eq. (6.3). Though this filtering technique has been adopted in several density-based approach works (Wu, Clausen, and Sigmund, 2017; Yi, Zhou, Yoon, and Saitou, 2019; Träff, Sigmund, and Aage, 2021), it has seldom been used in the LSM in the context of lattice designing and this work is the first step in this direction. Moreover, the use of this PDE-filter makes the distributed computing quite straightforward (Lazarov and Sigmund, 2011; Kawamoto, Matsumori, Yamasaki, Nomura, Kondoh, and Nishiwaki, 2011), which will be detailed in later sections.

$$\begin{cases} -r^2\nabla^2\bar{\chi} + \bar{\chi} = \chi & \text{in } \Omega \\ \nabla\bar{\chi} \cdot \boldsymbol{n} = 0 & \text{on } \partial\Omega. \end{cases} \tag{6.3}$$

where χ is the binalized characteristic function. The schematic of the local "averaging" characteristic function $\bar{\chi}$ is shown in Fig. 6.1, seen in the top layer of this schematic.

6.2.2 Optimum design problem for the lattice infill

The context of interest is that of topology optimization of lattice infills. We intend to find an optimal structure which can minimize the mean compliance (or maximize the stiffness) under a global and/or a local averaging volume constraint. The governing equation underlying the displacement $\boldsymbol{u}$ can be formulated by the Lamé's equation under the assumptions that: (1) small displacements and deformations are observed (linear elasticity), and (2) the body-force and gravity are neglected. Therefore, the optimization mathematical model can be formulated as

$$\inf_{\chi_\phi \in \mathcal{X}} J(\Omega) = \int_{\partial\Omega_s^N} \boldsymbol{g} \cdot \boldsymbol{u} d\Gamma, \tag{6.4a}$$

$$\text{s.t.} \begin{cases} -\operatorname{div}(\mathbb{C}_{\chi_\phi} : e(\boldsymbol{u})) = 0 & \text{in } \Omega \\ \boldsymbol{u} = \boldsymbol{u}_0 & \text{on } \partial\Omega^D \\ (\mathbb{C} : e(\boldsymbol{u})) \cdot \boldsymbol{n}_s = \mathbf{g} & \text{on } \partial\Omega^N \\ G_1 = \dfrac{\int_D \chi d\Omega}{\int_D d\Omega} - V_{\max} \leq 0 & \\ G_2 = \left(\dfrac{1}{n}\sum_{i=1}^n \bar{\chi}^p\right)^{1/p} - \bar{V}_{\max} \leq 0 & \\ -r^2\nabla^2\bar{\chi} + \bar{\chi} = \chi & \text{in } \Omega \\ \nabla\bar{\chi} \cdot \boldsymbol{n} = 0 & \text{on } \partial\Omega, \end{cases} \tag{6.4b}$$

where $\mathbb{C}$ is the fourth-order elasticity tensor, $\boldsymbol{g}$ is the surface traction, and $e(\boldsymbol{u})$ is the linearized strain tensor. Using the characteristic function χ_ϕ, the elasticity tensor $\mathbb{C}$ can be expanded as

$$\mathbb{C}_{\chi_\phi} = \chi_\phi (\mathbb{C}_\mathrm{s} - \mathbb{C}_\mathrm{v}) + \mathbb{C}_\mathrm{v}, \tag{6.5}$$

$V_{\max}$ and $\bar{V}_{\max}$ in Eq. (6.4) are the maximum allowed global and local averaging volume fractions for the solid phase, respectively.

The mean compliance problem governed by the linear elasticity is known to be self-adjoint. Therefore, the topological sensitivity $\mathcal{F}'$ can be derived as follows:

$$\mathcal{F}' = -\left(e(\boldsymbol{u}) : \mathbb{C}_{\chi_\phi}\right) : e(\boldsymbol{u}) + \lambda_1 + \lambda_2\mathcal{G}', \tag{6.6}$$

where λ_1 and λ_2 are the Lagrange multipliers associated to the global and local averaging volume constraints, respectively. In the present work, $\lambda_{1,2}$ are updated using the augmented Lagrangian method. The updating scheme is given as follows:

$$\lambda_i^{n+1} = \lambda_i^n + c_1 G_i^n + c_2\left(G_i^{n-1} - G_i^n\right), \tag{6.7}$$

where c_1 and c_2 are the constant coefficients. Both G_1 and G_2 are relaxed, and they are gradually tightened until a given iterative step, in order to stabilize the optimization process.

We denote by $\mathcal{G}'$ in Eq. (6.6) the sensitivity associated to the local averaging volume constraint, $\mathcal{G}' = \frac{\delta G_2}{\delta\chi}$, and it can be computed as the solution of Eq. (6.8).

$$\begin{cases} -r^2\nabla^2\mathcal{G}' + \mathcal{G}' = \dfrac{\partial G_2}{\partial\bar{\chi}} & \text{in } \Omega \\ \nabla\mathcal{G}' \cdot \boldsymbol{n} = 0 & \text{on } \partial\Omega, \end{cases} \tag{6.8}$$

where $\dfrac{\partial G_2}{\partial\bar{\chi}}$ is expressed as

$$\frac{\partial G_2}{\partial\bar{\chi}} = \frac{\bar{\chi}^{p-1}\left(\dfrac{1}{n}\sum\bar{\chi}^p\right)^{\frac{1}{p}-1}}{n}. \tag{6.9}$$

The sensitivity analysis of the local volume constraint can be found in Appendix A.3. Note that this constraint is independent to the physics. In other words, the deduced sensitivity $\mathcal{G}'$ can be used in a different TO problem governed by any other constitutive laws.

6.3 Implementation details

6.3.1 Finite element modeling

We use the finite element method to solve the PDEs mentioned in Section 6.2. We set the classical Hilbert spaces $\mathscr{U}$ for the displacement $\boldsymbol{u}$, and $\mathscr{P}$ for the level-set function ϕ, characteristic function χ, local averaged characteristic function $\bar{\chi}$, and sensitivity for the local volume constraint $\mathcal{G}'$, as follows:

$$\begin{aligned} \mathscr{U} &:= \left\{ \tilde{\boldsymbol{u}} \in H^1\left(\Omega, \mathbb{R}^d\right) \mid \tilde{\boldsymbol{u}} = 0 \text{ on } \partial\Omega_s^D \right\} \\ \mathscr{P} &:= \left\{ \tilde{p} \in H^1(\Omega) \mid \tilde{p} = 0 \text{ on } \partial\Omega_p^D \right\}. \end{aligned} \tag{6.10}$$

First, the governing equation can be expressed in the weak form as:

$$\begin{aligned} -\int_\Omega (e(\boldsymbol{u}) : \mathbb{C}_{\chi_\phi}) : e(\tilde{\boldsymbol{u}}) d\Omega + \int_{\partial\Omega^N} \boldsymbol{g} \cdot \tilde{\boldsymbol{u}} d\Gamma = 0 \\ \forall \tilde{\boldsymbol{u}} \in \mathscr{U}, \boldsymbol{u} \in \mathscr{U}. \end{aligned} \tag{6.11}$$

Second, the PDE-filter defined in Eq. (6.3) is expressed in the weak form as

$$\int_\Omega r^2 \nabla\tilde{\bar{\chi}} \cdot \nabla\bar{\chi} + \tilde{\bar{\chi}}\bar{\chi} - \tilde{\bar{\chi}}\chi d\Omega = 0 \quad \forall \tilde{\bar{\chi}} \in \mathscr{P}, \bar{\chi} \in \mathscr{P} \tag{6.12}$$

Third, similar to the PDE-filter, the adjoint equation defined in Eq. (6.8) is expressed in the weak form as

$$\int_\Omega r^2 \nabla\tilde{\mathcal{G}}' \cdot \nabla\mathcal{G}' + \tilde{\mathcal{G}}'\mathcal{G}' - \tilde{\mathcal{G}}' \frac{\partial G_2}{\partial \bar{\chi}} d\Omega = 0 \quad \forall \tilde{\mathcal{G}}' \in \mathscr{P}, \mathcal{G}' \in \mathscr{P}. \tag{6.13}$$

In Eqs. (2.36) and (6.11) to (6.13), $\tilde{\boldsymbol{u}}$, $\tilde{\bar{\chi}}$, $\tilde{\mathcal{G}}'$, and $\tilde{\phi}$ are the test functions for $\boldsymbol{u}$, $\bar{\chi}$, $\mathcal{G}'$, and ϕ, respectively.

6.3.2 Distributed computing

To implement the weak formulations in Section 6.3.1, an open-source finite element software FreeFEM[2] (Hecht, 2012; Jolivet, Dolean, Hecht, Nataf, Prud'homme, and Spillane, 2012) is used for the discretization of those PDEs. FreeFEM is a high-level programming language, internally

[2] http://www.freefem.org/.

written in C++ and its syntax is close to the mathematical formulations, which thus makes the coding quite straightforward. For parallelism, it relies on the Message Passing Interface (MPI).

Since we target large-scale 3D problems, the most time consuming part in this workflow lies in the solution of the sequence of linear systems of the form $Ax = b$. To accelerate the overall computation, we use an overlapping Schwarz domain decomposition method to solve the linear systems in a distributed fashion. To this end, we use PETSc (Abhyankar, Brown, Constantinescu, Ghosh, Smith, and Zhang, 2018; Balay, Gropp, McInnes, and Smith, 1997; Balay, Abhyankar, Adams, Benson, Brown, Brune, Buschelman, Constantinescu, Dalcin, Dener, Eijkhout, Gropp, Hapla, Isaac, Jolivet, Karpeev, Kaushik, Knepley, Kong, Kruger, May, McInnes, Mills, Mitchell, Munson, Roman, Rupp, Sanan, Sarich, Smith, Zampini, Zhang, Zhang, and Zhang, 2021; Balay, Abhyankar, Adams, Brown, Brune, Buschelman, Dalcin, Dener, Eijkhout, Gropp, Karpeyev, Kaushik, Knepley, May, McInnes, Mills, Munson, Rupp, Sanan, Smith, Zampini, Zhang, and Zhang, 2019) for the distributed linear algebra. PETSc and many other open-source libraries such as ParMmg (Cirrottola and Froehly, 2021) can be called within FreeFEM. To this end, we use the parallel framework `macro_ddm` which is a high-level FreeFEM macro that one can call in the script at different steps which is needed for the distributed solution of a linear system.

The first step is that of the partition of a global mesh $\mathcal{T}$ into N meshes $\{\mathcal{T}_i\}_{1\leq i\leq N}$ using a partitioner package such as METIS (Karypis and Kumar, 1998) (by default). One can also choose to use Scotch (Pellegrini and Roman, 1996). This step can be performed by using the macro `buildDmesh`. Note that the ghost elements in the overlapping domains are along the skeletons between each subdomain. They are used for multiple MPI processes to communicate one with another. Next, we create the PETSc matrix with `Mat` followed by `createMat` so that one can let FreeFEM interact with PETSc to distribute parallel matrix.

After creating the finite element space and declaring unknowns, we use the corresponding variational formulations to define the bilinear and linear parts with `varf`. The next important step is to build appropriate (or physics-tailored) preconditioners. Various types of multigrid preconditioners have been made available in PETSc library. The mathematical background of the domain decomposition methods and preconditioners can be referred to in (Dolean, Jolivet, and Nataf, 2015). In this chapter, we call GAMG (Adams, Bayraktar, Keaveny, and Papadopoulos, 2004) for solving linear elasticity, cf. Eq. (6.11). See also the scalability analysis in Chapter 2. And we call hypre (Falgout and Yang, 2002) to solve RDE, cf. Eq. (2.36) and helmholtz-type PDEs, cf. Eqs. (6.12) and (6.13). The use of preconditioners ensures that this part of the solver is scalable with respect to the problem size.

For the ease of replication of results as well as to show the user-friendly syntax, we provide in Appendix B.2 a sample code for the implementation of the adjoint equation given in Eq. (6.13).

In this chapter, all the two-dimensional test cases are performed on a laptop equipped with an Intel Xeon processor with a clock frequency of 3.2 GHz having 8 cores and 32 GB of memory.

The three-dimensional test cases are performed on a cloud-based HPC platform–Rescale cluster (www.rescale.com) using 8 or 16 nodes where each node is equipped with 352 GB and an Xeon Platinum 8168 (Skylake) with a clock frequency of 2.7 GHz with 44 cores.

6.3.3 Optimization flow chart

We summarize in Algorithm 5 the workflow of the proposed TO framework. First, the unstrctured mesh $\mathcal{T}$ is created and stored in the Inria Medit format which can be parsed by FreeFEM. Next, the computational domain is decomposed by a standard mesh partitioner such as METIS (Karypis and Kumar, 1998). After that, the initial level-set field is defined[3]. After that, the characteristic function χ_ϕ is initialized based on ϕ. Next, the local averaged characteristic function $\bar{\chi}$ is computed by the PDE-filter.

Then, the optimization loop begins. First, the governing equation is solved. Next, the objective and constraint functionals are computed. If it is converged, the optimization ends. Otherwise, the sensitivity for the local volume constraint $\mathcal{G}'$ is computed as the solution of the adjoint equations given in Eq. (6.8). After that, the sensitivity and the Lagrange multipliers are computed. Then, the level-set function is evolved by solving the RDE, and the newly updated ϕ is bounded in the range of $\phi(\boldsymbol{x}) \in [-1, 1]$. Finally, the characteristic function χ_ϕ and the local averaged value $\bar{\chi}$ are computed successively. The aformentioned workload is repeated until the one of the following criteria are satisfied: (1) the relative difference between the objective and constraint values in current and previous steps is smaller than 10^{-4} for 5 steps in a sequence, or (2) the maximum iteration number is reached (500 in this work).

6.4 Numerical investigation

In this section, we will run Algorithm 5 to solve several toy problems to demonstrate the effectiveness of the proposed methodology. In Section 6.4.1, we consider the optimization of a 3D cantilever. An in-depth numerical investigation is provided to examine the filter parameters and their effects on the optimal solutions. In Section 6.4.2, we will reproduce a "hand" and a "bird beak" example presented in Chapter 2. These two examples will clearly show the capability of our TO framework when handling unstructured mesh and any geometries. Section 6.4.3 shows an extension of this workflow using adaptive mesh refinement. A 2D cantilever test case will be presented to confirm its compatibility to the mesh adaptation techniques.

[3]In this chapter, for all test cases, we initialize the design domain with a uniform level-set field $\phi = 1$, indicating that all the design space is filled with solid phase material. It should be noted that one can only reach a local optima. In other words, the generative design could be highly dependent to the initial guess. However, to examine the effect of the initial guess on the design results is beyond the scope of this chapter, and will thus not be further detailed in the present work.

Algorithm 5 Lattice infill topology optimization.

Input: global mesh $\mathcal{T}$
initialization:
decompose the computational domain for parallel computing
initialize the level-set field ϕ
for $it = 0; it < 500; it = it + 1$ **do**
  solve the governing equations, cf. Eq. (6.11)
  compute the objective value J, cf. Eq. (6.4a)
  compute the global and local volume constraint G_1 and G_2, cf. Eq. (6.4b)
  if $\|J_{it+1} - J_{it}\| < \varepsilon$, $\|G_{it+1} - G_{it}\| < \varepsilon$ **then**
    break
  else
    compute $\mathcal{G}'$ by solving PDE, cf. Eq. (6.13)
    compute the sensitivity $\mathcal{F}'$, cf. Eq. (6.6)
    compute the Lagrange multipliers $\lambda_{1,2}$, cf. Eq. (6.7)
    update the level-set function ϕ by solving RDE, cf. Eq. (2.36)
    update the characteristic function χ_ϕ
    compute the local averaged characteristic function $\bar{\chi}$ by PDE-filter, cf. Eq. (6.12)
  end if
end for

In the present work, all quantities used in the optimization are non-dimensional. We denote by L the unit length. The Young's Modulus E is set to 1.0 and the Poisson's ratio ν is set to 0.3. The fictitious time step Δt is set to 0.1. In all the 3D test cases, four-node linear tetrahedron elements are used to discretize the computational domain. The other parameters used in each test case are documented in Table 6.2.

6.4.1 Cantilever

In this subsection, we start by a classical benchmark–a 3D cantilever as shown in Fig. 6.3. The computational domain is a cuboid with the dimension of "length $\times$ height $\times$ width" = $0.5L \times 0.25L \times 0.25L$. The surface traction $\boldsymbol{g} = [0, 0, -1]^{\mathrm{T}}$ is applied at the left end portion of the bottom surface, and the right end bears a Dirichlet boundary condition ($\boldsymbol{u} = [0, 0, 0]^{\mathrm{T}}$).

First, we examine the effects of r, $V_{\max}$, $\bar{V}_{\max}$ on the optimal solutions, see cases #C.1–C.4. The optimal solutions are shown in Fig. 6.3. The iterative histories of the objective and constraint values of case #C.1 are plotted in Fig. 6.2. The runtime breakdown of the finite element actions performed at each iteration (in average) of cases #C.1 and #C.3 are documented in Table 6.4.

Next, we compute the global volume fractions $V_{\max}$ for each case #C.1–C.4, and impose only the global volume constraint. This is seen cases #C.1G–C.4G, i.e., cases #C.1 and #C.1G have the same value of $V_{\max}$. The objective and global/local volume fraction values for cases #C.1–C.4 and

TABLE 6.2: The filter radius r, regularization parameter τ, global and local maximum allowed volume fraction $V_{\max}$, $\bar{V}_{\max}$, tetrahedron element number n_e, and MPI process number n_p for the test cases.

Case No.	r	τ	$V_{\max}$	$\bar{V}_{\max}$	n_e	n_p	Remesh
Cantilever #C.1, cf. Figs. 6.3a–f	1.0×10^{-2}	1.0×10^{-5}	-	20.0%	$1.04 \cdot 10^7$	352	-
Cantilever #C.2, cf. Figs. 6.3g–l	1.0×10^{-2}	1.0×10^{-5}	-	40.0%	$1.04 \cdot 10^7$	352	-
Cantilever #C.3, cf. Figs. 6.3m–r	5.0×10^{-3}	2.5×10^{-6}	-	20.0%	$2.03 \cdot 10^7$	704	-
Cantilever #C.4, cf. Figs. 6.3s–x	1.0×10^{-2}	1.0×10^{-5}	15.0%	20.0%	$1.04 \cdot 10^7$	352	-
Cantilever #C.1G, cf. Figs. 6.4a–c	-	1.0×10^{-5}	14.0%	-	$1.04 \cdot 10^7$	352	-
Cantilever #C.2G, cf. Figs. 6.4d–f	-	1.0×10^{-5}	31.3%	-	$1.04 \cdot 10^7$	352	-
Cantilever #C.3G, cf. Figs. 6.4g–i	-	2.5×10^{-6}	15.6%	-	$2.03 \cdot 10^7$	704	-
Cantilever #C.4G, cf. Figs. 6.4j–l	-	1.0×10^{-5}	10.1%	-	$1.04 \cdot 10^7$	352	-
Cantilever #C.5A, cf. Figs. 6.9a–b	1.0×10^{-2}	1.0×10^{-5}	-	60.0%	$1.18 \cdot 10^5$	4	Isotropic
Cantilever #C.5F, cf. Figs. 6.9c–d	1.0×10^{-2}	1.0×10^{-5}	-	60.0%	$2.92 \cdot 10^5$	4	-
Hand #H.1, cf. Fig. 6.6a	1.0×10^{-2}	1.0×10^{-5}	-	20.0%	$1.19 \cdot 10^7$	704	-
Hand #H.2, cf. Fig. 6.7	1.0×10^{-2}	1.0×10^{-5}	-	20.0%	$1.19 \cdot 10^7$	704	-
Hand #H.1G, cf. Fig. 6.6b	-	1.0×10^{-5}	10.5%	-	$1.19 \cdot 10^7$	704	-
Beak #B.1, cf. Fig. 6.8	5.0×10^{-3}	2.5×10^{-6}	-	30.0%	$1.75 \cdot 10^7$	704	-

#C.1G–C.4G are summarized in Table 6.3. From these results, some findings can be summarized as follows:

1. Comparing case #C.1 (cf. Figs. 6.3a–f) with #C.2 (cf. Figs. 6.3g–l), it can be observed that with the same value of filter radius r, a larger value of maximum allowed local volume fraction $\bar{V}_{\max}$ tends to suppress the appearance of the lattice infills. Instead, it ends up with a wall-like structure. In contrast, a smaller value of $\bar{V}_{\max}$ results in a truss-like structure. The objective value of case #C.2 is 58.6% higher than that of #C.1, partly due to its higher global volume fraction V_f, partly due to the fact that the enclosed walls can provide higher stiffness than the slender trusses.

2. Comparing case #C.1 (cf. Figs. 6.3a–f) with #C.3 (cf. Figs. 6.3m–r), it can be found that with the same value of $\bar{V}_{\max}$, a smaller value of r can generate a thinner and denser truss-like structure. However, we can observe a decrease of stiffness by 5.7%. Furthermore, our experience tells that a smaller value of r requires finer meshes such that the local mesh resolution can be sufficient to capture the small features such as slender bars. In this chapter, we set r greater than or equal to five times of the mesh size.Also note that a smaller value of r requires a smaller value of the regularization parameter τ. In this chapter, we set $r^2 > 10\tau$.

3. From cases #C.1–C.3 (cf. Figs. 6.3a–r), we find that though only the local volume constraint has been activated, the obtained global volume fraction $V_f < \bar{V}_f$, which means that the global volume constraint is implicitly imposed by the local one. To control the global volume fraction directly, we need to introduce the global volume constraint, see (4).

4. As for case #C.4 (cf. Figs. 6.3s–x), we activate both global and local volume constraints. The design results show that in the global sense, there are large void domains which are attributed to the global volume constraint G_1. On the other hand, in the local sense, truss like structures emerge to satisfy the local volume constraint G_2.

5. From cases #C.1–C.4, it can be clearly observed that no matter if the optimal configuration has truss- or wall-like structure, the structure is dominated by the crossing elongated substructures in the $yz-$plane which follow the principal stress directions.

6. Comparing case #C.1 (cf. Figs. 6.3a–f) with #C.1G (cf. Figs. 6.4a–c), #C.2 with #C.2G, etc., it can be found that with the same global volume fraction, the global volume constraint cases can always outperform their local volume constraint counterparts. It makes physical sense because the geometrical constraints are satisfied at the expense of mechanical performances. On the other hand, if an optimized structure can meet the minimum performance criteria, the sacrifice in performance is not too big an issue since the performance maximization is not the only consideration in many application scenarios as we discussed above. Furthermore, the optimal solutions for the global volume constraint cases #C.1G–C.4G feature thin-walls which are completely filled solid due to the lack of local volume constraint. These optimal

solutions seem to agree well with the previous works on high resolution topology optimization (Liu, Tian, Zong, Ma, Wang, and Zhang, 2019; Sigmund, Aage, and Andreassen, 2016; Wu, Aage, Westermann, and Sigmund, 2017) that thin-wall is the most efficient structure for the minimal mean compliance problem.

7. From the iterative histories shown in Fig. 6.2, we can clearly observe that the compliance gradually increases during the optimization process, along with the decrease in the local volume fraction. The proposed level set-based method uses a binary structure, indicating that there is no grey element appearing during the topological evolution. Hence, one does not bear the risk of misinterpretation of topology.

8. From the runtime breakdown shown in Table 6.4, we can observe that the most time consuming step is to solve the governing equation, i.e., for case #C.3 it takes 59.0% of the total runtime. The overall runtime is approximately 4 h12 min for this large-scale 3D problem having $2.03 \cdot 10^7$ tetrahedral elements.

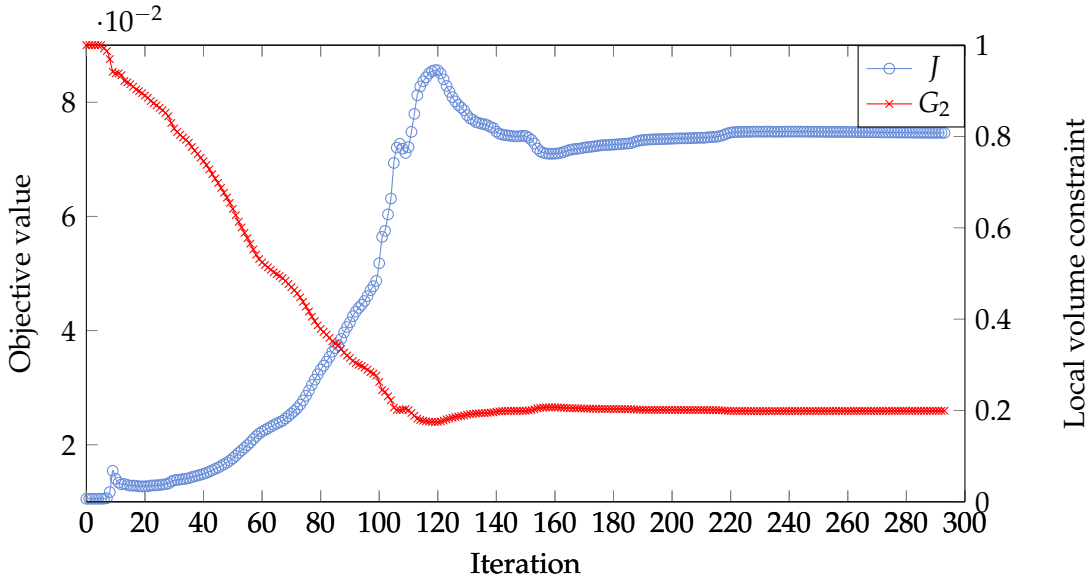

FIGURE 6.2: Iterative histories of the objective and constraint values, cf. Figs. 6.3a–f.

TABLE 6.3: Comparison of the objective and constraint values of the 3D cantilever.

Case No.	J	V_f	$\bar{V}_f$
Cantilever #C.1, cf. Figs. 6.3a–f	$7.46 \cdot 10^{-2}$	14.0%	20.0%
Cantilever #C.2, cf. Figs. 6.3g–l	$3.09 \cdot 10^{-2}$	31.3%	40.0%
Cantilever #C.3, cf. Figs. 6.3m–r	$7.9 \cdot 10^{-2}$	15.6%	20.0%
Cantilever #C.4, cf. Figs. 6.3s–x	$9.32 \cdot 10^{-2}$	10.1%	20.0%
Cantilever #C.1G, cf. Figs. 6.4a–c	$5.3 \cdot 10^{-2}$	14.0%	59.2%
Cantilever #C.2G, cf. Figs. 6.4d–f	$2.42 \cdot 10^{-2}$	31.3%	76.4%
Cantilever #C.3G, cf. Figs. 6.4g–i	$4.81 \cdot 10^{-2}$	15.6%	67.8%
Cantilever #C.4G, cf. Figs. 6.4j–l	$7.49 \cdot 10^{-2}$	10.1%	51.1%

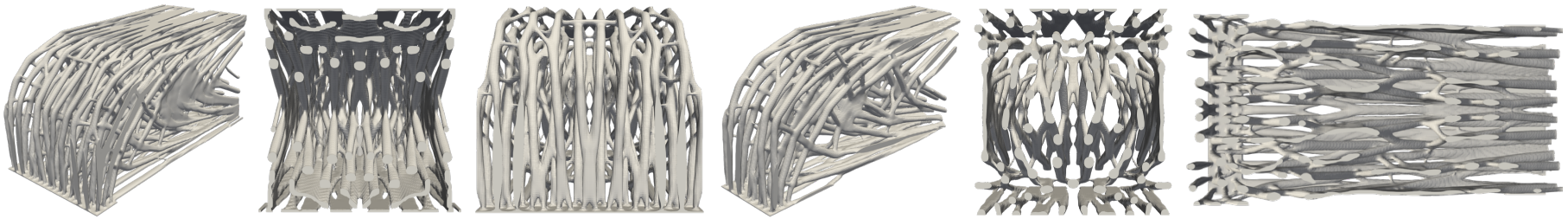

(A) Isometric view. (B) Back view. (C) Front view. (D) Cross section $yz-$plane. (E) Cross section $xy-$plane. (F) Cross section $xz-$plane.

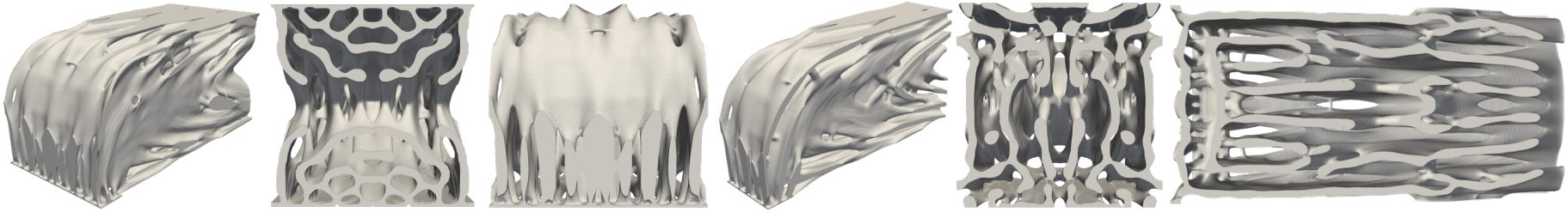

(G) Isometric view. (H) Back view. (I) Front view. (J) Cross section $yz-$plane. (K) Cross section $xy-$plane. (L) Cross section $xz-$plane.

FIGURE 6.3: Design results of the 3D cantilever test case #C.1–#C.4 (from top to bottom).

(M) Isometric view. (N) Back view. (O) Front view. (P) Cross section $yz-$plane. (Q) Cross section $xy-$plane. (R) Cross section $xz-$plane.

(S) Isometric view. (T) Back view. (U) Front view. (V) Cross section $yz-$plane. (W) Cross section $xy-$plane. (X) Cross section $xz-$plane.

FIGURE 6.3: Design results of the 3D cantilever test case #C.1–#C.4 (from top to bottom).

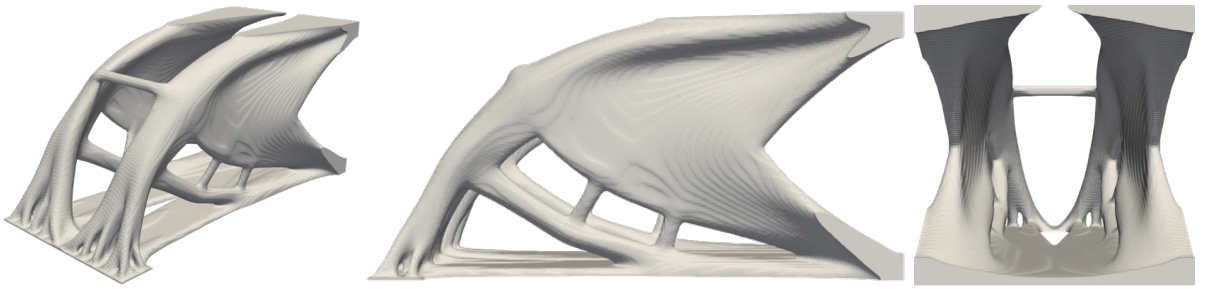

(A) Isometric view. (B) Side view. (C) Back view.

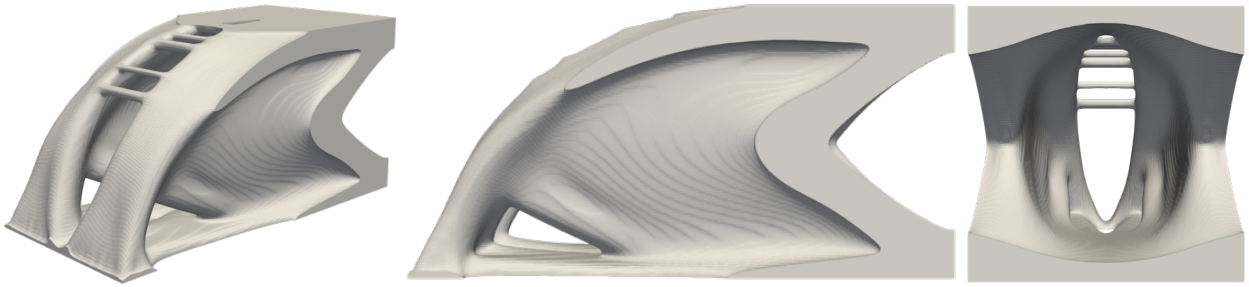

(D) Isometric view. (E) Side view. (F) Back view.

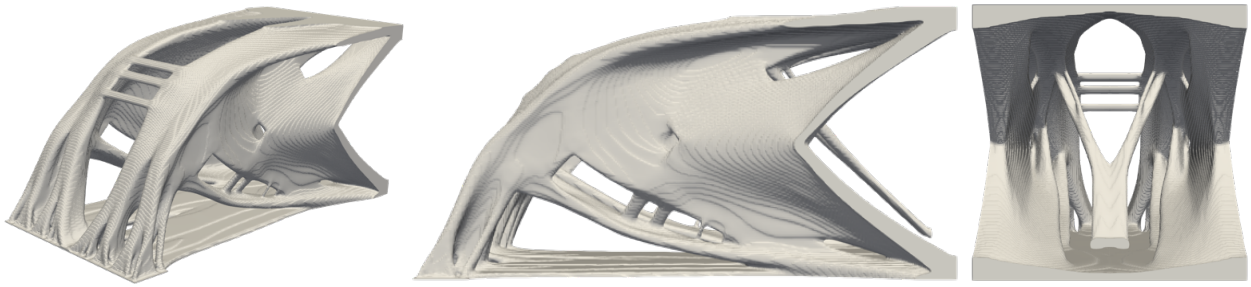

(G) Isometric view. (H) Side view. (I) Back view.

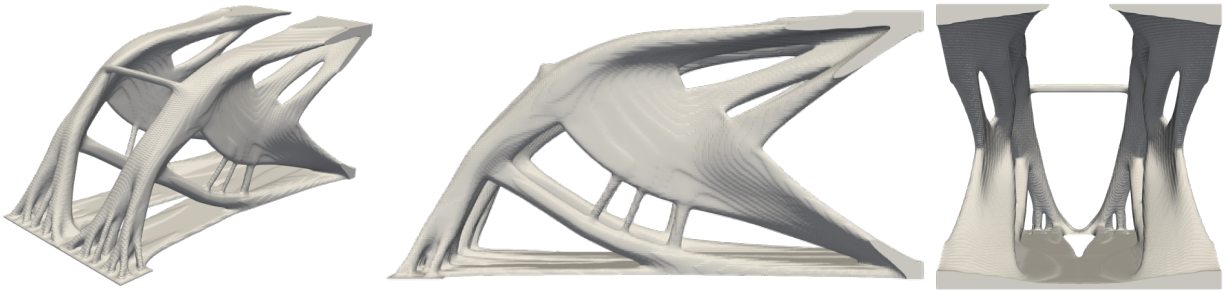

(J) Isometric view. (K) Side view. (L) Back view.

FIGURE 6.4: Design results of the 3D cantilever test case #C.1G–#C.4G (from top to bottom).

TABLE 6.4: Runtime breakdown (s) of the finite element actions performed at each iteration (in average) of the cantilever test cases #C.1 and #C.3.

	Case #C.1	Case #C.3
n_e	$1.04 \cdot 10^7$	$2.03 \cdot 10^7$
n_p	352	704
n_{it}	293	155
Action	Runtime (s)	Runtime (s)
Solve governing equations	19.4	55.0
Compute objective and constraint values	17.4	16.6
Compute $\mathrm{d}G_2/\mathrm{d}\chi$	3.05	2.47
Compute Lagrange multiplier and sensitivity	7.01	9.30
Solve RDE	6.93	6.66
Compute local "averaging" value $\bar{\chi}$	3.04	2.45
Visualization output	0.52	0.52
Total	57.34	93.0

6.4.2 Hand and bird beak

To further demonstrate the capability of the proposed methodology, we now deal with complex-shape structural components and boundary conditions. This can be achieved by using unstructured meshes. To this end, we run the proposed algorithm on another two test cases inspired by the state-of-the-art works (Wu, Dick, and Westermann, 2015; Liu, Hu, Zhu, Matusik, and Sifakis, 2018), and later reproduced in Li, Yamada, Jolivet, Furuta, Kondoh, Izui, and Nishiwaki (2021). Note that in these three works, the global volume constraint was taken into account.

First, we reassemble a "hand" example. The design model is shown in Fig. 6.5. The right end is fixed and the surface traction $\boldsymbol{g} = [0, 0, -1]^{\mathrm{T}}$ is applied on the top of the fingers. The computational domain is discretized into $1.19 \cdot 10^7$ tetrahedral elements, as shown in Fig. 6.5b. In Fig. 6.6, the surface traction is applied on the index, middle, and ring fingers. Figs. 6.6a and b show the optimized results with local and global volume constraint, respectively. Similar to what we have observed in the cantilever test cases, case #H.1 has more slender bars compared with case #H.1G. Then in Fig. 6.7, the surface traction is applied on the top of five fingers. The palm part features bone-like lattice structures whereas the wrist part shows a shell-like structure.

The second example is the infill design of a "bird beak", as shown in Fig. 6.8. The normal force is applied on the outer surface and the left end is fixed. We used approximately $1.75 \cdot 10^7$ tetrahedral elements and performed the distributed computing using 704 MPI processes. Compared to the optimized results shown in our previous works Li, Yamada, Jolivet, Furuta, Kondoh, Izui, and Nishiwaki (2021), the configuration here is much more feature rich due to the use of local volume constraint. We can expect to obtain an ultra-high resolution result if the element number can be increased by at least an order of magnitude.

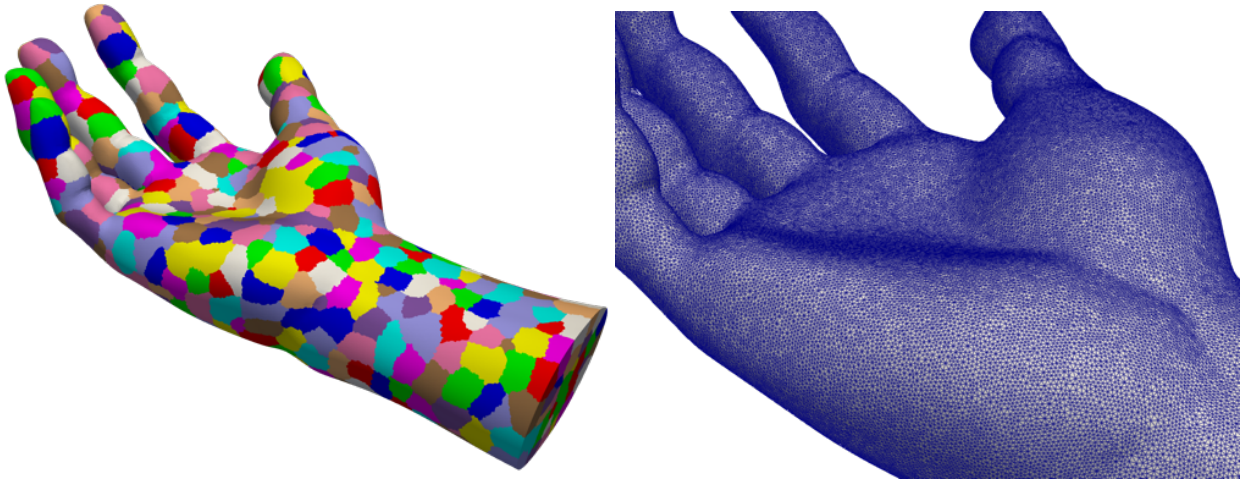

(A) Domain decomposition. (B) Unstructured mesh.

FIGURE 6.5: Hand example: finite element mesh and subdomains for the domain decomposition and parallel computing using 704 MPI processes.

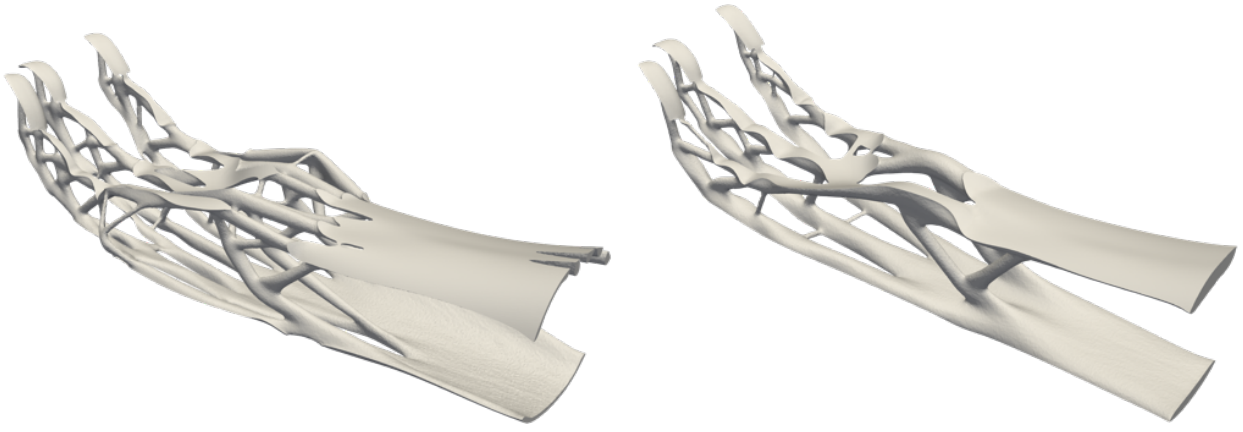

(A) Case #H.1. (B) Case #H.1G.

FIGURE 6.6: Design results of the hand example with (a) local or (b) global volume constraint.

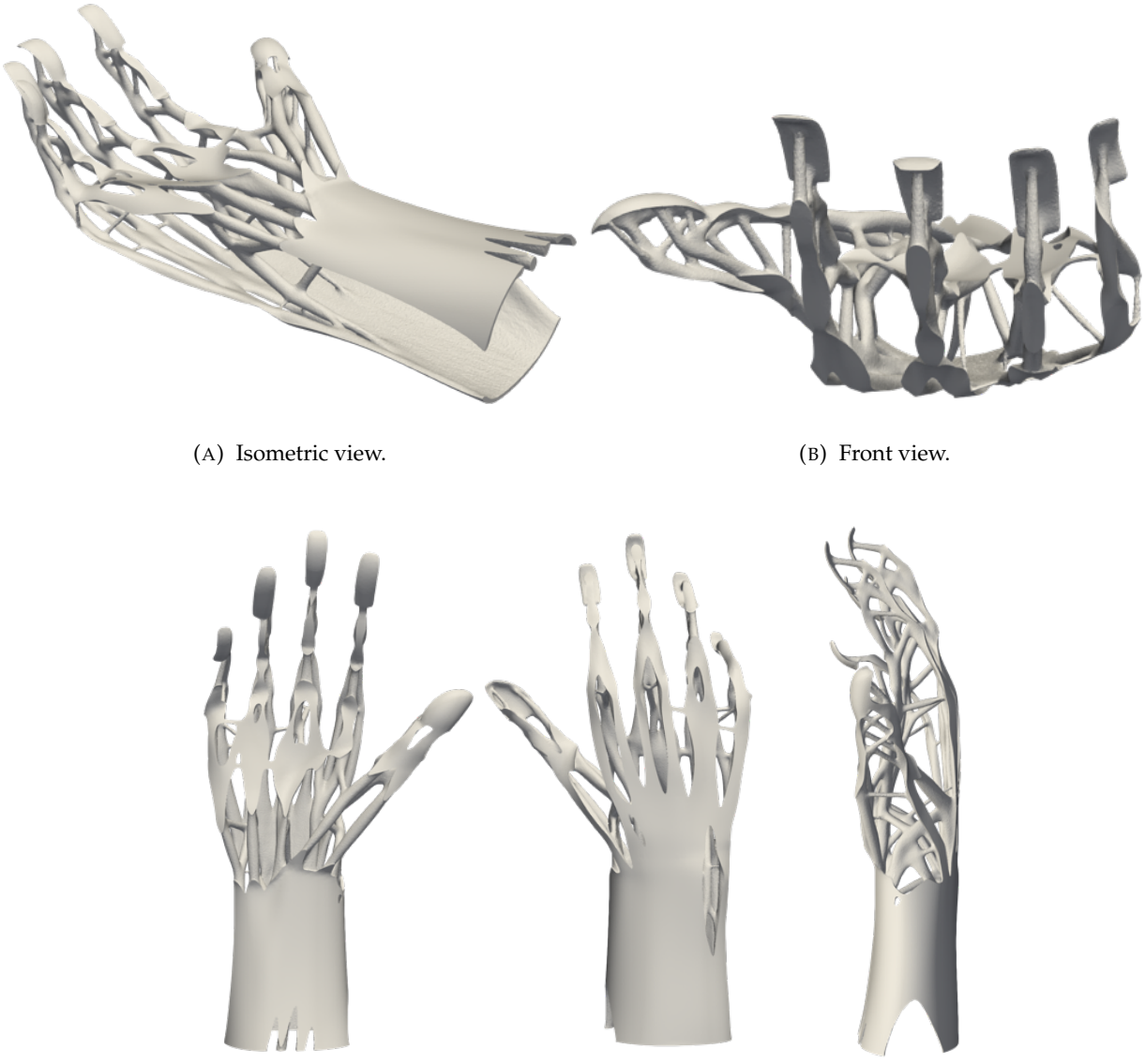

(A) Isometric view.

(B) Front view.

(C) Bottom view.

(D) Top view.

(E) Side view.

FIGURE 6.7: Design results of the hand test case #H.2.

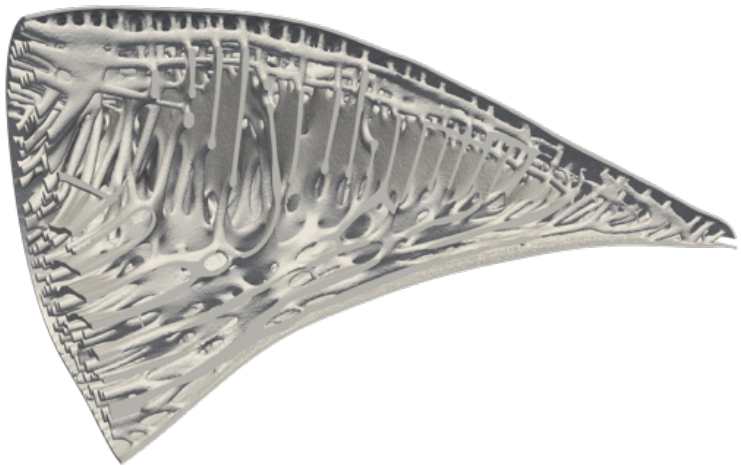

(A) Cross section $yz-$plane.

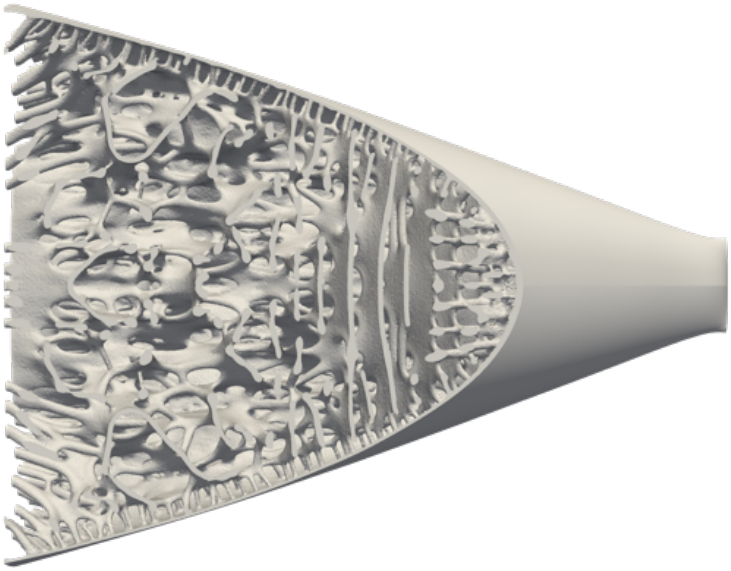

(B) Cross section $xz-$plane.

(C) Back view.

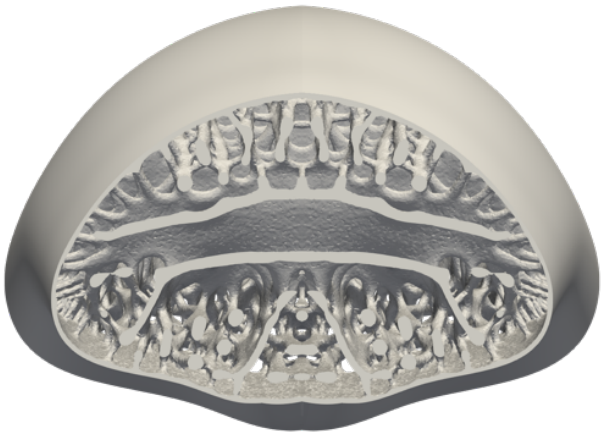

(D) Cross section $xy-$plane.

FIGURE 6.8: Design result of the bird beak test case #B.1.

6.4.3 Extensions

In this subsection, we present some extensions for the proposed framework by introducing an additional ingredient into this workflow–mesh adaptation. As has been briefly discussed above, with the traditional method (Wu, Aage, Westermann, and Sigmund, 2017), it is not easy to incorporate dynamically sparse grids into the optimization solver. On the contrary, in the proposed method, since the PDE-filter is used to compute $\bar{\chi}$, there is no specific restriction on the numerical techniques. For example, numerical analysis using the FEM with other types of elements (i.e., hexahedral elements) or finite volume method (FVM) can be alternative options. In addition, the boundary of the binary structure is represented by the zero-level-set isosurface. Therefore, we can have a clear metric to refine the mesh elements along the boundary. Note that iso-/anisotropic meshes or body-fitted meshes are both compatible to this framework.

The proposed method can adopt three types of adaptive mesh: isotropic (or regular shape), anisotropic, and body-fitted mesh. The isotropic or shape regular adaptive method uses only elements with bounded aspect ratio so that stretched elements can be avoided. Anistropic mesh, on the other hand, can fit high aspect ratio elements along the regions of rapid variation of the solution. And they are preferred to use for situations like boundary layers observed in the fluid mechanics problems (Aguilar and Goodman, 2006). Unlike the above-mentioned two types of meshes, body-fitted mesh adaptation can distribute nodes along the zero-level-set, indicating that we can disjoin-reunion subdomains straightforwardly (Allaire, Dapogny, and Frey, 2013). In this chapter, we demonstrate the mesh adaptivity using the isotropic mesh.

A two-dimensional cantilever case is presented in Fig. 6.9. The computational domain is a rectangle whose dimension is $0.5L \times 0.25L$. The surface traction $\boldsymbol{g} = [0, -1]^{\mathrm{T}}$ is applied at the right end portion of the bottom surface, and the left end bears a Dirichlet boundary condition.

To fully reflect this topic, we also provide a fixed mesh case for comparison. To make this comparison fair enough, as for the adaptive mesh case #C.5A (cf. Fig. 6.9a), we set the minimum mesh size `hmin` to be $1.0 \cdot 10^{-3}$. As for the fixed mesh case #C.5F (cf. Fig. 6.9c), the mesh size is set to $1.0 \cdot 10^{-3}$ in the whole computational domain. The number of triangular elements used at the last iteration is $1.18 \cdot 10^5$ for #C.5A, and $2.92 \cdot 10^5$ for #C.5F. From the results, some findings and suggestions can be concluded as follows:

1. Adaptive and fixed mesh cases end up with a practically identical solution. The relative difference between the obtained objective value is less than 1.2%, as shown in Table 6.5. This observation confirms that the proposed LSM can avoid the mesh dependency to some extent. More importantly, the PDE filter-based local volume constraint method does not have specific restriction on the choice of meshing strategies.

2. It is not always worth performing mesh adaptation since this step is still time consuming, especially for the case where r is very small. It is suggested to estimate the runtime for each

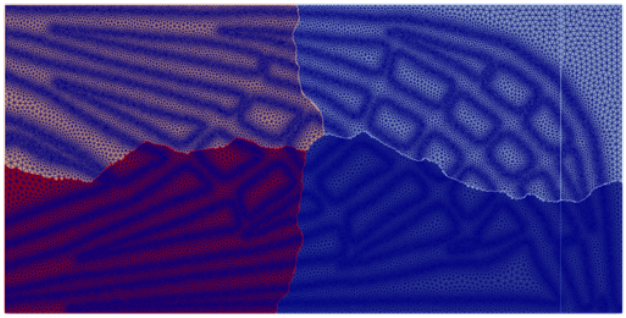

(A) Isotropic adaptive mesh.

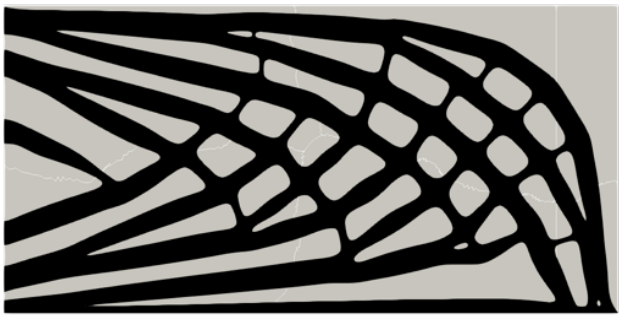

(B) Optimal solution for #C.5A.

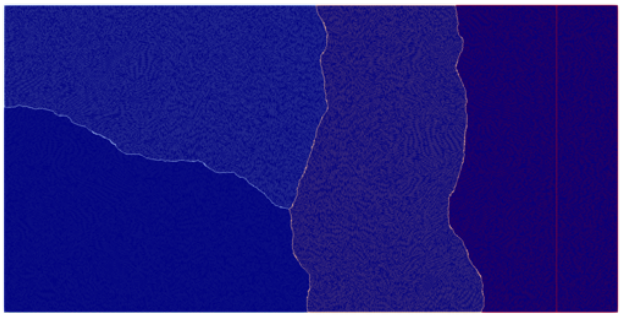

(C) Fixed mesh.

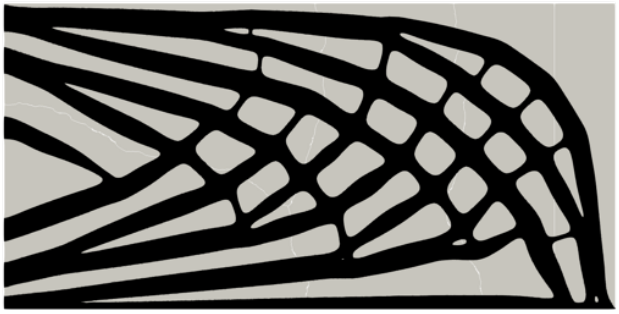

(D) Optimal solution for #C.5F.

FIGURE 6.9: 2D cantilever test cases: finite element mesh and subdomains for the domain decomposition and parallel computing using 4 MPI processes (left column). Optimal solution (right column).

finite element action. If the total runtime of the forward analysis and mesh adaptation is shorter than the forward analysis time using a finer fixed mesh, it may be worthy of remeshing. For example, in the context of thermal fluid TO problems, the governing equations are Navier-Stokes which is a nonlinear system of equations. In that case, the forward analysis could be the bottleneck of the entire solver. The use of adaptive mesh can save the overall runtime. If this is not the case, the fixed meshes may be more efficient.

TABLE 6.5: Comparison of the objective and constraint values of the 2D cantilever.

Case No.	J	V_f	$\bar{V}_f$
Cantilever #C.5A, cf. Figs. 6.9a–b	0.15	47.6%	60.0%
Cantilever #C.5F, cf. Figs. 6.9c–d	0.15	46.4%	60.0%

6.5 Summary

Motivated by the need for porous structure in the design of biodegradable implants, as well as for the diverse and competitive structural designs in the architectures, this chapter proposes a level set-based topology optimization method to design lattice structures. The key idea is to use a variational method (PDE-filter) for the simplification of the numerical evaluation of geometric constraints. It allows us to compute local "averaged" characteristic function on an unstructured mesh by solving this PDE without knowing the spatial information of neighborhood elements.

To demonstrate the complete workflow of the proposed methodology, first, we recalled the mathematical frame of the maximum length scale constraint and how it was integrated into the reaction–diffusion equation-based level-set method. Secondly, the optimum design problem was formulated and the sensitivity derived using the continuous adjoint method. Thirdly, the implementation details were illustrated regarding the finite element modeling and distributed computing, together with the sample codes to show its user-friendly syntax. Finally, we ran our algorithm to solve various large-scale three-dimensional test cases. The main findings can be summarized as follows:

1. With different values of the maximum allowed local volume fraction and filtered radius, one can end up with truss-like (resp. wall-like) structures featuring slender and denser (resp. thicker and sparser) trusses.
2. The RDE-based level-set method allows us to design from scratch. Moreover, the binary structure ensures that one does not bear the risk of misinterpretation of topological configuration throughout the iterative history.
3. There is no specific restriction on the numerical techniques. Using the unstructured mesh, the proposed framework can easily deal with complex-shape structural components. Furthermore, mesh adaptation techniques can be integrated into this workflow.
4. Large-scale 3D problems, having approximately 20 million tetrahedral elements, are computed with 704 MPI processes. It requires a fully-distributed framework including scalable domain decomposition, matrix assembly, parallel interpolation, and linear solver that very few general purpose libraries offer. This is achieved by using multigrid preconditioners offered by PETSc, suitably interfaced in FreeFEM.

As a final remark, the proposed PDE filter-based maximum length scale constraints can be adopted by any other level set-based shape and topology optimization methods. But it should be noted that the averaged value computed by this PDE-filter is weighted by the distance, which means that it is not as precise as the the one evaluated by the average of neighboring elements (Wu, Clausen, and Sigmund, 2017). In addition, a validated computational model of the degradation process (Barzegari, Mei, Lamaka, and Geris, 2021) paves the way to future investigations into

the biodegradation behavior of those optimized lattice structures. Finally, this chapter can be a helpful discussion for such further research, aimed at including maximum length scale constraint in large-scale multiphysics TO such as thermal-fluids, multi-material designs, etc.

Chapter 7

General Conclusions

This thesis focuses on the level set-based topology optimization for the optimum design of thermal fluid–structure systems. The following is a summary of achievements.

In Chapter 2, the basic concept of the level-set method is introduced. The mathematical and physical frame of the reaction–diffusion equation (RDE) based topology optimization (TO) method is provided and the derivation of the topological derivative is given in details. Building upon this cornerstone, we propose a parallel distributed and open-source framework for full-scale three-dimensional structural topology optimization. This can be achieved by properly combining parallel computing and mesh adaption techniques by adopting a RDE-based level-set method (LSM). Mesh adaptivity which discretizes and optimizes an implicitly defined surface (level-set interface) can allow us to reach an optimal solution with high-resolution and clear boundaries. Our framework can be easily extended to design real world engineering products which have complex geometries, and optimized structures represented by body-fitted tetrahedral meshes can be efficiently post-processed and prototypes can be built straightforwardly. Furthermore, the proposed optimization algorithm can mitigate dependency to initial guess and mesh resolution to some extent. Our numerical implementation uses FreeFEM for finite element analysis (FEA), PETSc for distributed linear algebra, and Mmg for mesh adaption. Several numerical examples for the minimal mean compliance problem support these remarkable features. However, it should be pointed out that the main limitations of the present framework is that the mesh adaptation step is done in sequential, meaning that a global mesh has to be centralized. This can be quite memory demanding. Indeed, the framework in its current form (integrated with the sequential version of Mmg) is still not scalable to billions of voxels, but is targeted in our future work.

In Chapter 3, we extend the proposed TO framework to solve the two- and three-dimensional weakly-coupled fluid–structure problems. From the numerical point of view, two key ingredients are highlighted: (i) the body-fitted adaptive mesh strategy allows the disjoint-reunion of a global mesh that contains several (fluid/solid) subdomains, whose interfaces can be described by an implicitly defined surface (zero level-set); (ii) physics tailored multigrid preconditioner techniques are utilized to solve the large-scale finite element systems. More specifically, a modified

augmented Lagrangian (mAL) preconditioner is adopted to solve the linearized flow equations. From the engineering stand point, we propose a complete product development workflow including the pre-processing, TO, B-Rep conversion, and the numerical experiment. The performance of our methodology is demonstrated by solving three different optimization problems: minimal mean compliance problem, minimal power dissipation problem, and fluid–structure interaction (including both "dry" and "wet" FSI). For comparison and for assessing our various techniques, we benchmark our designs against state-of-the-art works. The main findings real that: (1) the suggested TO method allows the nucleation of new holes during the topology evolution. By combining the body-fitted remeshing technique, we are able to solve the "wet" (design-dependent) FSI problem with no predefined holes in the initial guess; (2) several engineering cases (e.g., roof support design, pipe connector design, solar plate support design) are presented to highlight the potential of the proposed design workflow to real-world applications. (3) The B-Rep conversion allows the organic part (design domain) to be integrated into (resp. extracted from) the assembly. The converted CAD data features an editable and smoothened boundary. This allows the generation of a high quality boundary layer mesh for the CFD simulation and helps ease the manufacturing.

In Chapter 4, we shed a light on the passive heat sinks cooled by natural convection which are known to be reliable, compact, and low-noise. They are widely used in telecommunication devices, LEDs, etc. This chapter builds upon the recent advancements in fluid topology optimization to present a case study of two- and three-dimensional optimum design and thermal modeling for natural convection problems using the proposed design methodology. To this end, first, a high-fidelity thermal–fluid model is constructed where the full Navier–Stokes equations are strongly coupled with the energy equation through the Boussinesq approximation. We benchmark our simulation solver against experimental analysis and other numerical analysis methods such as the ISHP method and the FVM. Next, we carefully investigate the flow behavior under different Grashof numbers using a fully transient simulation solver. Then we run our algorithm to deliver interesting 2D and 3D generative designs. The main findings reveal that: (1) the nonlinear RAMP scheme is employed for material interpolation to prevent bad quality local optima. The binary structure expression allows us to avoid the use of the continuation approach to penalize the design variable to the binary structure. The penalty parameters can be used to control the geometrical complexity of the optimal configuration. (2) The generative designs represented by the body-fitted meshes are converted into editable CAD models, and they are imported to the COMSOL simulation solver for performance validation. The simulation results agree well with the optimization solver, confirming the accuracy of the hybrid modeling strategy. The crosscheck results show that the design optimized for a certain Grashof number preferably performs better than the others for its particular Grashof number. Moreover, the TO designs perform better than the reference design, which further validates the effectiveness of the suggested design methodology. (3) A moderately large-scale TO problem with $3.56 \cdot 10^6$ unknowns can be solved in parallel on a standard multiprocessor system, thanks to the use of sparsely populated grids.

In Chapter 5, we focus on an important technical issue encountered in the large-scale fluid relevant TO. That is to improve the computational efficiency and to save the overall computational cost. To this end, we incorporate three different remeshing techniques (isotropic, anisotropic, or body-fitted adaptive mesh refinement) into the proposed TO framework. This is owing to the flexibility of the RDE method for handling both "separate" and "hybrid" flow modeling strategies. The "separate" modeling, relying on the body-fitted mesh, allows the disjoint-reunion of a global mesh that contains several (fluid/solid) subdomains. The no-slip boundary conditions can be applied on the moving fluid-solid interface. The "hybrid" modeling, on the other hand, relying on the idea of the fictitious porous media, is compatible with iso-/anisotropic mesh. Moreover, the iso-/anisotropic remeshing algorithms can be performed in parallel. This breaks through the existing bottleneck of the sequentially performed body-fitted mesh evolution method. A lift–drag optimization problem, a classical minimal power dissipation problem, and a forced convection problem are formulated. Various 2D/3D, small-/large-scale test cases are presented to validate the computational efficiency of this framework. The results show that with the "hybrid" modeling, over 70% runtime-saving is reported compared with the "separate" modeling. This is partly due to the fact that the iso-/anisotropic mesh adaptation can be performed in a distributed fashion, partly due to a huge decrease in the Newton iteration number. In addition, a large-scale 3D test case (using fixed mesh) with a total tetrahedra number of $3.12 \cdot 10^6$, having approximately $1.32 \cdot 10^7$ degrees of freedom for the linearized fluid system, is solved using a cluster mounted with 352 MPI processes, further confirming the scalability of the proposed framework.

In Chapter 6, we focus on the biomimetic design of porous structures observed in natural systems. The basic idea is to impose a maximum allowable volume fraction to the locally averaged value of the characteristic function. To compute this local averaged value, a PDE-filter is introduced. Unlike the traditional approach which requires the measurement of the percentage of solid voxels overall voxels in a prescribed neighborhood, the proposed method shows the following good features: (1) it can be used in the unstructured mesh and/or adaptive mesh-based TO framework. There is no specific restriction on the numerical techniques. (2) The use of this PDE-filter makes the distributed computing quite straightforward. (3) This geometrical constraint can be applied to any physics governed by different constitutive laws. To formulate the optimization model, we use the $p-$norm function to approximate the maximum value of the local averaged value thus makes it differentiable. Various large-scale three-dimensional test cases are presented. We push the tetrahedral element number to the level of 20 million and perform the computation on cloud-based clusters. The design results reveal that: (1) a larger value of maximum allowed local volume fraction tends to suppress the appearance of the lattice infills. Instead, it ends up with a wall-like structure. (2) A smaller value of PDE-filter radius can generate thinner and denser truss-like structure. (3) No matter the optimal configuration has truss- or wall-like structure, the structure is dominated by the crossing elongated sub-structures which follow the principal stress directions. (4) With the same global volume fraction, the global volume constraint cases can always outperform their local volume constraint counterparts. It makes physical sense since we have to sacrifice the ultimate in performance for the sake of geometrical requirement. (5)

Adaptive and fixed mesh cases end up with a practically identical solution. This confirms that the PDE filter-based local volume constraint method does not have specific restriction on the choice of meshing strategies.

To conclude, this thesis develops a reaction–diffusion equation-based level-set method to solve multi-physics topology optimization problems. We highlight two key ingredients in this workflow. The first is the *physics-dependent multigrid preconditioner* for distributed computing. This ensures that the physical computation part of the TO framework can be highly scalable with respect to the problem size. The second is the *adaptive mesh refinement*. This further exploits the potential of LSM, stating that, at each iterative step, the global mesh needs to be reconstructed and tetrahedra are only refined in the region-of-interest while remaining coarse at the far field, making it possible to reduce the overall computational cost. We present a variety of conceptual designs for not only academic toy problems but also practical application cases. We hope that this thesis can provide some guiding significance to the generative design of fluidic devices that can be used in the real-world industry.

Appendix A

Sensitivity Analysis

A.1 Minimal mean compliance problem

Using Lagrange's method, the optimization problem given by Section 2.2.4 is replaced with an unconstrained optimization problem.The Lagrangian $\mathscr{L}(\tilde{u}, \tilde{v}, \lambda_1, \Omega)$ is formulated as:

$$\mathscr{L}(\tilde{u}, \tilde{v}, \lambda_1, \Omega) = \int_{\Gamma_N} g \cdot \tilde{u}\, d\Gamma - \int_{\Omega} (\mathrm{div}(C : e(\tilde{u}))) \cdot \tilde{v}\, d\Omega \quad + \lambda_1 \left(\frac{\int_D \chi_\phi d\Omega}{\int_D d\Omega} - V_{\max} \right), \tag{A.1}$$

where $\tilde{u}$ and $\tilde{v}$ are vector-valued functions, $\tilde{v}$ is the adjoint variable for the governing equation, and λ_1 is the Lagrange multiplier for the volume constraint. First, in order to derive the adjoint equations, we use the Lagrangian $\mathscr{L}(\tilde{u}, \tilde{v}, \Omega)$ which does not include the volume constraint G_1, as follows:

$$\mathscr{L}(\tilde{u}, \tilde{v}, \Omega) = \int_{\Gamma_N} g \cdot \tilde{u}\, d\Gamma - \int_{\Omega} (\mathrm{div}(C : e(\tilde{u}))) \cdot \tilde{v}\, d\Omega. \tag{A.2}$$

For the second term on the right-hand side in Eq. (A.2), by applying integration by parts and the divergence theorem, Eq. (A.2) can be rewritten as follows:

$$\mathscr{L}(\tilde{u}, \tilde{v}, \Omega) = \int_{\Gamma_N} g \cdot \tilde{u}\, d\Gamma + \int_{\Omega} (e(\tilde{u}) : C) : e(\tilde{v})\, d\Omega \quad - \int_{\Gamma_N} g \cdot \tilde{v}\, d\Gamma. \tag{A.3}$$

Using the definition of Gâteaux derivative, the partial derivative of the Lagrangian $\mathscr{L}(\tilde{u}, \tilde{v}, \Omega)$ with respect to $\tilde{u}$ in the direction ξ at the stationary point (u, v) will be:

$$\left\langle \frac{\partial \mathscr{L}}{\partial \tilde{u}}(u, v, \Omega), \xi \right\rangle = \int_{\Gamma_N} g \cdot \xi d\Gamma \quad + \int_{\Omega} (e(\xi) : C) : e(\tilde{v})\, d\Omega = 0. \tag{A.4}$$

For the second term on the right-hand side in Eq. (A.4), ξ can be switched with $\tilde{v}$ thanks to the symmetric property of the bilinear form. Thus, Eq. (A.4) can be rewritten as:

$$\left\langle \frac{\partial \mathscr{L}}{\partial \tilde{u}}(u, v, \Omega), \xi \right\rangle = \int_{\Gamma_N} g \cdot \xi d\Gamma \quad + \int_{\Omega} (e(\tilde{v}) : C) : e(\xi)\, d\Omega = 0. \tag{A.5}$$

For the second term on the right-hand side of Eq. (A.5), by applying integration by parts and the divergence theorem, the following equation is obtained:

$$\begin{aligned}\left\langle \frac{\partial \mathscr{L}}{\partial \tilde{u}}(u,v,\Omega),\xi \right\rangle = &-\int_{\Omega} \operatorname{div}(C:e(\tilde{v}))\cdot\xi dx + \int_{\Gamma_D}((C:e(\tilde{v})))\cdot n)\cdot\xi d\Gamma \\ &+\int_{\Gamma_N}((C:e(\tilde{v}))\cdot n)+g)\cdot\xi d\Gamma = 0.\end{aligned} \tag{A.6}$$

The above equation should be satisfied with any arbitrary ξ. Therefore, the adjoint equation can be obtained as follows:

$$\begin{cases} \operatorname{div}(C:e(v)) = 0 & \text{in } \Omega \\ v = 0 & \text{on } \Gamma_{\mathrm{D}} \\ -\tilde{g} = \bar{g} & \text{on } \Gamma_{\mathrm{N}}, \end{cases} \tag{A.7}$$

where $\tilde{g} = (C:e(v))\cdot n$. Comparing adjoint equation Eq. (A.7) with the governing equation Eq. (2.1), it can be seen that the adjoint problem is self-adjoint with $v = -u$.

Next, to derive the topological derivative, a boundary value problem considering a created hole is formulated as:

$$\begin{cases} -\operatorname{div}(C:(e(u)+e(\delta u)) = 0 & \text{in } \Omega\backslash\Omega_\epsilon \\ u+\delta u = 0 & \text{on } \Gamma_{\mathrm{D}} \\ g+\delta g = \bar{g} & \text{on } \Gamma_{\mathrm{N}} \\ g+\delta g = 0 & \text{on } \Gamma_\epsilon. \end{cases} \tag{A.8}$$

The Lagrangian considering a created hole is given as:

$$\begin{aligned}\bar{F}+\delta\bar{F} = &\int_{\Omega\backslash\Omega_\epsilon} e(v):C:e(u+\delta u)d\Omega + \int_{\Gamma_{\mathrm{N}}}(u+\delta u)\cdot(g+\delta g)\,d\Gamma \\ &-\int_{\Gamma_{\mathrm{N}}}(g+\delta g)\cdot v d\Gamma - \int_{\Gamma_\epsilon}(g+\delta g)\cdot v d\Gamma + \lambda_1\left(\frac{\int_{\Omega\backslash\Omega_\epsilon}\chi_\phi d\Omega}{\int_{\Omega\backslash\Omega_\epsilon} d\Omega} - V_{\max}\right).\end{aligned} \tag{A.9}$$

Substituting the boundary condition $g+\delta g = 0$ on Γ_ϵ into Lagrangian Eq. (A.9), then subtracting the Lagrangian Eq. (A.1) from Lagrangian Eq. (A.9), the variation $\delta\bar{F}$ of the Lagrangian is given as:

$$\begin{aligned}\delta\bar{F} = &\int_{\Omega\backslash\Omega_\epsilon} e(v):C:e(\delta u)d\Omega - \int_{\Omega_\epsilon} e(v):C:e(u)d\Omega + \int_{\Gamma_{\mathrm{N}}}(g\cdot\delta u+\delta g\cdot u)\,d\Gamma \\ &-\int_{\Gamma_{\mathrm{N}}}\delta g\cdot v d\Gamma - \lambda_1\left(\frac{\int_{\Omega_\epsilon}\chi_\phi d\Omega}{\int_{\Omega_\epsilon} d\Omega}\right).\end{aligned} \tag{A.10}$$

Applying Green's formula to the first term in Eq. (A.10), and substituting the boundary conditions, $\delta u = 0$ on Γ_D and $\delta g = 0$ on Γ_N, the variation can be rewritten as:

$$\begin{aligned}\delta\bar{F} = &-\int_{\Omega\backslash\Omega_\epsilon} \operatorname{div}\left(C : e(v)\right)\cdot\delta u d\Omega - \int_{\Omega_\epsilon} e(v) : C : e(\delta u) d\Omega + \int_{\Gamma_\epsilon} \left(C : e(v)\right)\cdot\delta u \cdot n d\Gamma \\ &+ \int_{\Gamma_N} (\tilde{g}+g)\cdot\delta u d\Gamma - \lambda_1 \left(\frac{\int_{\Omega_\epsilon}\chi_\phi d\Omega}{\int_{\Omega_\epsilon} d\Omega}\right).\end{aligned} \tag{A.11}$$

Using the adjoint variable $v = -u$ obtained by solving the adjoint equation Eq. (A.7), the variation of Lagrangian can be rewritten as:

$$\delta\bar{F} = \int_{\Omega_\epsilon} e(u) : C : e(\delta u) d\Omega - \int_{\Gamma_\epsilon} \left(C : e(u)\right)\cdot\delta u \cdot n d\Gamma - \lambda_1 \left(\frac{\int_{\Omega_\epsilon}\chi_\phi d\Omega}{\int_{\Omega_\epsilon} d\Omega}\right). \tag{A.12}$$

To calculate the unknown δu in Eq. (A.12), we subtract Eq. (2.4) from Eq. (A.8), and obtain the following problem:

$$\begin{cases} -\operatorname{div}(C : e(\delta u)) = 0 & \text{in } \Omega\backslash\Omega_\epsilon \\ \delta u = 0 & \text{on } \Gamma_{\mathrm{D}} \\ \delta g = 0 & \text{on } \Gamma_{\mathrm{N}} \\ \delta g = -g^0 & \text{on } \Gamma_\epsilon, \end{cases} \tag{A.13}$$

where the tensor $g^0 = \sigma^0(u)\cdot n = C : e^0(u)$. Note that the superscript 0 indicates the values without creating a hole. The solution of the boundary value problem in Eq. (A.13) is given by Guzina and Bonnet (2004), as follows:

$$\delta u_i = -\frac{\epsilon}{\mu}\left(\frac{4-5\mu}{7-5\mu}\sigma^0_{ij}(u)n_j - \frac{3-5\mu}{4(7-5\mu)}\sigma^0_{jj}(u)n_j + O(\varepsilon)\right). \tag{A.14}$$

Therefore, the variation of Lagrangian $\bar{F}$ is obtained as:

$$\begin{aligned}&\delta\bar{F} = \\ &\frac{4\pi\epsilon^3}{3}\left\{\frac{3(1-\nu)}{2(1+\nu)(7-5\nu)}\left[\frac{-\left(1-14\nu+15\nu^2\right)E(\chi_\phi)}{(1-2\nu)^2}\delta_{ij}\delta_{kl} + 5E(\chi_\phi)\left(\delta_{ik}\delta_{jl}+\delta_{il}\delta_{jk}\right)\right] e^0_{ij}(u)e^0_{kl}(u) - \lambda_1\right\},\end{aligned} \tag{A.15}$$

where δ_{ij} is the Kronecker delta function. Hence, the topological derivative $d_t\bar{F}$ is derived as follows:

$$d_t\bar{F} = \lim_{\epsilon\to 0}\frac{\delta\bar{F}}{\frac{4\pi\epsilon^3}{3}} = \left(e(u) : A\right) : e(u) - \lambda_1, \tag{A.16}$$

where the fourth-order tensor A is defined as follows:

$$A_{ijkl} := A_1\delta_{ij}\delta_{kl} + A_2\left(\delta_{ik}\delta_{jl} + \delta_{il}\delta_{jk}\right), \tag{A.17}$$

where A_1 and A_2 are given as:

$$\begin{cases} A_1 = -\dfrac{3(1-\nu)\left(1-14\nu+15\nu^2\right)}{2(1+\nu)(7-5\nu)(1-2\nu)^2}E(\chi_\phi) \\ A_2 = \dfrac{15(1-\nu)}{2(1+\nu)(7-5\nu)}E(\chi_\phi). \end{cases} \tag{A.18}$$

A.2 Natural convection problem

Using Lagrange's method, the optimization problem given by Eq. (4.12) can be replaced with an unconstrained optimization problem. The Lagrangian $\mathscr{L}\left(\boldsymbol{v}, \boldsymbol{v}_A, p, p_A, T, T_A, \lambda_1, \Omega\right)$ is formulated as:

$$\begin{aligned} &\mathscr{L}\left(\boldsymbol{v}, \boldsymbol{v}_A, p, p_A, T, T_A, \lambda_1, \Omega\right) \\ &= \underbrace{\int_\omega QT d\Omega}_{\text{obj. function}} + \int_\Omega \boldsymbol{v}_A \cdot \underbrace{\left(\left(\boldsymbol{v}\cdot\nabla\right)\boldsymbol{v} - \mathrm{Pr}\,\nabla\cdot\left(\nabla\boldsymbol{v}+\nabla\boldsymbol{v}^{\mathrm{T}}\right)+\nabla p+\alpha\boldsymbol{v}-\mathrm{Gr}\,\mathrm{Pr}^2\,T\boldsymbol{e}_3\right)}_{\text{momentum conservation}} d\Omega \\ &- \int_\Omega p_A \underbrace{\left(\nabla\cdot\boldsymbol{v}\right)}_{\text{continuity}} d\Omega + \int_\Omega T_A \underbrace{\left(\left(\boldsymbol{v}\cdot\nabla T\right)-\nabla\cdot\left(\kappa\nabla T\right)-Q\right)}_{\text{energy conservation}} d\Omega + \lambda_1 \underbrace{\left(\frac{\int_D 1-\chi_\phi d\Omega}{\int_D d\Omega} - V_{\max}\right)}_{\text{volume constraint}} \end{aligned} \tag{A.19}$$

Using the definition of Gâteaux derivative, the partial derivative of the Lagrangian $\mathscr{L}\left(\boldsymbol{v}, \boldsymbol{v}_A, p, p_A, T, T_A, \lambda_1, \Omega\right)$ with respect to $\boldsymbol{v}$, p, and T in the direction ξ at the stationary point will be:

$$\begin{aligned} &\left\langle \frac{\partial\mathscr{L}}{\partial\boldsymbol{v}}\left(\boldsymbol{v}, \boldsymbol{v}_A, p, p_A, T, T_A, \lambda_1, \Omega\right), \boldsymbol{\xi}\right\rangle \\ &= \int_\Omega -\boldsymbol{\xi}\cdot\left(\boldsymbol{v}\cdot\nabla\boldsymbol{v}_A\right) + \boldsymbol{\xi}\cdot\left(\boldsymbol{v}_A\cdot\nabla\boldsymbol{v}^{\mathrm{T}}\right) - \boldsymbol{\xi}\cdot\left(\mathrm{Pr}\,\nabla\cdot\left(\nabla\boldsymbol{v}_A+\nabla\boldsymbol{v}_A^{\mathrm{T}}\right)\right) \\ &+ \boldsymbol{\xi}\cdot\alpha\boldsymbol{v}_A + \boldsymbol{\xi}\cdot\nabla p_A + T_A\left(\boldsymbol{\xi}\cdot\nabla T\right) d\Omega \\ &+ \int_\Gamma \left(\boldsymbol{v}_A\cdot\boldsymbol{\xi}\right)\left(\boldsymbol{v}\cdot\boldsymbol{n}\right) + \left(\boldsymbol{\xi}\cdot\mathrm{Pr}\left(\nabla\boldsymbol{v}_A+\nabla\boldsymbol{v}_A^{\mathrm{T}}\right)\right)\cdot\boldsymbol{n} \\ &- \left(\boldsymbol{v}_A\cdot\mathrm{Pr}\left(\nabla\boldsymbol{\xi}+\nabla\boldsymbol{\xi}^{\mathrm{T}}\right)\right)\cdot\boldsymbol{n} - \left(p_A\boldsymbol{\xi}\right)\cdot\boldsymbol{n} d\Gamma = 0. \end{aligned} \tag{A.20}$$

$$\begin{aligned} &\left\langle \frac{\partial\mathscr{L}}{\partial p}\left(\boldsymbol{v}, \boldsymbol{v}_A, p, p_A, T, T_A, \lambda_1, \Omega\right), \xi\right\rangle \\ &= -\int_\Omega \nabla\cdot\boldsymbol{v}_A\xi d\Omega + \int_\Gamma \left(\boldsymbol{v}_A\xi\right)\cdot\boldsymbol{n} d\Gamma = 0 \end{aligned} \tag{A.21}$$

$$\begin{aligned}
&\left\langle \frac{\partial \mathscr{L}}{\partial T}\left(\boldsymbol{v}, \boldsymbol{v}_A, p, p_A, T, T_A, \lambda_1, \Omega\right), \xi \right\rangle \\
&= \int_\omega Q\xi d\Omega - \int_\Omega \boldsymbol{v}_A \cdot \left(\mathrm{Gr}\,\mathrm{Pr}^2\,\xi \boldsymbol{e}_3\right) - \left(\nabla T_A \cdot \boldsymbol{v}\right)\xi - \nabla \cdot \left(\kappa \nabla T_A\right)\xi d\Omega \\
&+ \int_\Gamma \left(T_A \boldsymbol{v}\xi + \kappa \nabla T_A \xi - \kappa T_A \nabla \xi\right) \cdot \boldsymbol{n} d\Gamma = 0
\end{aligned} \tag{A.22}$$

The above system of equations should be satisfied with any arbitrary ξ. Therefore, the adjoint equation can be obtained as follows:

$$\begin{cases}
-\boldsymbol{v} \cdot \nabla \boldsymbol{v}_A + \boldsymbol{v}_A \cdot \nabla \boldsymbol{v}^{\mathrm{T}} - \mathrm{Pr}\,\nabla \cdot \left(\nabla \boldsymbol{v}_A + \nabla \boldsymbol{v}_A^{\mathrm{T}}\right) + \alpha \boldsymbol{v}_A + \nabla p_A + T_A \nabla T = 0 \\
-\nabla \cdot \boldsymbol{v}_A = 0 \\
Q - \mathrm{Gr}\,\mathrm{Pr}^2\,\boldsymbol{v}_A \cdot \boldsymbol{e}_3 - \nabla T_A \cdot \boldsymbol{v} - \nabla \cdot \left(\kappa \nabla T_A\right) = 0,
\end{cases} \tag{A.23}$$

with the following adjoint boundary conditions:

$$\begin{cases}
\boldsymbol{v}_A = 0 & \text{on } \partial\Omega \\
T_A = 0 & \text{on } \Gamma \\
\left(T_A \boldsymbol{v} + \kappa \nabla T_A\right) \cdot \boldsymbol{n} = 0 & \text{on } \partial\Omega \backslash \Gamma.
\end{cases} \tag{A.24}$$

Finally, following the RAMP material interpolation scheme defined in Eq. (4.11), the design sensitivity can be easily derived as follows:

$$\frac{d\mathscr{L}}{d\chi_\phi} = \int_\Omega -\frac{q_\alpha \alpha_{\max}\left(q_\alpha + 1\right)}{\left(q_\alpha + \chi_\phi\right)^2} \boldsymbol{v} \cdot \boldsymbol{v}_A - \nabla T_A \cdot \nabla T \frac{q_\kappa \left(c_k - 1\right)\left(q_\kappa + 1\right)}{\left(q_\kappa + \chi_\phi\right)^2} - \lambda_1 d\Omega, \tag{A.25}$$

A.3 Local averaging volume constraint

The local averaging constraint functional $G_2\left(\bar{\chi}\left(\chi\right)\right)$ is defined as follows:

$$G_2 = \left(\frac{1}{n}\sum \bar{\chi}^p\right)^{1/p} - \bar{V}_{\max} \leq 0, \tag{A.26}$$

Using Lagrange's method, the extend constraint functional is formulated as

$$\begin{aligned}
\mathcal{G} :=& G_2 + \int_\Omega \bar{\chi}_A \left(-r^2 \nabla^2 \bar{\chi} + \bar{\chi} - \chi\right) d\Omega \\
=& G_2 + \int_\Omega -r^2 \bar{\chi} \nabla^2 \bar{\chi}_A + \bar{\chi}_A \left(\bar{\chi} - \chi\right) d\Omega + \int_{\partial\Omega} -\bar{\chi}_A \frac{\partial \bar{\chi}}{\partial \boldsymbol{n}} + \bar{\chi} \frac{\partial \bar{\chi}_A}{\partial \boldsymbol{n}} d\Gamma
\end{aligned} \tag{A.27}$$

Using the definition of Gâteaux derivative, the partial derivative of the extended constraint functional $\mathcal{G}$ with respect to $\bar{\chi}$ in the direction ξ at the stationary point will be:

$$\left\langle \frac{\partial \mathcal{G}}{\partial \bar{\chi}}, \xi \right\rangle = \int_\Omega -r^2 \xi \nabla^2 \bar{\chi}_A + \xi \bar{\chi}_A + \xi \frac{\partial G_2}{\partial \bar{\chi}} d\Omega + \int_{\partial\Omega} \xi \frac{\partial \bar{\chi}_A}{\partial \boldsymbol{n}} d\Gamma = 0. \tag{A.28}$$

The above equation should be satisfied with any arbitrary ξ. Therefore, the adjoint equation can be derived as follows:

$$\begin{cases} -r^2 \nabla^2 \bar{\chi}_A + \bar{\chi}_A = -\dfrac{\partial G_2}{\partial \bar{\chi}} & \text{in } \Omega \\ \nabla \bar{\chi}_A \cdot \boldsymbol{n} = 0 & \text{on } \partial\Omega. \end{cases} \tag{A.29}$$

The sensitivity for the local volume constraint can be thus obtained as

$$\mathcal{G}' = -\bar{\chi}_A. \tag{A.30}$$

By substituting Eq. (A.30) into Eq. (A.29), we can rewrite Eq. (A.29) as

$$\begin{cases} -r^2 \nabla^2 \mathcal{G}' + \mathcal{G}' = \dfrac{\partial G_2}{\partial \bar{\chi}} & \text{in } \Omega \\ \nabla \mathcal{G}' \cdot \boldsymbol{n} = 0 & \text{on } \partial\Omega, \end{cases} \tag{A.31}$$

where $\dfrac{\partial G_2}{\partial \bar{\chi}}$ is expressed as

$$\frac{\partial G_2}{\partial \bar{\chi}} = \frac{\bar{\chi}^{p-1} \left(\dfrac{1}{n} \sum \bar{\chi}^p \right)^{\frac{1}{p}-1}}{n}. \tag{A.32}$$

Appendix B

FreeFEM Code Implementation

B.1 Natural convection

B.1.1 Adjoint equations

The FreeFEM code implementation for the adjoint equation Eq. (4.20) is briefly illustrated here. First, we define a vector field for the adjoint velocity, adjoint pressure, and adjoint temperature. Since the mini-element is already supported in FreeFEM, we declare in the script as `func Pk = [P1b, P1b, P1b, P1, P1]`. Next, we create a new finite element space as `fespace VhV1(Sh, Pk)` that is associated with $\tilde{V} \times \tilde{V} \times \tilde{V} \times \tilde{P} \times \tilde{P}$. Then, we define unknowns by declaring `VhV1<real> [ua1,ua2,ua3,pa,Ta]` for adjoint variables, and `VhV1<real> [uau1,uau2,uau3,pap,TaT]` for the corresponding test functions. After that, we use the `macro` to define the material interpolation scheme in Eq. (4.11) and the operators appears in Eq. (4.20), as follows:

```
macro kappa(chi) 1.0+(Ck-1.0)*(qkappa*(1-chi)/(qkappa+chi))//
macro alpha(chi) (alphamax*(qalpha*(1-chi))/(qalpha+chi))//
macro grad(u)[dx(u), dy(u), dz(u)]//
macro Grad(u)[grad(u#1), grad(u#2), grad(u#3)]//
macro div(u)(dx(u#1) + dy(u#2) + dz(u#3))//
macro UgradV1(u1,u2,u3,v1,v2,v3)[[u1,u2,u3]'*[dx(v1),dx(v2),dx(v3)],
[u1,u2,u3]'*[dy(v1),dy(v2),dy(v3)],
[u1,u2,u3]'*[dz(v1),dz(v2),dz(v3)]]//
macro UgradV2(u1,u2,u3,v1,v2,v3)[[u1,u2,u3]'*[dx(v1),dy(v1),dz(v1)],
[u1,u2,u3]'*[dx(v2),dy(v2),dz(v2)],
[u1,u2,u3]'*[dx(v3),dy(v3),dz(v3)]]//
```

Finally, the variational formulation can be coded using the built-in syntax `varf`. It is to build the matrix and the right-hand side vector of the linear system. All these technical issues related to the finite element method are hidden and such advantage makes the script look like the mathematical formulations:

```
varf Adj ([ua1,ua2,ua3,pa,Ta],[uau1,uau2,uau3,pap,TaT])
= intN(Sh)(
// (ua*grad)u^T
UgradV1(ua1, ua2, ua3, u1, u2, u3)' * [uau1,uau2,uau3]
// -(u*grad)ua
- UgradV2(u1, u2, u3, ua1, ua2, ua3)' * [uau1,uau2,uau3]
// the -Pr*Lap(ua)
+ Pr * ( Grad(ua):Grad(uau) )
// Brinkman model, alpha*ua
+ alpha(chiP)*[ua1,ua2,ua3]'*[uau1,uau2,uau3]
// the grad(pa)
- div(uau)*pa
// Ta*grad(T)
+ [uau1,uau2,uau3]' * grad(T) * Ta
// the Continuity
- div(ua)*pap
// the Bouyancy force -Gr*Pr^2*ua*(0,1,0)'
- (1./nu)*Pr^2*TaT*[ua1,ua2,ua3]'*[0,1,0]
// the-grad(Ta)*u
- TaT * grad(Ta)' * [u1,u2,u3]
// the kappa*Lap(Ta)
+ kappa(chiP) * grad(Ta)'*grad(TaT)
)
// the Heat source term
+ intN(Sh, HeatSource)(-HtS*TaT)

// Adjoint Boundary Conditions for velocity field
+ on(wall, ua1=0,ua2=0,ua3=0) //Dirichlet velocity B.C
+ on(sym1, ua3=0) // sysmetric B.C (uz=0)
+ on(sym2, ua1=0) // sysmetric B.C (ux=0)
// Adjoint Boundary Conditions for temperature field
+ on(Twall, Ta=0) //Dirichlet temperature B.C.
+ intN1(Sh,Adiabatic)(
TaT * Ta * [u1,u2,u3]' * [N.x, N.y, N.z]
) // Temperature Neumann B.C.
;
```

B.1.2 Body-fitted mesh adaptation

The FreeFEM code implementation for the body-fitted mesh is presented here (cf. Section 4.3.3). The sequential version of Mmg can be called within FreeFEM, as follows:

```
load "mmg"
```

```
ShtruncGlobal = mmg3d(ShtruncGlobal, metric=ophiGlobal[], iso=true, hmin=hmin, hmax=
    hmax, hgrad = hgrad, hausd=hausd, localParameter = lp, requiredTriangle = rt);
```

The input parameters are listed as follows:

- **iso**: if true, allows the implicit domain mesh (body-fitted) adaptation;
- **hmax, hmin**: maximum and minimum edge size, respectively;
- **hgrad**: imposes two adjacent edges e_1 and e_2 to satisfy $\frac{1}{h_{\text{grad}}} \leq \frac{l_{e_1}}{l_{e_2}} \leq h_{\text{grad}}$;
- **hausd**: imposes the maximal distance between the piecewise linear representation of the boundary and the reconstructed ideal boundary;
- **localParameter**: associates local Hausdorff, minimal edge size and maximal edge size to boundary references. The local parameters overwrite the global ones;
- **requiredTriangle**: associates the unchanged elements to the boundary reference.

B.1.3 Anisotropic mesh adaptation

As for the anisotropic mesh used in the transient simulation solver (cf. Section 4.3.3), in 2D case (see Fig. 4.8), we use the built-in function `adaptmesh` offered by FreeFEM:

```
ShGlobal = adaptmesh(ShGlobal, [uG,uGB], ratio = ratio, err = err, hmax = hmax, hmin =
    hmin);
```

For 3D simulation (see Fig. 4.9), the mesh algorithm can be performed by ParMmg, a parallel version of Mmg recently developed by Cirrottola and Froehly (2021). First, the metric is saved by `mshmet`. Then, we call ParMmg to read the metric and to generate the new mesh using the following script:

```
load "mshmet"
real[int] met = mshmet(ShGlobal, [uG,uGB,uGC], aniso = 1, hmin = hmin, hmax = hmax, err
     = err, nbregul = 1, normalization = 1);
load "parmmg"
ShGlobal = parmmg3d(ShGlobal, metric = met, hgrad = hgrad,comm=mpiCommWorld);
```

The input parameters are listed as follows:

- **ratio**: ratio for a prescribed smoothing on the metric (1.5 by default);
- **err**: interpolation error level (0.01 by default);

- **metric**: array of 3 real arrays to set or get metric data information;
- **aniso**: if true, allows the adapted mesh to be anisotropic.

B.2 Local averaging volume constraint

Here we briefly illustrate the FreeFEM code implementation for the distributed computing of the adjoint equation Eq. (6.13). As has been discussed in Section 6.3.2, FreeFEM is used for the discretization of the PDEs, and PETSc for linear algebra backend, and it has been interfaced in FreeFEM. To call PETSc within FreeFEM, we first load the necessary plugins as

```
load "PETSc" // PETSc plugin
macro dimension()3// for 3D problems
include "macro_ddm.idp" //additional DDM functions
```

We define a scalar field by declaring in the script as `func Pk1= [P1]` since the P1 linear element is used in the present work. Next, an external mesh file $\mathcal{T}$ can be read by FreeFEM. For instance, as for the "hand" and "bird beak" examples shown in Section 6.4.2, we first generate the global mesh file in Gmsh (Geuzaine and Remacle, 2009) and store it in the Inria Medit format. Then they can be natively parsed by FreeFEM. After that, the global mesh $\mathcal{T}$ is partitioned into N meshes $\{\mathcal{T}\}_{1\leq 1\leq N}$ using a graph partitioner package such as METIS. This domain decomposition step can be achieved by calling `buildDmesh`. Note that there are ghost elements in the overlapping domains along the skeletons between each subdomain. They are used to help multiple MPI processes to communicate one with another. Then we create the PETSc matrix with the script `Mat`. Then using `createMat`, we let FreeFEM interact with PETSc to distribute parallel matrix.

```
meshN Sh=readmesh3("./Hand.mesh"); // read external global mesh
buildDmesh(Sh);
Mat B4; // parallel PETSc matrix
createMat(Sh, B4, Pk1) // parallel finite element numbering
```

Then, the finite element space can be created with the script `fespace VhS1(Sh,Pk1)` which is associated to Eq. (B.1).

$$\mathscr{P} := \left\{ \tilde{p} \in H^1(\Omega) \mid \tilde{p} = 0 \text{ on } \partial\Omega_p^D \right\}. \tag{B.1}$$

After that, the unknowns can be defined as `VhS1<real> def1(sensV), def1(testsensV), def1(sensP)`, which associate to $\mathcal{G}'$, $\tilde{\mathcal{G}}'$, and $\frac{\partial G_2}{\partial \bar{\chi}}$, respectively.

Next, we define the weak formulation as in Eq. (B.2) on the distributed mesh.

$$\int_\Omega r^2 \nabla\tilde{\mathcal{G}}' \cdot \nabla\mathcal{G}' + \tilde{\mathcal{G}}'\mathcal{G}' - \tilde{\mathcal{G}}' \frac{\partial G_2}{\partial \bar{\chi}} d\Omega = 0 \quad \forall \tilde{\mathcal{G}}' \in \mathscr{P}, \mathcal{G}' \in \mathscr{P}. \tag{B.2}$$

The variational formulation can be coded using the built-in syntax `varf`.

```
varf Adjoint(sensV,testsensV)
= intN(Sh,qforder=3)((radiusX^2*dx(sensV)*dx(testsensV)+radiusY^2*dy(sensV)*dy(
    testsensV)+radiusZ^2*dz(sensV)*dz(testsensV)) + sensV*testsensV)
+ intN(Sh,qforder=3)(sensP*testsensV);
```

`qforder` is the quadrature formula as follows:

$$\int_{\Omega} f(\boldsymbol{x}) \approx \sum_{\ell=1}^{L} \omega_{\ell} f\left(\boldsymbol{\xi}_{\ell}\right). \tag{B.3}$$

In two-dimensional cases where `qfroder=3`, the quadrature formula is exact on $\mathbb{P}_2$[1].

Finally, we assemble the variational formulation inside the parallel matrix and define the right hand side. And we call *hypre* (Falgout and Yang, 2002) to solve the linear equation as

```
real[int] Adjointrhs = Adjoint(0, VhS1); // right hand side
B4 = Adjoint(VhS1, VhS1); // parallel finite element assembly
set(B4, sparams = "-pc_type hypre -ksp_type gmres -ksp_max_it 200");
sensV[] = B4^-1 * Adjointrhs;
```

The obtained sensitivity is normalized by $\max_{\forall i}\left(\mathcal{G}_i'\right)$. To this end, we use a standard MPI reduction as

```
real sensVmaxloc = sensV[].max;
real sensVmax;
mpiAllReduce(sensVmaxloc, sensVmax, mpiCommWorld, mpiMAX);
sensV = sensV/sensVmax;
```

To post-process the results, one can output them in the `.vtk` format using `savevtk`. For the distributed computing, the outputs include N `.vtu` files and one single `.pvd` file. Each `.vtu` file store the mesh and data for one MPI process and they can be gathered by the `.pvd` file.

```
int[int] order = [1];
savevtk("./sensV.vtu", Sh, sensV, dataname = "sensV", order = order);
```

B.3 An educational code for mean compliance problem based on the density approach

This part of the work is for educational purposes. We solve a minimal mean compliance problem given in Chapter 2. The density approach is adopted, as discussed in Section 1.2.1. The optimality

[1] https://doc.freefem.org/references/quadrature-formulae.html#qf2pt

criteria is used to update the design variables. Readers are referred to in our recent educational paper for more details (Zhu, Zhang, Li, Liang, Wang, Li, and Nishiwaki, 2021).

```
// Macros
macro el(ux,uy)  [dx(ux), (dx(uy)+dy(ux)), dy(uy) ] // Linear strain
macro e(ux,uy)   (el(ux,uy) + enl(ux,uy)) //

real  L = 2; // Length of the design domain
real  W = 1; // Width of the design domain
real  E1 = 3e9;    // Young's modulus for solid material
real E0 = 1e-9*E1;  // Young's modulus for void material
real  nu = 0.4;    // Poison's ratio
real  fx = 0;      // External load, x direction
real  fy = -1e6;    // External load, y direction
real  volfrac = 0.4;  // Target volume fraction
real  p = 1;      // Penalty
real  change = 1;    // Maximum change of design variable
int  s = 1; // Index to controll the meshfine
int  i = 1;       // Optimization iteration number
int  Imax = 200;    // Maximum iteration number

// Border: Cantilever
int loaded = 1, free = 2, fixed = 3;
border b1 (t = -0.025*W, 0.025*W) {x = 0.5*L; y = t; label = loaded;}
border b2 (t = 0.025*W, 0.5*W)  {x = 0.5*L; y = t; label = free;}
border b3 (t = 0.5*L, -0.5*L)  {x = t; y = 0.5*W; label = free;}
border b4 (t = 0.5*W, -0.5*W)  {x = -0.5*L; y = t; label = fixed;}
border b5 (t = -0.5*L, 0.5*L)  {x = t; y = -0.5*W; label = free;}
border b6 (t = -0.5*W, -0.025*W) {x = 0.5*L; y = t; label = free;}

// Mesh
mesh th = buildmesh(b1(2*s) + b2(19*s) + b3(160*s) + b4(40*s) +b5(160*s) + b6(19*s));

// Fespace: define all the variables
fespace Vh (th, [P1, P1]);
Vh [ux, uy], [vx, vy];
fespace Vh1 (th, P1);
Vh1 E, theta, testtheta, oldtheta, sens, thetaold, thetanew, dtheta, sensnew, vv, gama;

// Make intial design
theta = volfrac;

// Map theta to the material property
E = theta^p*(E1 - E0) + E0;

// Form A matrix
```

```
real lambda = nu/((1+nu)*(1-2*nu));
real mu = 1/(2*(1+nu));
real a11= 2*mu + lambda ;
real a22= mu ;
real a33= 2*mu + lambda ;
real a12= 0 ;
real a13= lambda ;
real a23= 0 ;
real a21= a12 ;
real a31= a13 ;
real a32= a23 ;
func A = [ [ a11,a12,a13],[ a21,a22,a23],[ a31,a32,a33] ];

// Optimization loop
while (change > 1e-3 && i < Imax){
  i = i + 1;
  thetaold = theta;
  p = min(3., p + (i%5 == 0)*0.2); // Penalty update
  // Linear finite element analysis
      ---------------------------------------------------------
  solve linear([ux, uy], [vx, vy]) =
  int2d(th)( E*(el(ux,uy)'*A*el(vx,vy)) )
  - int1d(th, loaded)(fx*vx + fy*vy)
  + on(fixed, ux = 0, uy = 0);


  // Sensitivity and smoothing
      ---------------------------------------------------------
  // sens = -p*theta^(p-1)*(E1 - E0)*((el(uxa,uya))'*A*(el(ux,uy)));
  sens = -p*theta^(p-1)*(E1 - E0)*((el(ux,uy))'*A*(el(ux,uy)));
  solve smoothing (sensnew,vv) = int2d(th)( 0.002*( dx(sensnew)*dx(vv)+dy(sensnew)*dy(vv)
       ) + sensnew*vv ) - int2d(th)(sens*vv);
  sens = sensnew;

  // OC update ------------------------------------------------------------
  real l1 = 0; real l2 = 100000; real move = 0.1;
  while ((l2-l1)/(l2+l1) > (1e-4)&&l2>1e-40){
    real lmid = 0.5*(l2+l1);
    thetanew = max(0., max(theta - move, min(1., min(theta + move, theta*(max(1e-10, -
        sens/lmid))^0.3))));
    if ((int2d(th)(thetanew)- int2d(th)(volfrac)) > 0){
      l1 = lmid;
    }
    else{
      l2 = lmid;
    }
```

```
  }
  theta = thetanew;
  E = theta^p*(E1 - E0) + E0;

  // Objective functions and visualization
      ---------------------------------------------------------------
  real comp = int1d(th, loaded)(fx*ux + fy*uy);
  real vol = int2d(th)(theta)/int2d(th)(1); // volume fraction
  dtheta = abs(theta - thetaold);
  change = dtheta[].max;
  plot(theta, fill =1, grey=true);
  cout <<"iter = "<< i <<"; comp = "<<comp<<"; vol = "<<vol <<"; change ="<< change <<"
      .----------------------"<<endl;
}
```

References

Aage, Niels, Erik Andreassen, and Boyan Stefanov Lazarov (2015). "Topology optimization using PETSc: An easy-to-use, fully parallel, open source topology optimization framework". In: *Structural and Multidisciplinary Optimization* 51.3, pp. 565–572.

Aage, Niels, Erik Andreassen, Boyan Stefanov Lazarov, and Ole Sigmund (2017). "Giga-voxel computational morphogenesis for structural design". In: *Nature* 550.7674, pp. 84–86.

Aage, Niels and Boyan S Lazarov (2013). "Parallel framework for topology optimization using the method of moving asymptotes". In: *Structural and multidisciplinary optimization* 47.4, pp. 493–505.

Aage, Niels, Thomas H Poulsen, Allan Gersborg-Hansen, and Ole Sigmund (2008). "Topology optimization of large scale stokes flow problems". In: *Structural and Multidisciplinary Optimization* 35.2, pp. 175–180.

Abhyankar, Shrirang, Jed Brown, Emil M Constantinescu, Debojyoti Ghosh, Barry F Smith, and Hong Zhang (2018). "PETSc/TS: A Modern Scalable ODE/DAE Solver Library". In: *arXiv preprint arXiv:1806.01437*.

Adams, Mark, Harun H. Bayraktar, Tony M. Keaveny, and Panayiotis Papadopoulos (2004). "Ultrascalable Implicit Finite Element Analyses in Solid Mechanics with over a Half a Billion Degrees of Freedom". In: *Proceedings of the 2004 ACM/IEEE Conference on Supercomputing*. SC04. IEEE Computer Society, 34:1–34:15.

Aguilar, Juan C and Jonathan B Goodman (2006). "Anisotropic mesh refinement for finite element methods based on error reduction". In: *Journal of Computational and Applied Mathematics* 193.2, pp. 497–515.

Alexandersen, Joe, Niels Aage, Casper Schousboe Andreasen, and Ole Sigmund (2014). "Topology optimisation for natural convection problems". In: *International Journal for Numerical Methods in Fluids* 76.10, pp. 699–721.

Alexandersen, Joe and Casper Schousboe Andreasen (2020). "A review of topology optimisation for fluid-based problems". In: *Fluids* 5.1, p. 29.

Alexandersen, Joe, Ole Sigmund, and Niels Aage (2016). "Large scale three-dimensional topology optimisation of heat sinks cooled by natural convection". In: *International Journal of Heat and Mass Transfer* 100, pp. 876–891.

Alexandersen, Joe, Ole Sigmund, Knud Erik Meyer, and Boyan Stefanov Lazarov (2018). "Design of passive coolers for light-emitting diode lamps using topology optimisation". In: *International Journal of Heat and Mass Transfer* 122, pp. 138–149.

Allaire, Grégoire, Lorenzo Cavallina, Nobuhito Miyake, Tomoyuki Oka, and Toshiaki Yachimura (2019). "The homogenization method for topology optimization of structures: old and new". In: *Interdisciplinary Information Sciences* 25.2, pp. 75–146.

Allaire, Grégoire, Charles Dapogny, and Pascal Frey (2013). "A mesh evolution algorithm based on the level set method for geometry and topology optimization". In: *Structural and Multidisciplinary Optimization* 48.4, pp. 711–715.

Allaire, Grégoire, Frédéric De Gournay, François Jouve, and Anca-Maria Toader (2005). "Structural optimization using topological and shape sensitivity via a level set method". In: *Control and Cybernetics* 34.1, p. 59.

Allaire, Grégoire, Perle Geoffroy-Donders, and Olivier Pantz (2019). "Topology optimization of modulated and oriented periodic microstructures by the homogenization method". In: *Computers & Mathematics with Applications* 78.7, pp. 2197–2229.

Allaire, Grégoire, François Jouve, and Anca-Maria Toader (2004). "Structural optimization using sensitivity analysis and a level-set method". In: *Journal of Computational Physics* 194.1, pp. 363–393.

Allaire, Grégoire and Olivier Pantz (2006). "Structural optimization with FreeFem++". In: *Structural and Multidisciplinary Optimization* 32.3, pp. 173–181.

Alonso, Diego Hayashi, Juan Sergio Romero Saenz, and Emilio Carlos Nelli Silva (2020). "Non-newtonian laminar 2D swirl flow design by the topology optimization method". In: *Structural and multidisciplinary optimization* 62.1, pp. 299–321.

Aly, Abdelraheem M (2020). "Mixing between solid and fluid particles during natural convection flow of a nanofluid-filled H-shaped cavity with three center gates using ISPH method". In: *International Journal of Heat and Mass Transfer* 157, p. 119803.

Aly, Abdelraheem M and ZAS Raizah (2020). "Incompressible smoothed particle hydrodynamics simulation of natural convection in a nanofluid-filled complex wavy porous cavity with inner solid particles". In: *Physica A: Statistical Mechanics and its Applications* 537, p. 122623.

Aly, Abdelraheem M, Zehba Raizah, and Amal Al-Hanaya (2021). "Double rotations between an inner wavy shape and a hexagonal-shaped cavity suspended by NEPCM using a time-fractional derivative of the ISPH method". In: *International Communications in Heat and Mass Transfer* 127, p. 105533.

Arnold, Douglas N, Franco Brezzi, and Michel Fortin (1984). "A stable finite element for the Stokes equations". In: *Calcolo* 21.4, pp. 337–344.

Asmussen, Janus, Joe Alexandersen, Ole Sigmund, and Casper Schousboe Andreasen (2019). "A "poor man's" approach to topology optimization of natural convection problems". In: *Structural and Multidisciplinary Optimization* 59.4, pp. 1105–1124.

Autodesk (n.d.). "PowerShape". In: ().

Bacuta, Constantin (2006). "A unified approach for Uzawa algorithms". In: *SIAM Journal on Numerical Analysis* 44.6, pp. 2633–2649.

Baiges, Joan, Jesús Martínez-Frutos, David Herrero-Pérez, Fermin Otero, and Alex Ferrer (2019). "Large-scale stochastic topology optimization using adaptive mesh refinement and coarsening

through a two-level parallelization scheme". In: *Computer Methods in Applied Mechanics and Engineering* 343, pp. 186–206.

Balasubramanian, K, PS Lee, CJ Teo, and SK Chou (2013). "Flow boiling heat transfer and pressure drop in stepped fin microchannels". In: *International journal of heat and mass transfer* 67, pp. 234–252.

Balay, Satish, Shrirang Abhyankar, Mark F. Adams, Steven Benson, Jed Brown, Peter Brune, Kris Buschelman, Emil Constantinescu, Lisandro Dalcin, Alp Dener, Victor Eijkhout, William D. Gropp, Václav Hapla, Tobin Isaac, Pierre Jolivet, Dmitry Karpeev, Dinesh Kaushik, Matthew G. Knepley, Fande Kong, Scott Kruger, Dave A. May, Lois Curfman McInnes, Richard Tran Mills, Lawrence Mitchell, Todd Munson, Jose E. Roman, Karl Rupp, Patrick Sanan, Jason Sarich, Barry F. Smith, Stefano Zampini, Hong Zhang, Hong Zhang, and Junchao Zhang (2021). *PETSc/TAO Users Manual*. Tech. rep. ANL-21/39 - Revision 3.16. Argonne National Laboratory.

Balay, Satish, Shrirang Abhyankar, Mark F. Adams, Jed Brown, Peter Brune, Kris Buschelman, Lisandro Dalcin, Alp Dener, Victor Eijkhout, William D. Gropp, Dmitry Karpeyev, Dinesh Kaushik, Matthew G. Knepley, Dave A. May, Lois Curfman McInnes, Richard Tran Mills, Todd Munson, Karl Rupp, Patrick Sanan, Barry F. Smith, Stefano Zampini, Hong Zhang, and Hong Zhang (2019). *PETSc Web page*. https://www.mcs.anl.gov/petsc. URL: https://www.mcs.anl.gov/petsc.

Balay, Satish, William D. Gropp, Lois Curfman McInnes, and Barry F. Smith (1997). "Efficient Management of Parallelism in Object Oriented Numerical Software Libraries". In: *Modern Software Tools in Scientific Computing*. Ed. by E. Arge, A. M. Bruaset, and H. P. Langtangen. Birkhäuser Press, pp. 163–202.

Baldry, Mark, Victoria Timchenko, and Chris Menictas (2019). "Optimal design of a natural convection heat sink for small thermoelectric cooling modules". In: *Applied Thermal Engineering* 160, p. 114062.

Barzegari, Mojtaba, Di Mei, Sviatlana V Lamaka, and Liesbet Geris (2021). "Computational modeling of degradation process of biodegradable magnesium biomaterials". In: *Corrosion Science* 190, p. 109674.

Bazilevs, Yuri, Kenji Takizawa, and Tayfun E Tezduyar (2015). *New directions and challenging computations in fluid dynamics modeling with stabilized and multiscale methods*.

Beghini, Lauren L, Alessandro Beghini, Neil Katz, William F Baker, and Glaucio H Paulino (2014). "Connecting architecture and engineering through structural topology optimization". In: *Engineering Structures* 59, pp. 716–726.

Behrou, Reza, Ram Ranjan, and James K Guest (2019). "Adaptive topology optimization for incompressible laminar flow problems with mass flow constraints". In: *Computer Methods in Applied Mechanics and Engineering* 346, pp. 612–641.

Bejan, Adrian, Alex J Fowler, and George Stanescu (1995). "The optimal spacing between horizontal cylinders in a fixed volume cooled by natural convection". In: *International journal of heat and mass transfer* 38.11, pp. 2047–2055.

Bendsøe, Martin P (1989). "Optimal shape design as a material distribution problem". In: *Structural optimization* 1.4, pp. 193–202.

— (1995). *Optimization of structural topology, shape, and material*. Vol. 414. Springer.

Bendsøe, Martin P and Ole Sigmund (1999). "Material interpolation schemes in topology optimization". In: *Archive of Applied Mechanics* 69.9-10, pp. 635–654.

Bendsøe, Martin Philip and Noboru Kikuchi (1988). "Generating optimal topologies in structural design using a homogenization method". In: *Computer Methods in Applied Mechanics and Engineering* 71.2, pp. 197–224.

Besserud, Keith, Neil Katz, and Alessandro Beghini (2013). "Structural emergence: architectural and structural design collaboration at SOM". In: *Architectural Design* 83.2, pp. 48–55.

Birmingham, Lauren, James Grogan, Glen Niebur, Laoise McNamara, and Peter McHugh (2013). "Computational modelling of the mechanics of trabecular bone and marrow using fluid structure interaction techniques". In: *Annals of Biomedical Engineering* 41.4, pp. 814–826.

Borouchaki, Houman, Manuel Castro-Diaz, Paul Louis George, Frédéric Hecht, and Bijan Mohammadi (1996). "Anisotropic adaptive mesh generation in two dimensions for CFD". In: *Numerical grid generation in computational field simulations*, pp. 197–206.

Borrvall, Thomas and Joakim Petersson (2001). "Large-scale topology optimization in 3D using parallel computing". In: *Computer methods in Applied Mechanics and Engineering* 190.46-47, pp. 6201–6229.

— (2003). "Topology optimization of fluids in Stokes flow". In: *International journal for numerical methods in fluids* 41.1, pp. 77–107.

Bruns, Tyler E (2007). "Topology optimization of convection-dominated, steady-state heat transfer problems". In: *International Journal of Heat and Mass Transfer* 50.15-16, pp. 2859–2873.

Burger, Martin (2003). "A framework for the construction of level set methods for shape optimization and reconstruction". In: *Interfaces and Free boundaries* 5.3, pp. 301–329.

Campen, Marcel, David Bommes, and Leif Kobbelt (2015). "Quantized global parametrization". In: *Acm Transactions On Graphics (TOG)* 34.6, pp. 1–12.

Castro-Diaz, Manuel, Frédéric Hecht, and Bijan Mohammadi (2000). "Anisotropic grid adaptation for inviscid and viscous flows simulations". In: *International Journal of Computational Fluid Dynamics* 25, pp. 475–491.

Challis, Vivien J and James K Guest (2009). "Level set topology optimization of fluids in Stokes flow". In: *International journal for numerical methods in engineering* 79.10, pp. 1284–1308.

Chemisana, Daniel (2011). "Building integrated concentrating photovoltaics: a review". In: *Renewable and sustainable energy reviews* 15.1, pp. 603–611.

Chu, D Nha, YM Xie, A Hira, and GP Steven (1996). "Evolutionary structural optimization for problems with stiffness constraints". In: *Finite elements in analysis and design* 21.4, pp. 239–251.

Cirrottola, Luca and Algiane Froehly (2021). "Parallel Unstructured Mesh Adaptation Based on Iterative Remershing and Repartitioning". In: *WCCM-Eccomas 2020-14th World Congress on Computational Mechanic*.

Coffin, Peter and Kurt Maute (2016a). "A level-set method for steady-state and transient natural convection problems". In: *Structural and Multidisciplinary Optimization* 53.5, pp. 1047–1067.

— (2016b). "Level set topology optimization of cooling and heating devices using a simplified convection model". In: *Structural and multidisciplinary optimization* 53.5, pp. 985–1003.

COMSOL (2018). "COMSOL Multiphysics® v. 5.4. www.comsol.com. COMSOL AB, Stockholm, Sweden." In.

Dapogny, Charles, Cécile Dobrzynski, and Pascal Frey (2014). "Three-dimensional adaptive domain remeshing, implicit domain meshing, and applications to free and moving boundary problems". In: *Journal of Computational Physics* 262, pp. 358–378.

Dapogny, Charles, Alexis Faure, Georgios Michailidis, Grégoire Allaire, Agnes Couvelas, and Rafael Estevez (2017). "Geometric constraints for shape and topology optimization in architectural design". In: *Computational Mechanics* 59.6, pp. 933–965.

Dede, Ercan M (2009). "Multiphysics topology optimization of heat transfer and fluid flow systems". In: *proceedings of the COMSOL Users Conference*.

Dede, Ercan M, Yuqing Zhou, and Tsuyoshi Nomura (2020). "Inverse design of microchannel fluid flow networks using Turing pattern dehomogenization". In: *Structural and Multidisciplinary Optimization* 62.4, pp. 2203–2210.

Dilgen, Cetin B, Sumer B Dilgen, David R Fuhrman, Ole Sigmund, and Boyan S Lazarov (2018a). "Topology optimization of turbulent flows". In: *Computer Methods in Applied Mechanics and Engineering* 331, pp. 363–393.

Dilgen, Sumer B, Cetin B Dilgen, David R Fuhrman, Ole Sigmund, and Boyan S Lazarov (2018b). "Density based topology optimization of turbulent flow heat transfer systems". In: *Structural and Multidisciplinary Optimization* 57.5, pp. 1905–1918.

Ding, Xiaohong and Koetsu Yamazaki (2005). "Adaptive growth technique of stiffener layout pattern for plate and shell structures to achieve minimum compliance". In: *Engineering Optimization* 37.3, pp. 259–276.

Dolean, Victorita, Pierre Jolivet, and Frédéric Nataf (2015). *An introduction to domain decomposition methods: algorithms, theory, and parallel implementation*. SIAM.

Dou, Suguang (2020). "A projection approach for topology optimization of porous structures through implicit local volume control". In: *Structural and Multidisciplinary Optimization* 62.2, pp. 835–850.

Duan, Xianbao, Feifei Li, and Xinqiang Qin (2016). "Topology optimization of incompressible Navier–Stokes problem by level set based adaptive mesh method". In: *Computers & Mathematics with Applications* 72.4, pp. 1131–1141.

Duan, Xianbao, Yichen Ma, and Rui Zhang (2008). "Optimal shape control of fluid flow using variational level set method". In: *Physics letters A* 372.9, pp. 1374–1379.

Eschenauer, Hans A, Vladimir V Kobelev, and Axel Schumacher (1994). "Bubble method for topology and shape optimization of structures". In: *Structural Optimization* 8.1, pp. 42–51.

Falgout, Robert and Ulrike Yang (2002). "*hypre*: a library of high performance preconditioners". In: *Computational Science—ICCS 2002*, pp. 632–641.

Fawaz, Ahmad, Yuchao Hua, Steven Le Corre, Yilin Fan, and Lingai Luo (2022). "Topology optimization of heat exchangers: A review". In: *Energy*, p. 124053.

Feppon, Florian (2019). "Shape and topology optimization of multiphysics systems". PhD thesis. Paris Saclay.

Feppon, Florian, Grégoire Allaire, Felipe Bordeu, Julien Cortial, and Charles Dapogny (2019). "Shape optimization of a coupled thermal fluid–structure problem in a level set mesh evolution framework". In: *SeMA Journal* 76.3, pp. 413–458.

Feppon, Florian, Grégoire Allaire, Charles Dapogny, and Pierre Jolivet (2020a). "Topology optimization of thermal fluid–structure systems using body-fitted meshes and parallel computing". In: *Journal of Computational Physics* 417, p. 109574.

— (2020b). "Topology optimization of thermal fluid–structure systems using body-fitted meshes and parallel computing". In: *Journal of Computational Physics* 417, p. 109574.

— (2021). "Body-fitted topology optimization of 2D and 3D fluid-to-fluid heat exchangers". In: *Computer Methods in Applied Mechanics and Engineering* 376, p. 113638.

Ferro, Nicola, Simona Perotto, and Matteo Gavazzoni (2022). "A new fluid-based strategy for the connection of non-matching lattice materials". In: *arXiv preprint arXiv:2206.00994*.

Fortin, Michel and Franco Brezzi (1991). *Mixed and hybrid finite element methods*. New York: Springer-Verlag.

Frey, Pascal Jean and Paul-Louis George (1999). *Maillages: applications aux éléments finis*. Hermès Science Publications.

Gallagher, Richard H and Olgierd Cecil Zienkiewicz (1973). "Optimum structural design: Theory and applications(Book- Optimum structural design: Theory and applications.)" In: *London, John Wiley and Sons, Ltd., 1973. 360 p*.

Garcke, Harald, Michael Hinze, Christian Kahle, and Kei Fong Lam (2018). "A phase field approach to shape optimization in Navier–Stokes flow with integral state constraints". In: *Advances in Computational Mathematics* 44.5, pp. 1345–1383.

Geoffroy-Donders, Perle, Grégoire Allaire, and Olivier Pantz (2020). "3-d topology optimization of modulated and oriented periodic microstructures by the homogenization method". In: *Journal of Computational Physics* 401, p. 108994.

George, Paul-Louis and Houman Borouchaki (1998). "Delaunay triangulation and meshing. 1. vyd. Paris". In: *Hermes*.

Gersborg-Hansen, Allan, Ole Sigmund, and Robert B. Haber (2005). "Topology optimization of channel flow problems". In: *Structural and multidisciplinary optimization* 30.3, pp. 181–192.

Gerzen, Nikolai, Thorsten Mertins, and Claus BW Pedersen (2022). "Geometric dimensionality control of structural components in topology optimization". In: *Structural and Multidisciplinary Optimization* 65.5, pp. 1–17.

Geuzaine, Christophe and Jean-François Remacle (2009). "Gmsh: A 3-D finite element mesh generator with built-in pre- and post-processing facilities". In: *International Journal for Numerical Methods in Engineering* 79.11, pp. 1309–1331.

Ghasemi, Ali and Ali Elham (2022). "Efficient multi-stage aerodynamic topology optimization using an operator-based analytical differentiation". In: *Structural and Multidisciplinary Optimization* 65.4, pp. 1–22.

Gingold, Robert A and Joseph J Monaghan (1977). "Smoothed particle hydrodynamics: theory and application to non-spherical stars". In: *Monthly notices of the royal astronomical society* 181.3, pp. 375–389.

Groen, Jeroen P, Florian C Stutz, Niels Aage, Jakob A Bærentzen, and Ole Sigmund (2020). "Dehomogenization of optimal multi-scale 3D topologies". In: *Computer Methods in Applied Mechanics and Engineering* 364, p. 112979.

Guo, Xu, Weisheng Zhang, and Wenliang Zhong (2014). "Doing topology optimization explicitly and geometrically—a new moving morphable components based framework". In: *Journal of Applied Mechanics* 81.8.

Guzina, Bojan B and Marc Bonnet (2004). "Topological derivative for the inverse scattering of elastic waves". In: *Quarterly Journal of Mechanics and Applied Mathematics* 57.2, pp. 161–179.

He, Yunzhen, Kun Cai, Zi-Long Zhao, and Yi Min Xie (2020). "Stochastic approaches to generating diverse and competitive structural designs in topology optimization". In: *Finite Elements in Analysis and Design* 173, p. 103399.

Hecht, Frédéric (2012). "New development in FreeFem++". In: *Journal of Numerical Mathematics* 20.3-4, pp. 251–266.

Hecht, Frédéric and Bijan Mohammadi (1997). "Mesh adaption by metric control for multi-scale phenomena and turbulence". In: *35th Aerospace Sciences Meeting and Exhibit*, p. 859.

Hestenes, Magnus R. (1969). "Multiplier and gradient methods". In: *Journal of Optimization Theory and Applications* 4.5, pp. 303–320.

Hong, Sihui, Bohan Zhang, Chaobin Dang, and Eiji Hihara (2020). "Development of two-phase flow microchannel heat sink applied to solar-tracking high-concentration photovoltaic thermal hybrid system". In: *Energy* 212, p. 118739.

Huang, Xiaodong and Mike Xie (2010). *Evolutionary topology optimization of continuum structures: methods and applications*. John Wiley & Sons.

Iga, Atsuro, Shinji Nishiwaki, Kazuhiro Izui, and Masataka Yoshimura (2009). "Topology optimization for thermal conductors considering design-dependent effects, including heat conduction and convection". In: *International Journal of Heat and Mass Transfer* 52.11-12, pp. 2721–2732.

Jenkins, Nicholas and Kurt Maute (2015). "Level set topology optimization of stationary fluid-structure interaction problems". In: *Structural and Multidisciplinary Optimization* 52.1, pp. 179–195.

— (2016). "An immersed boundary approach for shape and topology optimization of stationary fluid-structure interaction problems". In: *Structural and Multidisciplinary Optimization* 54.5, pp. 1191–1208.

Jolivet, Pierre, Victorita Dolean, Frédéric Hecht, Frédéric Nataf, Christophe Prud'homme, and Nicole Spillane (2012). "High-Performance Domain Decomposition Methods on Massively Parallel Architectures with FreeFem++". In: *Journal of Numerical Mathematics* 20.4, pp. 287–302.

Joo, Younghwan, Ikjin Lee, and Sung Jin Kim (2017). "Topology optimization of heat sinks in natural convection considering the effect of shape-dependent heat transfer coefficient". In: *International Journal of Heat and Mass Transfer* 109, pp. 123–133.

Kambampati, Sandilya, Carolina Jauregui, Ken Museth, and H Alicia Kim (2020). "Large-scale level set topology optimization for elasticity and heat conduction". In: *Structural and Multidisciplinary Optimization* 61.1, pp. 19–38.

Kambampati, Sandilya and H Alicia Kim (2020). "Level set topology optimization of cooling channels using the Darcy flow model". In: *Structural and Multidisciplinary Optimization*, pp. 1–17.

Karypis, George and Vipin Kumar (1998). "A Fast and High Quality Multilevel Scheme for Partitioning Irregular Graphs". In: *SIAM Journal on Scientific Computing* 20.1, pp. 359–392.

Kawamoto, Atsushi, Tadayoshi Matsumori, Shintaro Yamasaki, Tsuyoshi Nomura, Tsuguo Kondoh, and Shinji Nishiwaki (2011). "Heaviside projection based topology optimization by a PDE-filtered scalar function". In: *Structural and Multidisciplinary Optimization* 44.1, pp. 19–24.

Kikuchi, Noboru, Kyoon Yang Chung, Toshikazu Torigaki, and John E Taylor (1986). "Adaptive finite element methods for shape optimization of linearly elastic structures". In: *The Optimum Shape*. Springer, pp. 139–169.

Kim, BS, DS Lee, MY Ha, and HS Yoon (2008). "A numerical study of natural convection in a square enclosure with a circular cylinder at different vertical locations". In: *International journal of heat and mass transfer* 51.7-8, pp. 1888–1906.

Kim, Cheolwoong, Jung Mingook, Yamada Takayuki, Nishiwaki Shinji, and Yoo Jeonghoon (2020). "FreeFem++ code for reaction-diffusion equation–based topology optimization: for high-resolution boundary representation using adaptive mesh refinement". In: *Structural and Multidisciplinary Optimization* 62.1, pp. 439–455.

Koga, Adriano A, Edson Comini C Lopes, Helcio F Villa Nova, Cícero R De Lima, and Emílio Carlos Nelli Silva (2013). "Development of heat sink device by using topology optimization". In: *International Journal of Heat and Mass Transfer* 64, pp. 759–772.

Kondoh, Tsuguo, Tadayoshi Matsumori, and Atsushi Kawamoto (2012). "Drag minimization and lift maximization in laminar flows via topology optimization employing simple objective function expressions based on body force integration". In: *Structural and Multidisciplinary Optimization* 45.5, pp. 693–701.

Kranz, Micah, Julian K Lüdeker, and Benedikt Kriegesmann (2021). "An empirical study on stress-based fail-safe topology optimization and multiple load path design". In: *Structural and Multidisciplinary Optimization* 64.4, pp. 2113–2134.

Kreissl, Sebastian and Kurt Maute (2012). "Level set based fluid topology optimization using the extended finite element method". In: *Structural and Multidisciplinary Optimization* 46.3, pp. 311–326.

Kreissl, Sebastian, Georg Pingen, and Kurt Maute (2011). "Topology optimization for unsteady flow". In: *International Journal for Numerical Methods in Engineering* 87.13, pp. 1229–1253.

Kumar, Prabhat, Jan S Frouws, and Matthijs Langelaar (2020). "Topology optimization of fluidic pressure-loaded structures and compliant mechanisms using the Darcy method". In: *Structural and Multidisciplinary Optimization*, pp. 1–19.

Lazarov, Boyan S, Ole Sigmund, Knud E Meyer, and Joe Alexandersen (2018). "Experimental validation of additively manufactured optimized shapes for passive cooling". In: *Applied energy* 226, pp. 330–339.

Lazarov, Boyan Stefanov and Ole Sigmund (2011). "Filters in topology optimization based on Helmholtz-type differential equations". In: *International Journal for Numerical Methods in Engineering* 86.6, pp. 765–781.

Lee, Jaewook, Chiyoung Kwon, Jeonghoon Yoo, Seungjae Min, Tsuyoshi Nomura, and Ercan M Dede (2021). "Design of spatially-varying orthotropic infill structures using multiscale topology optimization and explicit de-homogenization". In: *Additive Manufacturing* 40, p. 101920.

Lee, Young Jin and Sung Jin Kim (2021). "Thermal optimization of the pin-fin heat sink with variable fin density cooled by natural convection". In: *Applied Thermal Engineering* 190, p. 116692.

Lei, Tian, Joe Alexandersen, Boyan S Lazarov, Fengwen Wang, Jan HK Haertel, Salvatore De Angelis, Simone Sanna, Ole Sigmund, and Kurt Engelbrecht (2018). "Investment casting and experimental testing of heat sinks designed by topology optimization". In: *International Journal of Heat and Mass Transfer* 127, pp. 396–412.

Li, Baotong, Chenhan Xie, Xinxin Yin, Rui Lu, Yue Ma, Honglei Liu, and Jun Hong (2021). "Multidisciplinary optimization of liquid cooled heat sinks with compound jet/channel structures arranged in a multipass configuration". In: *Applied Thermal Engineering*, p. 117159.

Li, Han-Ling, Dai-Yan Lan, Xian-Ming Zhang, and Bing-Yang Cao (2021). "Investigation of the parameter-dependence of topology-optimized heat sinks in natural convection". In: *Heat Transfer Engineering*, pp. 1–15.

Li, Hao, Xiaohong Ding, Dalei Jing, Min Xiong, and Fanzhen Meng (2019). "Experimental and numerical investigation of liquid-cooled heat sinks designed by topology optimization". In: *International Journal of Thermal Sciences* 146, p. 106065.

Li, Hao, Xiaohong Ding, Fanzhen Meng, Dalei Jing, and Min Xiong (2019). "Optimal design and thermal modelling for liquid-cooled heat sink based on multi-objective topology optimization: An experimental and numerical study". In: *International Journal of Heat and Mass Transfer* 144, p. 118638.

Li, Hao, Tsuguo Kondoh, Pierre Jolivet, Kozo Furuta, Takayuki Yamada, Benliang Zhu, Kazuhiro Izui, and Shinji Nishiwaki (2022). "Three-dimensional topology optimization of a fluid–structure system using body-fitted mesh adaption based on the level-set method". In: *Applied Mathematical Modelling* 101, pp. 276–308.

Li, Hao, Takayuki Yamada, Pierre Jolivet, Kozo Furuta, Tsuguo Kondoh, Kazuhiro Izui, and Shinji Nishiwaki (2021). "Full-scale 3D structural topology optimization using adaptive mesh refinement based on the level-set method". In: *Finite Elements in Analysis and Design* 194, p. 103561.

Lin, Haoju, Hui Liu, and Peng Wei (2022). "A parallel parameterized level set topology optimization framework for large-scale structures with unstructured meshes". In: *Computer Methods in Applied Mechanics and Engineering* 397, p. 115112.

Liu, Haixiang, Yuanming Hu, Bo Zhu, Wojciech Matusik, and Eftychios Sifakis (2018). "Narrow-band topology optimization on a sparsely populated grid". In: *ACM Transactions on Graphics (TOG)* 37.6, pp. 1–14.

Liu, Hui, Ye Tian, Hongming Zong, Qingping Ma, Michael Yu Wang, and Liang Zhang (2019). "Fully parallel level set method for large-scale structural topology optimization". In: *Computers & Structures* 221, pp. 13–27.

Lucy, Leon B (1977). "A numerical approach to the testing of the fission hypothesis". In: *The astronomical journal* 82, pp. 1013–1024.

Lundgaard, Christian, Joe Alexandersen, Mingdong Zhou, Casper Schousboe Andreasen, and Ole Sigmund (2018). "Revisiting density-based topology optimization for fluid-structure-interaction problems". In: *Structural and Multidisciplinary Optimization* 58.3, pp. 969–995.

Luo, Yunfeng, Ole Sigmund, Quhao Li, and Shutian Liu (2020). "Additive manufacturing oriented topology optimization of structures with self-supported enclosed voids". In: *Computer Methods in Applied Mechanics and Engineering* 372, p. 113385.

Luo, Zhen, Michael Yu Wang, Shengyin Wang, and Peng Wei (2008). "A level set-based parameterization method for structural shape and topology optimization". In: *International Journal for Numerical Methods in Engineering* 76.1, pp. 1–26.

Mahmoud, Dalia and Mohamed A Elbestawi (2017). "Lattice structures and functionally graded materials applications in additive manufacturing of orthopedic implants: a review". In: *Journal of Manufacturing and Materials Processing* 1.2, p. 13.

Marinov, Martin, Marco Amagliani, Tristan Barback, Jean Flower, Stephen Barley, Suguru Furuta, Peter Charrot, Iain Henley, Nanda Santhanam, G Thomas Finnigan, et al. (2019). "Generative design conversion to editable and watertight boundary representation". In: *Computer-Aided Design* 115, pp. 194–205.

Martínez-Frutos, Jesús, Pedro J Martínez-Castejón, and David Herrero-Pérez (2017). "Efficient topology optimization using GPU computing with multilevel granularity". In: *Advances in Engineering Software* 106, pp. 47–62.

Matsumori, Tadayoshi, Tsuguo Kondoh, Atsushi Kawamoto, and Tsuyoshi Nomura (2013). "Topology optimization for fluid–thermal interaction problems under constant input power". In: *Structural and Multidisciplinary Optimization* 47.4, pp. 571–581.

Maute, Kurt and Matthew Allen (2004). "Conceptual design of aeroelastic structures by topology optimization". In: *Structural and Multidisciplinary Optimization* 27.1-2, pp. 27–42.

McNeel, Robert (2010). "Rhinoceros 3D, Version 6.0". In: *Robert McNeel & Associates, Seattle, WA*.

Micheletti, Stefano, Simona Perotto, and Luca Soli (2019). "Topology optimization driven by anisotropic mesh adaptation: Towards a free-form design". In: *Computers & Structures* 214, pp. 60–72.

Mohammadi, Bijan and Olivier Pironneau (2010). *Applied shape optimization for fluids*. Oxford university press.

Moulin, Johann, Pierre Jolivet, and Olivier Marquet (2019). "Augmented Lagrangian preconditioner for large-scale hydrodynamic stability analysis". In: *Computer Methods in Applied Mechanics and Engineering* 351, pp. 718–743.

Myles, Ashish, Nico Pietroni, and Denis Zorin (2014). "Robust field-aligned global parametrization". In: *ACM Transactions on Graphics (TOG)* 33.4, pp. 1–14.

Nana, Alexandre, Jean-Christophe Cuillière, and Vincent Francois (2016). "Towards adaptive topology optimization". In: *Advances in Engineering Software* 100, pp. 290–307.

Nobis, Harrison, Philipp Schlatter, Eddie Wadbro, Martin Berggren, and Dan S Henningson (2022). "Topology optimization of unsteady flows using the spectral element method". In: *Computers & Fluids* 239, p. 105387.

Noguchi, Y, T Yamada, M Otomori, K Izui, and SJAPL Nishiwaki (2015). "An acoustic metasurface design for wave motion conversion of longitudinal waves to transverse waves using topology optimization". In: *Applied Physics Letters* 107.22, p. 221909.

Olesen, Laurits Højgaard, Fridolin Okkels, and Henrik Bruus (2006). "A high-level programming-language implementation of topology optimization applied to steady-state Navier–Stokes flow". In: *International Journal for Numerical Methods in Engineering* 65.7, pp. 975–1001.

Osher, Stanley, Ronald Fedkiw, and K Piechor (2004). "Level set methods and dynamic implicit surfaces". In: *Applied Mechanics Reviews* 57.3, B15–B15.

Osher, Stanley and James A Sethian (1988). "Fronts propagating with curvature-dependent speed: algorithms based on Hamilton-Jacobi formulations". In: *Journal of Computational Physics* 79.1, pp. 12–49.

Otomori, Masaki, Takayuki Yamada, Kazuhiro Izui, and Shinji Nishiwaki (2015). "Matlab code for a level set-based topology optimization method using a reaction diffusion equation". In: *Structural and Multidisciplinary Optimization* 51.5, pp. 1159–1172.

Pantz, Olivier and Karim Trabelsi (2008). "A post-treatment of the homogenization method for shape optimization". In: *SIAM Journal on Control and Optimization* 47.3, pp. 1380–1398.

Park, Michael A, Adrien Loseille, Joshua Krakos, Todd R Michal, and Juan J Alonso (2016). "Unstructured grid adaptation: status, potential impacts, and recommended investments towards CFD 2030". In: *46th AIAA Fluid Dynamics Conference*, p. 3323.

Paroncini, M and F Corvaro (2009). "Natural convection in a square enclosure with a hot source". In: *International journal of thermal sciences* 48.9, pp. 1683–1695.

Pellegrini, François and Jean Roman (1996). "Scotch: A software package for static mapping by dual recursive bipartitioning of process and architecture graphs". In: *International Conference on High-Performance Computing and Networking*. Springer, pp. 493–498.

Persson, PO (2004). "Mesh generation for implicit geometries (Ph. D. thesis)". In: *Cambridge (MA): Massachusetts Institute of Technology*.

Picelli, Renato, Eduardo Moscatelli, Paulo Vinícius Miyuki Yamabe, Diego Hayashi Alonso, Shahin Ranjbarzadeh, Rafael dos Santos Gioria, Julio Romano Meneghini, and Emílio Carlos Nelli Silva (2022). "Topology optimization of turbulent fluid flow via the TOBS method and a geometry trimming procedure". In: *Structural and Multidisciplinary Optimization* 65.1, pp. 1–25.

Picelli, Renato, A Neofytou, and H Alicia Kim (2019). "Topology optimization for design-dependent hydrostatic pressure loading via the level-set method". In: *Structural and Multidisciplinary Optimization* 60.4, pp. 1313–1326.

Picelli, Renato, Shahin Ranjbarzadeh, Raghavendra Sivapuram, RS Gioria, and Emílio Carlos Nelli Silva (2020). "Topology optimization of binary structures under design-dependent fluid-structure interaction loads". In: *Structural and Multidisciplinary Optimization* 62.4, pp. 2101–2116.

Picelli, Renato, William Martins Vicente, and Renato Pavanello (2017). "Evolutionary topology optimization for structural compliance minimization considering design-dependent FSI loads". In: *Finite elements in Analysis and Design* 135, pp. 44–55.

Pingen, Georg and Kurt Maute (2010). "Optimal design for non-Newtonian flows using a topology optimization approach". In: *Computers & Mathematics with Applications* 59.7, pp. 2340–2350.

Pollini, Nicolò, Ole Sigmund, Casper Schousboe Andreasen, and Joe Alexandersen (2020). "A "poor man's" approach for high-resolution three-dimensional topology design for natural convection problems". In: *Advances in Engineering Software* 140, p. 102736.

Powell, Michael JD (1969). "A method for nonlinear constraints in minimization problems". In: *Optimization*, pp. 283–298.

Qiu, Wenke, Peng Jin, Shaomeng Jin, Chuang Wang, Liang Xia, Jihong Zhu, and Tielin Shi (2020). "An evolutionary design approach to shell-infill structures". In: *Additive Manufacturing* 34, p. 101382.

Querin, Osvaldo M, Grant P Steven, and Yi Min Xie (1998). "Evolutionary structural optimisation (ESO) using a bidirectional algorithm". In: *Engineering computations*.

QUINT, Inc. (2021). "S-generator® www.quint.co.jp. Japan." In.

Radman, Arash, Xiaodong Huang, and Yimin Xie (2013). "Topology optimization of functionally graded cellular materials". In: *Journal of Materials Science* 48.4, pp. 1503–1510.

Raizah, Zehba AS, Sameh E Ahmed, and Abdelraheem M Aly (2020). "ISPH simulations of natural convection flow in E-enclosure filled with a nanofluid including homogeneous/heterogeneous porous media and solid particles". In: *International Journal of Heat and Mass Transfer* 160, p. 120153.

Rakotondrandisa, Aina, Georges Sadaka, and Ionut Danaila (2020). "A finite-element toolbox for the simulation of solid–liquid phase-change systems with natural convection". In: *Computer Physics Communications* 253, p. 107188.

Ranjbarzadeh, Shahin, R Picelli, R Gioria, and Emílio Carlos Nelli Silva (2022). "Topology optimization of structures subject to non-Newtonian fluid–structure interaction loads using integer linear programming". In: *Finite Elements in Analysis and Design* 202, p. 103690.

Rockafellar, Tyrell (1973). "The multiplier method of Hestenes and Powell applied to convex programming". In: *Journal of Optimization Theory and applications* 12.6, pp. 555–562.

Roy, S and Tanmay Basak (2005). "Finite element analysis of natural convection flows in a square cavity with non-uniformly heated wall (s)". In: *International Journal of Engineering Science* 43.8-9, pp. 668–680.

Rozvany, George IN, Ming Zhou, and Torben Birker (1992). "Generalized shape optimization without homogenization". In: *Structural Optimization* 4.3-4, pp. 250–252.

Sá, Luís F.N., Ricardo Cesare Roman Amigo, Antonio André Novotny, and Emílio Carlos Nelli Silva (2016). "Topological derivatives applied to fluid flow channel design optimization problems". In: *Structural and Multidisciplinary Optimization* 54.2, pp. 249–264.

Sadaka, Georges, Aina Rakotondrandisa, Pierre-Henri Tournier, Francky Luddens, Corentin Lothodé, and Ionut Danaila (2020). "Parallel finite-element codes for the simulation of two-dimensional and three-dimensional solid–liquid phase-change systems with natural convection". In: *Computer Physics Communications* 257, p. 107492.

Sasaki, Yusuke, Yuki Sato, Takayuki Yamada, Kazuhiro Izui, and Sshinji Nishiwaki (2019). "Topology optimization for fluid flows using the MPS method incorporating the level set method". In: *Computers & Fluids* 188, pp. 86–101.

Sato, Yuki, Kentaro Yaji, Kazuhiro Izui, Takayuki Yamada, and Shinji Nishiwaki (2018). "An optimum design method for a thermal-fluid device incorporating multiobjective topology optimization with an adaptive weighting scheme". In: *Journal of Mechanical Design* 140.3.

Schmit, Lucien A (1960). "Structural design by systematic synthesis". In: *Proceedings of the Second National Conference on Electronic Computation, ASCE, Sept., 1960*.

Sidik, Nor Azwadi Che, Muhammad Noor Afiq Witri Muhamad, Wan Mohd Arif Aziz Japar, and Zainudin A Rasid (2017). "An overview of passive techniques for heat transfer augmentation in microchannel heat sink". In: *International Communications in Heat and Mass Transfer* 88, pp. 74–83.

Siemens (n.d.). "Convergent modeling". In: ().

Sigmund, Ole (2001). "A 99 line topology optimization code written in Matlab". In: *Structural and multidisciplinary optimization* 21.2, pp. 120–127.

Sigmund, Ole, Niels Aage, and Erik Andreassen (2016). "On the (non-) optimality of Michell structures". In: *Structural and Multidisciplinary Optimization* 54.2, pp. 361–373.

Sivapuram, Raghavendra and Renato Picelli (2018). "Topology optimization of binary structures using Integer Linear Programming". In: *Finite Elements in Analysis and Design* 139, pp. 49–61.

Souza, BC, PVM Yamabe, LFN Sá, S Ranjbarzadeh, R Picelli, and ECN Silva (2021). "Topology optimization of fluid flow by using Integer Linear Programming". In: *Structural and Multidisciplinary Optimization*, pp. 1–20.

Sparrow, Ephraim M and SB Vemuri (1985). "Natural convection/radiation heat transfer from highly populated pin fin arrays". In.

Stolpe, Mathias and Krister Svanberg (2001). "An alternative interpolation scheme for minimum compliance topology optimization". In: *Structural and Multidisciplinary Optimization* 22.2, pp. 116–124.

Sun, Sicheng, Jaal Ghandhi, and Xiaoping Qian (2020). "Large Scale Topology Optimization of 3D Static Mixers". In: *ASME 2020 International Design Engineering Technical Conferences and Computers and Information in Engineering Conference*. American Society of Mechanical Engineers Digital Collection.

Sun, Sicheng, Piotr Liebersbach, and Xiaoping Qian (2020). "3D topology optimization of heat sinks for liquid cooling". In: *Applied Thermal Engineering* 178, p. 115540.

Svanberg, Krister (1987). "The method of moving asymptotes—a new method for structural optimization". In: *International journal for numerical methods in engineering* 24.2, pp. 359–373.

Takezawa, Akihiro, Xiaopeng Zhang, Masaki Kato, and Mitsuru Kitamura (2019). "Method to optimize an additively-manufactured functionally-graded lattice structure for effective liquid cooling". In: *Additive Manufacturing* 28, pp. 285–298.

Träff, Erik A., Ole Sigmund, and Niels Aage (n.d.). "Topology optimization of ultra high resolution shell structures". In: *Thin-Walled Structures* 160 (), p. 107349.

Träff, Erik A, Ole Sigmund, and Niels Aage (2021). "Topology optimization of ultra high resolution shell structures". In: *Thin-Walled Structures* 160, p. 107349.

Troya, Miguel A Salazar de, Daniel A Tortorelli, Julian Andrej, and Victor A Beck (2021). "Three-dimensional topology optimization of heat exchangers with the level-set method". In: *arXiv preprint arXiv:2111.09471*.

Tuckerman, David B and Roger Fabian W Pease (1981). "High-performance heat sinking for VLSI". In: *IEEE Electron device letters* 2.5, pp. 126–129.

Villanueva, Carlos H and Kurt Maute (2017). "CutFEM topology optimization of 3D laminar incompressible flow problems". In: *Computer Methods in Applied Mechanics and Engineering* 320, pp. 444–473.

Wang, Michael Yu, Xiaoming Wang, and Dongming Guo (2003). "A level set method for structural topology optimization". In: *Computer Methods in Applied Mechanics and Engineering* 192.1-2, pp. 227–246.

Wang, SY, Kian Meng Lim, Boo Cheong Khoo, and MY Wang (2007). "An extended level set method for shape and topology optimization". In: *Journal of Computational Physics* 221.1, pp. 395–421.

Wang, Yaguang and Zhan Kang (2018). "A velocity field level set method for shape and topology optimization". In: *International Journal for Numerical Methods in Engineering* 115.11, pp. 1315–1336.

Williams, H Paul (2009). "Integer programming". In: *Logic and Integer Programming*. Springer, pp. 25–70.

Wirth, N (1985). *Algorithms+ Data Structures= Programs (Vol. 76)*.

Wu, Jun, Niels Aage, Rüdiger Westermann, and Ole Sigmund (2017). "Infill optimization for additive manufacturing—approaching bone-like porous structures". In: *IEEE Transactions on Visualization and Computer Graphics* 24.2, pp. 1127–1140.

Wu, Jun, Anders Clausen, and Ole Sigmund (2017). "Minimum compliance topology optimization of shell–infill composites for additive manufacturing". In: *Computer Methods in Applied Mechanics and Engineering* 326, pp. 358–375.

Wu, Jun, Christian Dick, and Rüdiger Westermann (2015). "A system for high-resolution topology optimization". In: *IEEE Transactions on Visualization and Computer Graphics* 22.3, pp. 1195–1208.

Wu, Jun, Ole Sigmund, and Jeroen P Groen (2021). "Topology optimization of multi-scale structures: a review". In: *Structural and Multidisciplinary Optimization* 63.3, pp. 1455–1480.

Xia, Liang, Qi Xia, Xiaodong Huang, and Yi Min Xie (2018). "Bi-directional evolutionary structural optimization on advanced structures and materials: a comprehensive review". In: *Archives of Computational Methods in Engineering* 25.2, pp. 437–478.

Xie, Y Mike and Grant P Steven (1997). "Basic evolutionary structural optimization". In: *Evolutionary structural optimization*. Springer, pp. 12–29.

Xie, Yi Min and Grant P. Steven (1993). "A simple evolutionary procedure for structural optimization". In: *Computers & Structures* 49.5, pp. 885–896.

XIE-Engineering-Technologies. (2021). "Ameba® www.ameba.xieym.com. China". In.

Yaji, Kentaro (2016). "Topology optimization using the lattice Boltzmann method and applications in flow channel designs considering thermal and two-phase fluid flows". In.

Yaji, Kentaro, Masao Ogino, Cong Chen, and Kikuo Fujita (2018). "Large-scale topology optimization incorporating local-in-time adjoint-based method for unsteady thermal-fluid problem". In: *Structural and Multidisciplinary Optimization* 58.2, pp. 817–822.

Yaji, Kentaro, Masaki Otomori, Takayuki Yamada, Kazuhiro Izui, Shinji Nishiwaki, and Olivier Pironneau (2016). "Shape and topology optimization based on the convected level set method". In: *Structural and Multidisciplinary Optimization* 54.3, pp. 659–672.

Yaji, Kentaro, Takayuki Yamada, Seiji Kubo, Kazuhiro Izui, and Shinji Nishiwaki (2015). "A topology optimization method for a coupled thermal–fluid problem using level set boundary expressions". In: *International Journal of Heat and Mass Transfer* 81, pp. 878–888.

Yaji, Kentaro, Takayuki Yamada, Masato Yoshino, Toshiro Matsumoto, Kazuhiro Izui, and Shinji Nishiwaki (2014). "Topology optimization using the lattice Boltzmann method incorporating level set boundary expressions". In: *Journal of Computational Physics* 274, pp. 158–181.

— (2016). "Topology optimization in thermal-fluid flow using the lattice Boltzmann method". In: *Journal of Computational Physics* 307, pp. 355–377.

Yaji, Kentaro, Shintaro Yamasaki, and Kikuo Fujita (2020). "Multifidelity design guided by topology optimization". In: *Structural and Multidisciplinary Optimization* 61.3, pp. 1071–1085.

Yamada, Takayuki, Kazuhiro Izui, Shinji Nishiwaki, and Akihiro Takezawa (2010). "A topology optimization method based on the level set method incorporating a fictitious interface energy". In: *Computer Methods in Applied Mechanics and Engineering* 199.45-48, pp. 2876–2891.

Yamada, Takayuki and Yuki Noguchi (2022). "Topology optimization with a closed cavity exclusion constraint for additive manufacturing based on the fictitious physical model approach". In: *Additive Manufacturing* 52, p. 102630.

Yan, Suna, Fengwen Wang, and Ole Sigmund (2018). "On the non-optimality of tree structures for heat conduction". In: *International Journal of Heat and Mass Transfer* 122, pp. 660–680.

Yan, Xin Yu, Yuan Liang, and Geng Dong Cheng (2021). "Discrete variable topology optimization for simplified convective heat transfer via sequential approximate integer programming with trust-region". In: *International Journal for Numerical Methods in Engineering*.

Yang, Kai, Zi-Long Zhao, Yunzhen He, Shiwei Zhou, Qiang Zhou, Weixin Huang, and Yi Min Xie (2019). "Simple and effective strategies for achieving diverse and competitive structural designs". In: *Extreme Mechanics Letters* 30, p. 100481.

Yang, Xiao Ying, Yi Min Xie, Grant P. Steven, and Osvaldo Querin (1999). "Bidirectional evolutionary method for stiffness optimization". In: *AIAA Journal* 37.11, pp. 1483–1488.

Yi, Bing, Yuqing Zhou, Gil Ho Yoon, and Kazuhiro Saitou (2019). "Topology optimization of functionally-graded lattice structures with buckling constraints". In: *Computer Methods in Applied Mechanics and Engineering* 354, pp. 593–619.

Yoon, Gil Ho (2010a). "Topological design of heat dissipating structure with forced convective heat transfer". In: *Journal of Mechanical Science and Technology* 24.6, pp. 1225–1233.

— (2010b). "Topology optimization for stationary fluid–structure interaction problems using a new monolithic formulation". In: *International journal for numerical methods in engineering* 82.5, pp. 591–616.

— (2016). "Topology optimization for turbulent flow with Spalart–Allmaras model". In: *Computer Methods in Applied Mechanics and Engineering* 303, pp. 288–311.

Yu, Minghao, Shilun Ruan, Junfeng Gu, Mengke Ren, Zheng Li, Xinyu Wang, and Changyu Shen (2020). "Three-dimensional topology optimization of thermal-fluid-structural problems for cooling system design". In: *Structural and Multidisciplinary Optimization* 62.6, pp. 3347–3366.

Yu, Minghao, Shilun Ruan, Xinyu Wang, Zheng Li, and Changyu Shen (2019). "Topology optimization of thermal–fluid problem using the MMC-based approach". In: *Structural and Multidisciplinary Optimization* 60.1, pp. 151–165.

Zeng, Shi, Bugra Kanargi, and Poh Seng Lee (2018). "Experimental and numerical investigation of a mini channel forced air heat sink designed by topology optimization". In: *International Journal of Heat and Mass Transfer* 121, pp. 663–679.

Zeng, Shi and Poh Seng Lee (2019). "Topology optimization of liquid-cooled microchannel heat sinks: An experimental and numerical study". In: *International Journal of Heat and Mass Transfer* 142, p. 118401.

Zhang, Heng, Xiaohong Ding, Hao Li, and Min Xiong (2019). "Multi-scale structural topology optimization of free-layer damping structures with damping composite materials". In: *Composite Structures* 212, pp. 609–624.

Zhang, Heng, Akihiro Takezawa, Xiaohong Ding, Honghu Guo, Weiyu Ni, and Xiaopeng Zhang (2021). "Topology optimization of composite macrostructures comprising multi-phase viscoelastic composite microstructures for enhanced structural damping". In: *Composite Structures* 278, p. 114712.

Zhang, Heng, Akihiro Takezawa, Xiaohong Ding, Shipeng Xu, Pengyun Duan, Hao Li, and Honghu Guo (2021). "Bi-material microstructural design of biodegradable composites using topology optimization". In: *Materials & Design* 209, p. 109973.

Zhang, Heng, Akihiro Takezawa, Xiaohong Ding, Shipeng Xu, Hao Li, and Honghu Guo (2021). "Topology optimization of degradable composite structures with time-changeable stiffness". In: *International Journal for Numerical Methods in Engineering* 122.17, pp. 4751–4773.

Zhang, Heng, Akihiro Takezawa, Xiaohong Ding, Xiaopeng Zhang, Shipeng Xu, Hao Li, Shuya Nozawa, and Shinji Nishiwaki (2022). "Robust topology optimization of biodegradable composite structures under uncertain degradation rates". In: *Composite Structures* 291, p. 115593.

Zhang, Weisheng, Jishun Chen, Xuefeng Zhu, Jianhua Zhou, Dingchuan Xue, Xin Lei, and Xu Guo (2017). "Explicit three dimensional topology optimization via Moving Morphable Void (MMV) approach". In: *Computer Methods in Applied Mechanics and Engineering* 322, pp. 590–614.

Zhao, Xi, Mingdong Zhou, Ole Sigmund, and Casper Schousboe Andreasen (2018). "A "poor man's approach" to topology optimization of cooling channels based on a Darcy flow model". In: *International Journal of Heat and Mass Transfer* 116, pp. 1108–1123.

Zhou, Ming and George IN Rozvany (1991). "The COC algorithm, Part II: Topological, geometrical and generalized shape optimization". In: *Computer Methods in Applied Mechanics and Engineering* 89.1-3, pp. 309–336.

Zhou, Mingdong, Joe Alexandersen, Ole Sigmund, and Claus BW Pedersen (2016). "Industrial application of topology optimization for combined conductive and convective heat transfer problems". In: *Structural and Multidisciplinary Optimization* 54.4, pp. 1045–1060.

Zhou, Mingdong, Yufan Lu, Yichang Liu, and Zhongqin Lin (2022). "Concurrent topology optimization of shells with self-supporting infills for additive manufacturing". In: *Computer Methods in Applied Mechanics and Engineering* 390, p. 114430.

Zhou, Qiang, Wei Shen, Jin Wang, Yi Yi Zhou, and Yi Min Xie (2018). "Ameba: A new topology optimization tool for architectural design". In: *Proceedings of IASS Annual Symposia*. Vol. 2018. 19. International Association for Shell and Spatial Structures (IASS), pp. 1–8.

Zhou, Shiwei and Qing Li (2008). "A variational level set method for the topology optimization of steady-state Navier–Stokes flow". In: *Journal of Computational Physics* 227.24, pp. 10178–10195.

Zhou, Yuqing, Danny J Lohan, Feng Zhou, Tsuyoshi Nomura, and Ercan M Dede (2022). "Inverse design of microreactor flow fields through anisotropic porous media optimization and dehomogenization". In: *Chemical Engineering Journal* 435, p. 134587.

Zhu, Benliang, Rixin Wang, Nianfeng Wang, Hao Li, Xianmin Zhang, and Shinji Nishiwaki (2021). "Explicit structural topology optimization using moving wide Bezier components with constrained ends". In: *Structural and Multidisciplinary Optimization* 64.1, pp. 53–70.

Zhu, Benliang, Xianmin Zhang, Hai Li, Junwen Liang, Rixin Wang, Hao Li, and Shinji Nishiwaki (2021). "An 89-line code for geometrically nonlinear topology optimization written in FreeFEM". In: *Structural and Multidisciplinary Optimization* 63.2, pp. 1015–1027.

Zhu, Benliang, Xianmin Zhang, and Nianfeng Wang (2013). "Topology optimization of hinge-free compliant mechanisms with multiple outputs using level set method". In: *Structural and Multidisciplinary Optimization* 47.5, pp. 659–672.

Zhu, Benliang, Xianmin Zhang, Hongchuan Zhang, Junwen Liang, Haoyan Zang, Hai Li, and Rixin Wang (2020). "Design of compliant mechanisms using continuum topology optimization: A review". In: *Mechanism and Machine Theory* 143, p. 103622.

Zhu, Ji-Hong, Wei-Hong Zhang, and Liang Xia (2016). "Topology optimization in aircraft and aerospace structures design". In: *Archives of Computational Methods in Engineering* 23.4, pp. 595–622.

About the Author

Hao Li was born in Shanghai, China, on February 18, 1994.

From September 2012 to June 2016, he received his undergraduate education in automated system design at Liverpool John Moores University (UK) and earned the first-class honors degree. Also, he earned a dual bachelor's degree in mechanical system design from University of Shanghai for Science and Technology (USST), China. The title of his final year project was "To build and automated system to straighten the annealed swayed copper pipe of the electronic expansion valve". He was awarded the Outstanding Bachelor Thesis for his final year project.

From September 2016 to June 2019, he was enrolled in the School of Mechanical Engineering, University of Shanghai for Science for Technology for his master's degree under the supervision of Professor Xiaohong Ding. His master research project is about the topology optimization of high heat flux heat sink. In 2017, he was awarded the Outstanding Paper Award at the 18th International Conference on Electronic Packaging Technology & High-Density Packaging in Harbin, China. In 2018, he received a full grant from the Deutscher Akademischer Austauschdienst (DAAD) and worked at Paderborn Universität as a research intern for three months. In 2019, he was awarded the Outstanding Master Thesis Award.

In October 2019, he was enrolled in Kyoto University to pursue his Ph.D. degree in Mechanical Engineering under the supervision of Professor Shinji Nishiwaki, with his main research interests in the mathematical modeling of multi-physics and topology optimization. In April 2021, he became a DC-2 research fellow of the Japan Society for the Promotion of Science (JSPS). His research project " Large-scale multiphysics topology optimization for thermal and fluid systems" was funded by a JSPS grant (No. JP21J13418). In the course of his master's and doctoral studies, he has published and co-authored more than 20 journal articles and made numerous oral presentations at domestic and international conferences.

After his doctoral course, he will continue doing research as a postdoc researcher. Based on his prior and ongoing research experience, he aims at going beyond the-state-of-the-art and delivering more attractive conceptual designs.

July, 2022

Publication List

Peer-reviewed Journal Articles

1. **Li, H.**, Yu, M., Jolivet, P., Alexandersen, J., Kondoh, T., Furuta, K., Izui, K., and Nishiwaki, S., "Level set-based topology optimization of high resolution lattice structures using a PDE-filter with unstructured meshes." Preprint submitted to *Advances in Engineering Software* (2022).
2. Zhang, H., Ding, X., Guo, H., Xu, S., **Li, H.**, Nishiwaki, S., Chen, Y., and Takezawa, A., "Multiscale topology optimization of biodegradable metal matrix composite structures for additive manufacturing." Preprint submitted to *Applied Mathematical Modelling* (2022), under review.
3. Ishida, N., Kondoh, T., Furuta, K., **Li, H.**, Izui, K., and Nishiwaki, S., "Topology optimization for maximizing linear buckling load based on level set method." accepted for publication in *Mechanical Engineering Journal* (2022), in press.
4. Pan, S., Yu, M., **Li, H.**, Li, Z., Reng, M., Gu, J., and Shen, C., "An integrated two–step strategy for an optimal design of liquid–cooled channel layout based on the MMC-Density approach." accepted for publication in *Structural and Multidisciplinary Optimization* (2022), in press.
5. **Li, H.**, Kondoh, T., Jolivet, P., Nakayama, N., Furuta, K., Zhang, H., Zhu, B., Izui, K., and Nishiwaki, S., "Topology optimization for lift–drag problems incorporated with distributed unstructured mesh adaptation." accepted for publication in *Structural and Multidisciplinary Optimization* (2022), DOI: 10.1007/s00158-022-03314-w, in press.
6. Hu, T., Wang, Y., Zhang, H., **Li, H.**, Ding, X., Izui, K., and Nishiwaki, S., "Topology optimization of coated structures with layer-wise graded lattice infill for maximizing the fundamental eigenfrequency." accepted for publication in *Computers & Structures* 271 (2022): 106861, DOI: 10.1016/j.compstruc.2022.106861.
7. Yeranee, K., Rao, Y., Li, Y., and **Li, H.**, "Enhanced thermal performance of a pin-fin cooling channel for gas turbine blade by density-based topology optimization." accepted for publication in *International Journal of Thermal Sciences* 181 (2022): 107783, DOI: 10.1016/j.ijthermalsci.2022.107783.
8. Zhang, H., Takezawa, A., Ding, D., Zhang, X., Xu, S., **Li, H.**, Nozawa, S., and Nishiwaki,

S., "Robust topology optimization of biodegradable composite structures under uncertain degradation rates." *Composite Structures* 291 (2022): 115593, DOI: 10.1016/j.compstruct.2022.115593.

9. Meng, F., Ding, X., **Li, H.**, and Xiong, M., "Optimal design of liquid-cooled uniform-temperature plate with hierarchical vein structure." accepted for publication in *Journal of Mechanical Engineering* (2022), in Chinese, in press.
10. **Li, H.**, Kondoh, T., Jolivet, P., Furuta, K., Yamada T., Zhu, B., Zhang H., Izui K., and Nishiwaki, S., "Optimum design and thermal modeling for 2D and 3D natural convection problems incorporating level set-based topology optimization with body-fitted mesh." *International Journal for Numerical Methods in Engineering* 123, no.9 (2022): 1954–1990, DOI: 10.1002/nme.6923.
11. Zhu, B., Wang, R., Liang, J., Lai, J., Zhang, H., Li, H., **Li, H.**, Nishiwaki, S., and Zhang, X., "Design of compliance mechanism: an explicit topology optimization method using end-constrained spline curves with variable width." *Mechanism and Machine Theory* 171 (2022): 104713, DOI: 10.3390/ma15020538.
12. Zhang, H., Ding, X., Chen, Y., Zhang, X., **Li, H.**, and Ni, W., "Concurrent topology optimization of composite plates for minimum dynamic compliance." *Materials* 15, no.2 (2022): 538, DOI: 10.3390/ma15020538.
13. Hu, T., Ding, X., Zhang, H., Shen, L., and **Li, H.**, "Geometry and size optimization of stiffener layout for three-dimensional box structures with maximization of natural frequencies." *Chinese Journal of Aeronautics* (2022), DOI: 10.1016/j.cja.2022.06.010, in press.
14. **Li, H.**, Kondoh, T., Jolivet, P., Furuta, F., Yamada, T., Zhu, B., Izui, K., and Nishiwaki, S., "Three-dimensional topology optimization of fluid-structure system using body-fitted mesh adaption based on the level-set method." *Applied Mathematical Modelling* 101 (2022): 276-308, DOI: 10.1016/j.apm.2021.08.021.
15. Zhang, H., **Li, H.**, Ding, X., Hu, T., Pan, S., Ni, W., Xu, S., "Numerical study on the body-fitted topology optimization for three-dimensional high resolution structure design" *Journal of Mechanical Engineering* 58, no.5 (2022): 136-143, in Chinese, DOI: 10.3901/JME.2022.05.136.
16. Zhu, B., Wang, R., Zhang, H., Li, H., Liang, J., Zhang, X., **Li, H.**, and Nishiwaki, S., "An approach for geometrically nonlinear topology optimization using moving wide-Bézier components with constrained ends." *Journal of Mechanical Design* 144, no.1 (2022): 011704, DOI: 10.1115/1.4051872.
17. Zhang, H., Takezawa, A., Ding, X., Xu, S., Duan, P., **Li, H.**, and Guo, H., "Bi-material microstructural design of biodegradable composites using topology optimization" *Materials & Design* 209 (2021): 109973, DOI: 10.1016/j.matdes.2021.109973.
18. Zhang, H., Takezawa, A., Ding, X., Xu, S., **Li, H.**, and Guo, H., "Topology optimization of degradable composite structures with time-changeable stiffness." *International Journal for Numerical Methods in Engineering* 122 (2021): 4751–4773, DOI: 10.1002/nme.6745.

19. Zhu, B., Zhang, X., Li, H., Wang, R., Liu, M., and **Li, H.**, "Topology optimization of multi-material compliant mechanisms using node-density interpolation scheme." *Journal of Mechanical Engineering* 57, no. 15 (2021): 53-61, in Chinese, DOI: 10.3901/JME.2021.15.053.

20. **Li, H.**, Yamada, T., Jolivet, P., Furuta, K., Kondoh, T., Izui, K., and Nishiwaki, S., "Full-scale 3D structural topology optimization using adaptive mesh refinement based on level-set method." *Finite Elements in Analysis and Design* 194 (2021): 103561, DOI: 10.1016/j.finel.2021.103561.

21. Zhu, B., Wang, R., Wang, N., **Li, H.**, Zhang, X., and Nishiwaki, S., "Explicit structural topology optimization using moving wide Bezier components with constrained ends." *Structural and Multidisciplinary Optimization* 64 (2021): 53-70, DOI: 10.1007/s00158-021-02853-y.

22. Zhu, B., Zhang, X., Li, H., Liang, J., Wang, R., **Li, H.**, and Nishiwaki, S., "An 89-line code for geometrically nonlinear topology optimization written in FreeFEM." *Structural and Multidisciplinary Optimization* 63 (2020): 1015–1027, DOI: 10.1007/s00158-020-02733-x.

23. Zhang, H., Ding, X., Wang, Q., Ni, W., and **Li, H.**, "Topology optimization of damping composite material with broadband high damping." *Computers and Structures* 239 (2020): 106331, DOI: 10.1016/j.compstruc.2020.106331.

24. **Li, H.**, Ding, X., Meng, F., Jing, D., and Xiong, M., "Optimal design and thermal modelling for liquid-cooled heat sink based on multi-objective topology optimization: An experimental and numerical study." *International Journal of Heat and Mass Transfer* 144 (2019): 118638, DOI: 10.1016/j.ijheatmasstransfer.2019.118638.

25. **Li, H.**, Ding, X., Jing, D., Xiong, M., and Meng, F., "Experimental and numerical investigation of liquid-cooled heat sinks designed by topology optimization." *International Journal of Thermal Sciences* 146 (2019): 106065, DOI: 10.1016/j.ijthermalsci.2019.106065.

26. **Li, H.**, Ding, X., Jing, D., "Experimental and Numerical Investigation of Fluid Cooling Channel Layout Designed by Topology Optimization." *Journal of Mechanical Engineering* 055 (2019): 198-206, in Chinese, DOI: 10.3901/JME.2019.10.198.

27. Zhang, H., Ding, X., **Li, H.**, and Xiong, M., "Multi-scale structural topology optimization of free-layer damping structures with damping composite materials." *Composite Structures* 212 (2019): 609-624, DOI: 10.1016/j.compstruct.2019.01.059.

28. Ji, Y., Ding, X., **Li, H.**, and Xiong, M., "Layout Design of Conductive Heat Channel by Emulating Natural Branch Systems." *Journal of Bionic Engineering* 15, no. 3 (2018): 567-578, DOI: 10.1007/s42235-018-0047-3.

Conference Presentations

1. **Li, H.**, Yu, M., Alexandersen, J., Ishida, N., Kondoh, T., Furuta, K., Izui, K., and Nishiwaki, S., "Topology optimization of high resolution lattice structures using a PDE-filter." *32th Conference of Design & Systems*, Okayama, Japan, Sep 20–Sep 22, 2022.
2. Bae, S., Nakayama, N., **Li, H.**, Furuta, K., Izui, K., and Nishiwaki, S., "Topology optimization of an air compressor mount based on harmonic analysis." *32th Conference of Design & Systems*, Okayama, Japan, Sep 20–Sep 22, 2022.
3. Hu, T., Wang, Y., Zhang, H., **Li, H.**, Ding, X., Izui, K., and Nishiwaki, S., "Multiscale topology optimization of coated structures with layer-wise graded lattice infill for maximum fundamental eigenfrequency." *32th Conference of Design & Systems*, Okayama, Japan, Sep 20–Sep 22, 2022.
4. **Li, H.**, Yu, M., Jolivet, P., Alexandersen, J. Kondoh, T., Furuta, K., Izui, K., and Nishiwaki, S., "Large-scale level set-based topology optimization lattice structure using a PDE-filter." *Annual conference of The Japan Society for Industrial and Applied Mathematics*, Hokkaido, Japan, Sep 8–Sep 10, 2022.
5. Miura, H., Han, J., **Li, H.**, Furuta, F., Kondoh, T., Nishiwaki, S., Moriguchi, S., and Terada, K., "Topology optimization for maximizing fracture resistance using crack phase-field and reaction-diffusion-based level-set approach." *15th World Congress on Computational Mechanics & 8th Asian Pacific Congress on Computational Mechanics (WCCM–APCOM)*, Yokohama, Japan, Jul 31–Aug 5, 2022.
6. Nakayama, N., **Li, H.**, Jolivet, P., Furuta, K., Nishiwaki, S., and Izui, K., "Multi–material topology optimization of an eigenfrequency problem." *15th World Congress on Computational Mechanics & 8th Asian Pacific Congress on Computational Mechanics (WCCM–APCOM)*, Yokohama, Japan, Jul 31–Aug 5, 2022.
7. Ishida, N., **Li, H.**, Kondoh, T., Furuta, K., Izui, K., and Nishiwaki, S., "Level-set based topology optimization of a microfluidic mixing problem." *15th World Congress on Computational Mechanics & 8th Asian Pacific Congress on Computational Mechanics (WCCM–APCOM)*, Yokohama, Japan, Jul 31–Aug 5, 2022.
8. **Li, H.**, Kondoh, T., Jolivet, P., Furuta, K., Zhang, H., Izui, K., and Nishiwaki, S., "Topology optimization of thermal fluid–structure systems." *15th World Congress on Computational Mechanics & 8th Asian Pacific Congress on Computational Mechanics (WCCM–APCOM)*, Yokohama, Japan, Jul 31–Aug 5, 2022.
9. Zhang, H., Ding, X., **Li, H.**, Xu, S., Duan, P., Xiong, W., and Takezawa, A., "Topology optimization of biodegradable composite structures with tunable time-changeable stiffness." *15th World Congress on Computational Mechanics & 8th Asian Pacific Congress on Computational Mechanics (WCCM–APCOM)*, Yokohama, Japan, Jul 31–Aug5, 2022.

10. Nakayama, N., **Li, H.**, Jolivet, P., Furuta, K., Izui, K., and Nishiwaki, S., "Multi-material topology optimization of an eigenfrequency problem." *Asian Congress of Structural and Multidisciplinary Optimization (ACSMO)*, Matsue, Japan, May 22–26, 2022.
11. Pan, S., Yu, M., **Li, H.**, Li, Z., Ren, M., and Shen, C., "Numerical investigation of liquid-cooled heat sinks designed by MMC-density two-step strategy." *Asian Congress of Structural and Multidisciplinary Optimization (ACSMO)*, Matsue, Japan, May 22–26, 2022.
12. Ishida, N., **Li, H.**, Kondoh, T., Furuta, K., Izui, K., and Nishiwaki, S., "Topology optimization for a static microfluid mixing problem based on the level-set method." *Asian Congress of Structural and Multidisciplinary Optimization (ACSMO)*, Matsue, Japan, May 22–26, 2022.
13. Hu, T., Wang, Y., Zhang, H., **Li, H.**, Ding, X., Izui, K., and Nishiwaki, S., "Topological design of coated structures with layer-wise graded lattice infill for the maximization of the fundamental eigenfrequency." *Asian Congress of Structural and Multidisciplinary Optimization (ACSMO)*, Matsue, Japan, May 22–26, 2022.
14. **Li, H.**, Kondoh, T., Jolivet, P., Furuta, K., Zhang, H., Yamada, T., Izui, K., and Nishiwaki, S., "Level-set based topology optimization of multi-physics systems incorporating mesh adaptation." *Asian Congress of Structural and Multidisciplinary Optimization (ACSMO)*, Matsue, Japan, May 22–26, 2022.
15. **Li, H.**, Nakayama, N., Jolivet, P., Ishida, N., Wano, K., Kondoh, T., Furuta, K., and Nishiwaki, S., "Topology optimization of a thermo-fluid system and an eigenfrequency problem." *FreeFEM DAYs*, Paris, France, Dec 8–10, 2021.
16. **Li, H.**, Kondoh, T., Jolivet, P., Wano, K., Furuta, K., Yamada, T., Zhang, H., Izui, K., and Nishiwaki, S., "Body-fitted topology optimization: a novel framework for optimal design and thermal modelling of full-scale 3D natural convection problems." *Annual meeting of the Japan Society for Industrial and Applied Mathematics (JSIAM)*, online, Japan, Sep 7–9, 2021.
17. **Li, H.**, Kondoh, T, Jolivet, P., Furuta, K., Yamada, T., Izui, K., and Nishiwaki, S., "Reaction-Diffusion Equation-based Topology Optimization: a novel framework for 2D and 3D Thermal Fluid-Structure System Design." *14th World Congress of Structural and Multidisciplinary Optimization (WSCMO)*, online, Colorado, US, June 13–18, 2021.
18. **Li, H.**, Yamada, T., Jolivet, P., Wano, K., Kondoh, T., Furuta, K., Izui, K., and Nishiwaki, S., "Three-dimensional topology optimization of fluid-structure system based on the level-set method using body-fitted adaptive mesh refinement." *22nd Research workshop of the Japan Society for Industrial and Applied Mathematics (JSIAM)*, online, Japan, Dec 18, 2020.
19. **Li, H.**, Yamada, T., Jolivet, P., Wano, K., Kondoh, T., Izui, K., and Nishiwaki, S., " Reaction-diffusion equation–based topology optimization: 3D fluid-structure system design using FreeFEM-PETSc-Mmg." *FreeFEM Days*, online, Paris, France, Dec 10–11, 2020.

20. **Li, H.**, Furuta, K., Jolivet, P., Yamada, T., Izui, K., and Nishiwaki, S., "A fully parallel distributed 3D topology optimization framework using adaptive mesh refinement based on level-set method." *Asian Congress of Structural and Multidisciplinary Optimization (ACSMO)*, Seoul, Korea, Nov 22–26, 2020.
21. **Li, H.**, Yamada, T., Jolivet, P., Izui, K., and Nishiwaki, S., "Structural topology optimization of fluid-structure problem using adaptive mesh and parallel computing." *Annual Meeting of the Japan Society for Industrial and Applied Mathematics (JSIAM)*, via zoom, Japan, Sep 8–10, 2020.
22. **Li, H.**, Ding, X., and Hu, T., "Optimal design and thermal modeling for liquid-cooled heat sink based on multi-objective topology optimization: an experimental and numerical study." *13th World Congress of Structural and Multidisciplinary Optimization (WSCMO)*, Beijing, China, May 20–24, 2019.
23. **Li, H.**, Pan, S., Ding, X., Jing, D., and Xiong, M, "Experimental and numerical investigation of micro-fluid channel designed by topology optimization." *COMSOL Conference*, Shanghai, China, November 01–02, 2018.
24. Xu, L., **Li, H.**, Ding, X., and Liu, S., "Design of microchannel heat sink using topology optimization for high power modules cooling." *18th International Conference on Electronic Packaging Technology (ICEPT)*, Harbin, China, August 16–19, 2017.